Wavelength-Selective Light Trapping for Enhanced Photogeneration, Radiative Cooling and Sub-Bandgap Reflection

by

Nicholas Price Irvin

A Dissertation Presented in Partial Fulfillment
of the Requirements for the Degree
Doctor of Philosophy

Approved April 2023 by the
Graduate Supervisory Committee:

Christiana Honsberg, Co-Chair
Richard King, Co-Chair
David Smith
Robert Nemanich

ARIZONA STATE UNIVERSITY

May 2023

ABSTRACT

This work investigates the impact of wavelength-selective light trapping on photovoltaic efficiency and operating temperature, with a focus on GaAs and Si devices.

A nanostructure array is designed to optimize the efficiency of a III-V narrow-band photonic power converter (PPC). Within finite-difference time-domain (FDTD) simulations, a nanotextured GaInP window layer yields a 25× path-length enhancement when integrated with a rear dielectric-metal reflector. Then, nanotexturing of GaInP is experimentally achieved with electron-beam lithography (EBL) and Cl_2/Ar plasma etching. Time-resolved photoluminescence (TRPL) measurements show that the GaAs absorber lifetime does not drop due to the nanotexturing process, thus indicating a path to thinner, higher-efficiency PPCs.

Next, wavelength-selective light management is examined for enhanced radiative cooling. It is shown that wavelength-selective optimizations of a module's emissivity can yield 60-65% greater radiative cooling benefits compared to comparative changes across a broader wavelength range. State-of-the-art Si modules that utilize microtextured cover glass are shown to already achieve 99% of the radiative cooling gains that are possible for a photovoltaic device under full sunlight.

In contrast, the sub-bandgap reflection (SBR) of Si modules is shown to be far below ideal. The low SBR of modules with textured Si cells (15%-26%) is shown to be the primary reason for their higher operating temperatures than modules with planar GaAs cells (SBR measured at 77%). For textured cells, typical of Si modules, light trapping amplifies parasitic absorption in the encapsulant and the rear mirror, yielding

greater heat generation. Optimization of doping and the rear mirror of a Si module could increase the SBR to a maximum of 63%, with further increases available only if parasitic absorption in the encapsulation materials can be reduced. For thin films, increased heat generation may outweigh the photogeneration benefits that are possible with light trapping.

These investigations motivate a wavelength-selective application of light trapping: light trapping for near- to above-bandgap photons to increase photogeneration; and out-coupling of light in mid- to far-infrared wavelengths to increase the emission of thermal radiation; but light trapping should ideally be avoided at sub-bandgap energies where there is substantial solar radiation to limit heat generation and material degradation.

ACKNOWLEDGMENTS

I want to thank my advisors for their patience and guidance. I could not have done this work without the guidance of Professor Christiana Honsberg and the tutelage of Professor Richard King. My deepest appreciation goes out to my other invaluable mentors, including Doctors Chaomin Zhang, Michael Goryll, André Augusto, Eric Chen, Stuart Bowden, Bill Dauksher, Stephen Goodnick, Michelle Jordan, and Jongwon Lee. I also want to acknowledge my collaborators, including Srinath Murali for his development of the GaNP material, Alex Routhier for guiding me through my position at student leadership, Sangpyeong Kim for his in-depth teaching on his nanotexturing process, and Mansoure Moeini Rizi for her electrical characterization of the GaNP material. At the King lab, I want to think Sean Babcock and Madhan K. Arulanandam for their development of photon recycling theory and fabrication, Abhinav Chikhalkar for his expertise on photoluminescence measurements, Chris Gregory for his guidance on accurate UV-VIS spectroscopy. At the Stuart Bowden lab, I want to thank so many, including Pradeep Balaji for training me on various laboratory equipment and Alex Killam for his advice on outdoor testing. At the Zachary Holman lab, I thank Barry Hartweg and Jonathan Bryan for their expertise in thermal measurements and thermal PV behavior. I want to thank Tara Nietzold from the Mariana Bertoni group and Calli Campbell, Maxwell Lassise, and Cheng-Ying Tsai from the Yong-Hang Zhang group for teaching me the first things I ever learned about PV.

I am grateful to collaborators at Karin Hinzer group, including Neda Nouri. Thank you, Mathieu de Lafontaine, for fabricating the nanostructures that I designed – and then

teaching me the process! I also really want to thank the Sarah Kurtz group, including Aaron Wheeler and D. Martínez Escobar, for completing the outdoors Si and GaAs measurements. I want to thank the Christian Wolff group at École Polytechnique Fédérale de Lausanne (EPFL) as well as Tomas Leijtens, Giles Eperon, and company at Swift Solar Inc. for our collaborations on perovskite thermal behavior. I thank Hadi Afshari and the Ian Sellers group for their contributions to the characterizations of the GaNP material.

My appreciation goes out to the countless staff who keep the laboratories running at Arizona State University, including Su Lin, Marco Flores, Emmanuel Soignard, Anthony Woolson, Xan Henderson, Araceli Vizcarra, Katarina Miller, Scott Ageno, Diana Convey, and Kevin Nordquist.

I want to point out that my work has been built upon the efforts of many facilities and custodial staff members that keep the university safe, clean, and functional. Thank you all!

Finally, I acknowledge that this material is based upon work supported in part by the Engineering Research Center program of the National Science Foundation and the Office of Energy Efficiency and Renewable Energy of the Department of Energy under NSF Cooperative Agreement No. EEC-1041895. The author acknowledges the use of facilities within the Eyring Materials Center at Arizona State University supported in part by No. NHCI-ECCS-1542160. The authors acknowledge resources and support from the Ultrafast Laser Facility, part of the Chemical and Environmental Characterization Core Facilities at Arizona State University.

TABLE OF CONTENTS

CHAPTER 1

INTRODUCTION

We live in a world rich in solar energy. Solar energy regenerates at 23 PW per year, compared to 0.1 for wind [1], as shown in 1, while our global consumption is currently at 0.02 PW annually. All other renewable energy sources fall far below this need. While gas, oil, uranium, and coal offer 0.2-0.9 PW, these are nonrenewable. Solar energy is by far the most plentiful potential source. Solar is growing fast, accounting for the largest proposition of electricity additions in the last year, beating natural gas and wind energy [2]. This growth in clean solar energy gives hope to limiting the devasting consequences of global warming that would occur with unrestrained use of fossil fuels.

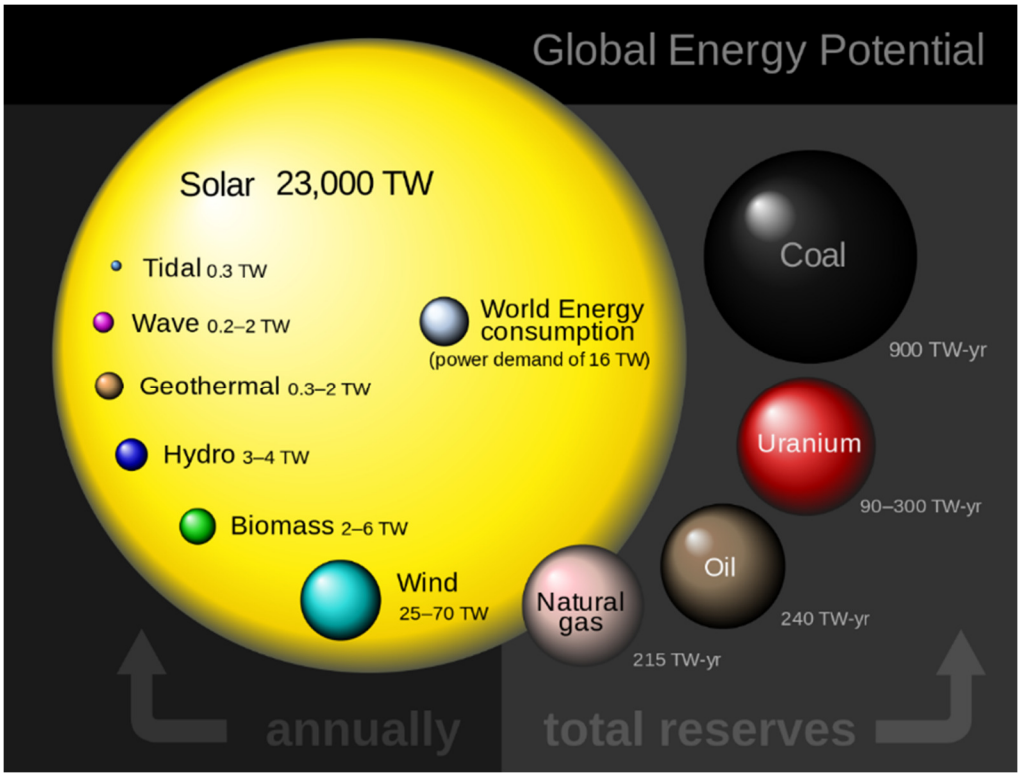

Fig. 1. Energy sources compared to world energy consumption [1]. The energy resource is proportional to the volume of each sphere.

Solar cells have versatile applications. Satellites, for instance, use solar cells as a sustainable source of energy. There is growing interest in integrating solar cells with drones or unmanned aerial vehicles (UAV). Solar can enable UAVs to be more autonomous, allowing for more activity before recharging [3]. Solar can also be used to power a diverse array of devices, powering what is known as the internet of things (IoT) [4]. IoT can link and synchronize sensors across an agricultural farm to expand responsive data collection. Beyond solar, photovoltaic (PV) cells can be used in other applications. Thermophotovoltaics (TPV) uses PV to convert light from a nearby hot source. TPV can be used in conjunction with fuel sources for microgenerators [5].

Photonic power converters (PPC) use PV for the transmission of energy. They convert laser light (or other monochromatic light) into electricity. PPCs can be integrated with optical fibers to transmit power alongside data. Energy transmission through an optical fiber to a PPC can withstand higher voltage or temperature environments than conventional electrical wires [6]. Outside of optical fibers, PPCs could enable wireless energy transfer [7]. Aeronautical institutions are interested in using PPCs for an automatized, wireless way of repowering drones and UAVs, as depicted in Fig. 2 [8].

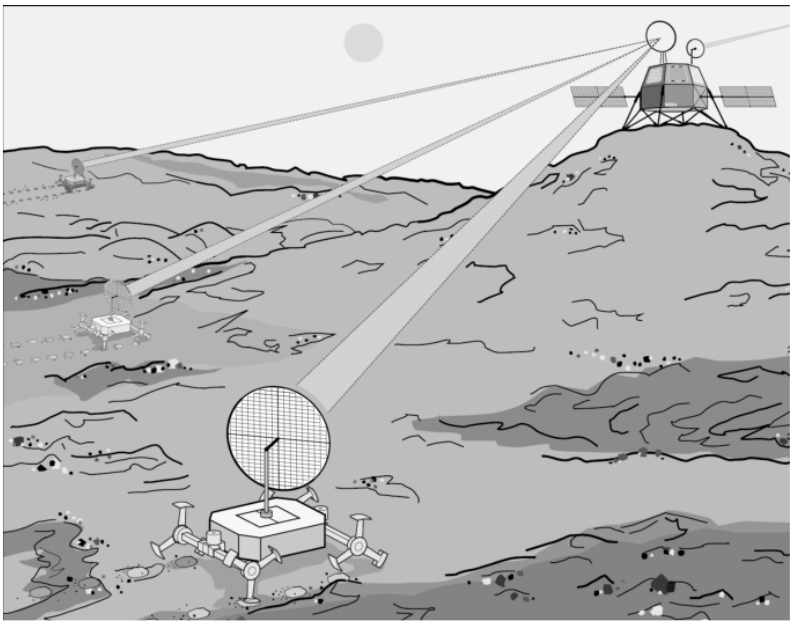

Fig. 2. Application of photonic power converter [8]. Wireless transmission of energy can enable autonomous, ranged repowering of lunar rovers.

Photovoltaics offers multiple uses, all of which can be improved by more careful light management. Silicon solar cells are textured to refract light into oblique angles, causing light trapping. When combined with a rear mirror, light trapping can drastically increase absorption. In a Lambertian light distribution, where light is scattered into isotropic directions, a semiconductor will absorb as much as a slab that is $4n^2 \approx 50$ times thicker [9]. Light trapping is critical for Si absorbers due to their indirect bandgap and low absorption coefficient. Even with light trapping, it usually must be made over 100 μm thick to reach near saturation of light. Most other PV materials, including GaAs, CdTe, CIGS, and perovskites, are direct bandgap materials. Many such thin films saturate in absorption at around 1 μm – even without light trapping. Nevertheless, light trapping in thin films would support J_{SC} while allowing for thinner absorbers – such as 0.1 μm. Thinner layers are expected to benefit from increased V_{OC} due to lower bulk recombination.

Light trapping can be made wavelength-selective, as has been shown to give benefits for tandem materials [10,11,12]. In this report, the relationship of wavelength-selective light trapping and the temperature of a photovoltaic material is investigated in detail.

First, the benefits of light trapping (Chapter 4) and its relationship with surface and bulk recombination (Chapter 5) are examined before addressing the relatively understudied topic of wavelength selective light trapping (WSLT). In subsequent sections, WSTL is further categorized into three regions with their associated physical phenomena: near and above-bandgap light for enhanced, reflection sub-bandgap light for the rejection of heat generation, and enhanced emissivity of low-energy, i.e., longwave light for radiative cooling. These spectral regions are presented in Figure 3.

The strategy of increasing photogeneration by focusing light trapping schemes on narrowband wavelength regions is developed in Chapter 6. The last two sections cover the thermal effects of WSLT.

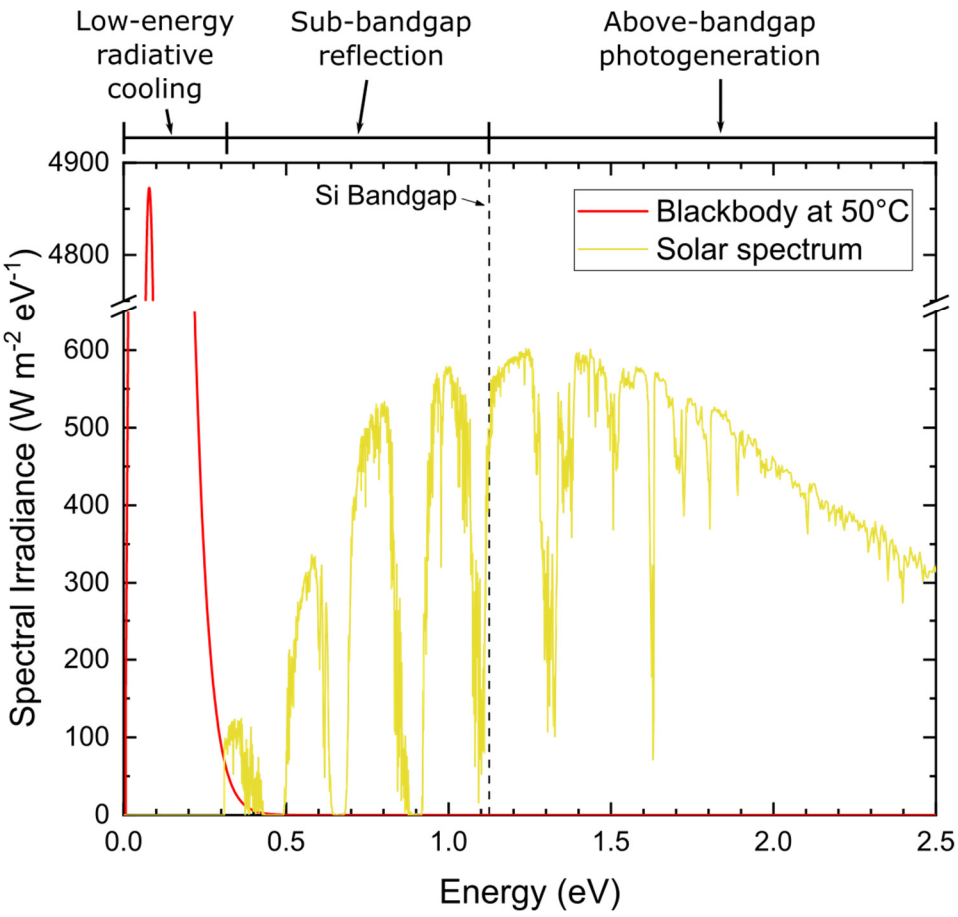

Fig. 3. Spectral regions for different wavelength-selective light trapping techniques.

Radiative cooling is a form of passive cooling for photovoltaics. Typically, the metric for increasing the radiative cooling is the glass emissivity, which in recent years has been brought close to unity through the strategy of texturing the front glass into micrometer patterns. In this report, the relative benefit of optimizing the emissivity over a narrower region of the wavelength spectra, known as the atmospheric window, will be examined within Chapter 7.

Another form of passive cooling is sub-bandgap reflection. As a significant portion of the solar spectrum is below the bandgap for single-junction solar materials such as CIGS (bandgap typically around 1.115 eV), crystalline silicon (1.125 eV), GaAs

(1.423 eV), CdTe (1.488 eV for polycrystalline or 1.504 eV for monocrystalline), perovskites (commonly 1.45-1.65 eV), and amorphous silicon (1.75 eV), maximal sub-bandgap reflection can yield significant benefits by lowering module for temperature, leading to more efficient and reliable devices. As is shown in Chapter 8, light trapping dramatically reduces sub-bandgap reflection by amplifying any present parasitic absorption.

CHAPTER 2

PREVIOUS WORKS

As a central material in this dissertation, the background starts with the benefits of light trapping, with a specific focus on Si cells where the process of texturing the material is particularly well developed. That section is followed by the historical development of GaAs cells light management, literature covering detailed-balance theory, light trapping fundamentals, surface recombination, photonic power converters, the impact of higher temperatures in PV, and the passive cooling mechanisms of radiative cooling and sub-bandgap reflection, which all have meaningful interactions with the absorption and emission of solar cells across the electromagnetic spectrum.

I. TEXTURING OF SI PHOTOVOLTAICS

While many other photovoltaic devices are direct bandgap and thus manufactured to be thin on the order of 1 μm or lower, crystalline Si is an indirect bandgap material and thus Si absorbers are made much thicker. Silicon absorbers are typically hundreds of microns thick, which enables the option of texturing micrometer features into the silicon layer. The textures of monocrystalline silicon are typically etched with alkaline solutions into pyramids on the order of 1-10 μm [13], while multicrystalline silicon is commonly etched with acidic solutions into micrometer-sized etching pits [14].

Texturing silicon has multifarious benefits. Front texturing reduces the external front reflection of the cells, allowing for more light to enter and be absorbed by the absorber layer [15]. Front texturing also scatters incident light into paths that will be absorbed closer to the front of the cell; and, as the front of the cell near the p-n junction

corresponds to the region of higher collection efficiency for some Si device architectures, front texturing can improve current collection [16]. Finally, texturing leads to light scattering outside of the material's escape cone, leading to light trapping through enhanced internal reflection at the front surface [17]. These mechanisms can all lead to an increase in PV current generation.

Another reason that silicon cells are typically textured can be seen from a manufacturing standpoint. After silicon ingots are sawed down into wafers, they will need to undergo saw damage removal to remove surface defects and impurities. For monocrystalline Si, an etching in KOH is used for both saw damage removal and the texturing of micrometer features [18], thus texturing incurs little to no added cost. In contrast, thin PV materials, such as amorphous silicon, copper indium gallium diselenide (CIGS), CdTe, and GaAs, are not conventionally cut from ingots and do not need the saw-damage removal step, meaning that texturing will likely incur added manufacturing steps for thin films. Additionally, thin-film thicknesses are on the order of a micrometer and are thus too thin for micrometer texturing features to be directly etched into the absorber. As such, thin films require alternative designs for light trapping.

II. Historical Development of GaAs Fabrication

The first reported GaAs solar cell was formed in 1956 by Cd diffusion into a single-crystal substrate [19]. These materials achieved efficiencies of around just 5%. Around 1970, Zhores Alferov developed GaAs into an AlGaAs/GaAs heterostructure, yielding up to 20% efficiency as well as a Nobel prize [20]. The heterostructure boosted efficiencies primarily by passivation of surface recombination [21]. A double-

heterostructure was later introduced in 1984, using AlGaAs on the front and back of the cell. The rear layer furthered passivated the device, bringing efficiency above 22% [22]. This innovation enabled the next development in GaAs cells: integration on a rear back mirror. The use of metal back reflectors, however, took until 2008, when it was finally achieved with an epitaxial lift-off technique, allowing for the double heterojunction to be removed from the substrate and placed on a metal reflector [23]. The rear mirror initially increased the efficiency to 26.1%. Further optimizations upon the mirror led to 29.1% [24] – a result quite close to the theoretical efficiency limit of 33.77% [25].

The historical development in GaAs solar cell design is depicted in Fig. 4, as adapted from Ref. [26]. Over time, the active region has become increasingly confined, both electrically and optically. The next step in this progression (from the author's perspective) is light trapping to enable ultra-thin photovoltaics. Light trapping is traditionally not used in direct-bandgap materials including GaAs, CdTe, CIGS, and perovskites. As a direct-bandgap semiconductor, GaAs can achieve high absorption with thickness as thin as 3 μm. The process for texturing Si (anisotropic etching of 1-10 μm features into the absorber) becomes challenging for such thin material.

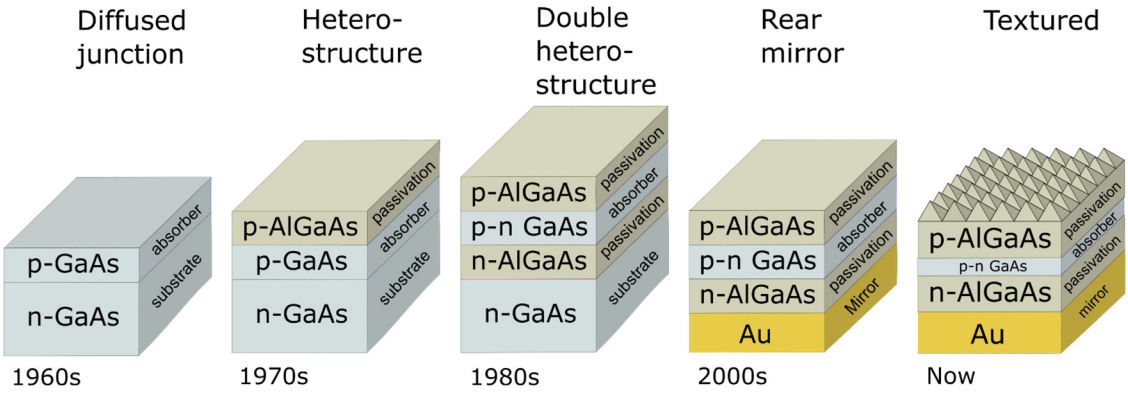

Fig. 4. History of GaAs photovoltaic innovation, showing increasingly confined active regions. Adapted from Yamaguchi [26].

Light trapping has been demonstrated in GaAs (and other thin films) with other methods. In 2013, Eyderman et al. simulated 200 nm GaAs cells that could achieve near-full absorption with a photonic crystal [27]. The following year, Yang et al. demonstrated experimental light trapping for a 300 nm GaAs layer, reaching 19.1% efficiency [28]. The light trapping there utilized a textured surface that grew naturally during the growth of a 5-μm thick AlInP layer. Later, in 2019, Chen et al. achieved a 19.9% efficiency GaAs efficiency with a 200-nm absorber on a nanostructured back mirror [29]. That same year, Eerden et al. achieved 21.4% at 300 nm with a relatively facile wet chemical process for texturing the GaAs back mirror [30].

Although light trapping has been demonstrated to boost efficiency at 200-300 nm absorber thickness, light trapping did not appear to increase the maximum efficiency of the devices. The efficiencies with light trapping in these studies (19-21%) fall far below that achieved by cells without light trapping (25-29%). So, higher efficiencies could generally have been achieved simply with thicker, planar absorbers. Furthermore, these innovations in light trapping have not penetrated commercial manufacturing. The benefits of enhanced absorption (and thinner layers) have not yet exceeded the negative impacts of light trapping and its processing. So, in this work, the question is not whether light trapping can be made in thin films – the question is when – and how – light trapping should be done.

III. Radiative Recombination and The Principle of Detailed Balance

The principle of detailed balance equates light absorption with light emission at each energy and angle [31]. Within photovoltaics (PV), detailed balance is used to

determine a PV cell's radiative recombination current density J_{rad} from the difference in the photon flux emitted and absorbed by the material. At equilibrium, these fluxes cancel, with magnitudes equal to the product of the cell's absorptance and the blackbody photon flux [32,33,34]. Out of equilibrium, the conventional treatment of detailed balance considers the emitted flux to scale with the exponential of the applied voltage. Specifically, this "volt model" for radiative recombination is

$$J_{\mathrm{rad,front}} = q \int_0^\infty A_f(V,E)\, b(E) dE \left(e^{\frac{qV}{kT}} - 1\right), \tag{1}$$

where E is the photon energy. The equations for the absorptance of light from the front A_{f} and the blackbody photon flux b are detailed in Section 3.I. V is the voltage applied across the cell, minus losses to parasitic resistances, which can also be thought of as the quasi-Fermi level splitting in the cell absorber, divided by the fundamental charge q.

$J_{\mathrm{rad,front}}$ is the current density loss corresponding to photons emitted by radiative recombination that are lost due to absorption or transmission at the front of the cell. A similar equation can be written for the current loss due to light absorption or transmission at the rear of the cell, $J_{\mathrm{rad,rear}}$, is given in Section 3.I.B. The sum of $J_{\mathrm{rad,front}}$ and $J_{\mathrm{rad,rear}}$ gives the net radiative recombination J_{rad}, which incorporates the effect of photon recycling to reduce the recombination density.

Although the volt model incorporates photon recycling, it neglects the phenomenon of carrier transport. Technically, the radiative emission from a point in a material scales with the quasi-Fermi level splitting – not the applied voltage [35,36,37]. A more accurate model for radiative recombination considers the variation of the quasi-Fermi-level splitting (QFLS) through the absorber. Namely, the "QFLS model" for radiative recombination is

$$J_{\mathrm{rad,front}} = q \int_0^{\infty} A(V,E)\, b(E) dE \int \frac{1}{W} \left(e^{\frac{\Delta\mu(z)}{kT}} - 1 \right) dz \qquad (2)$$

where $\Delta\mu$ is the quasi-Fermi-level splitting and W is the absorber thickness. The integral over the depth into the absorber z averages over the generalized Planck law to account for variation in the QFLS.

The detailed-balance limit published by Shockley and Queisser compares the photovoltaic potential of absorber materials based solely on their bandgap [38]. For the AM1.5G solar spectrum, these calculations yield a peak theoretical solar cell efficiency of 33.6%, with efficiencies above 30% for 0.92 to 1.64 eV. Many materials lie within this bandgap range, including Si, GaAs, CdTe, and copper indium gallium diselenide (CIGS). In 2018 silicon photovoltaics captured 95.8% of global photovoltaic power, with CdTe at 2.9% and CIGS at 1.1% [39]. GaAs solar cells provide far less energy, but they make up a large portion of the high-value cells deployed on satellites and space stations. A GaAs cell also holds the record efficiency for single-junction solar cells at 29.1% [40]

The calculations in the original paper by Shockley and Queisser assume that no photons below the bandgap energy are absorbed, while all photons above the bandgap energy get absorbed. This approach neglects the critical role of absorber thickness on cell performance. Instead, one can utilize the absorption coefficient for a material with a given thickness to calculate the absorptance – defined as the fraction of photons absorbed at each energy, as indicated in Equation 1. The absorptance can be calculated based on the absorption coefficient, thickness, and rear-mirror reflectance under a planar or Lambertian model for the light distribution.

IV. Previous Works on Light Trapping and Device Modeling

Absorptance can be increased through light trapping, which is done with the introduction of rear reflectors as well as structures that deflect incident light into oblique paths. The light that is completely diffused is isotropic, and the flux of isotropic radiation through a surface is a Lambertian distribution. Thus, a Lambertian light distribution (LLD) represents an upper limit for absorptance enhancement [41]. For the sake of brevity, this report will refer to 'cells that bring incident light into an internal Lambertian light distribution' as 'Lambertian cells.'

While nanostructures have been showed to surpass the Lambertian limit for specific incidence angles [42] or energy intervals [43], they yield lower absorptances when averaged over the angles or energies that are relevant for solar power generation. Cells that are textured on the front and back effectively achieve an LLD [44]. Texturing procedures are well-established for silicon, but achieving an LLD within a thin film is limited to nascent techniques such as rear-embedded nanostructures [45]. By comparing cells with and without an LLD, one can determine conditions for which an absorber material would benefit from texturing or rear-embedded nanostructures.

The impact of unavoidable non-radiative recombination in a material such as Auger recombination has been considered via thickness-dependent calculations of absorptance. At sunlight concentrations around 1 sun, the Auger recombination current is 10,000x greater in intrinsic, undoped silicon than in intrinsic GaAs. The increased Auger recombination in silicon is due to its low bandgap, which yields a high intrinsic carrier concentration, as well as its indirect bandgap, which requires thicker absorbers, and thicker absorbers yield more Auger recombination [46]. The presence of Auger

recombination in silicon was shown to decrease the fundamental efficiency of silicon from 32.2% to 29.4% [47]. A consideration of wafer resistivity lowers the limit to 29.1% [48], but alternatively, more in-depth modeling of the Lambertian distribution brings the efficiency limit up to 29.6% [49].

The overall impact of texturing and an LLD depends on how much it affects the absorption, the carrier collection, the optimal thickness, and the surface recombination of the photovoltaic device.

V. Previous Works on Measuring Surface Recombination

The parameter used to characterize a material's surface recombination is the surface recombination velocity (SRV). The surface recombination velocity S is a normalized metric of the surface recombination current density J_{surf} given by $S = \frac{J_{\text{surf}}}{qn_{\text{min}}}$ where n_{min} is the minority-carrier concentration. The SRV thus gives an indicator of the dependence of surface recombination current density on the carrier concentration n, useful as the carrier concentration can scale exponentially with voltage.

The impact of SRV generally has three regimes when plotted considering its effect on the efficiency of a device, with shape of a sigmoid when plotting efficiency versus the logarithm of the SRV. 1) At low SRV values, proportional increases in the SRV are relatively inconsequential to the efficiency of the device as surface recombination will not be the dominant part of the total recombination current. 2) At moderate SRV values, increasing SRV values will lead to drops in the device efficiency. The boundary between regimes of 'low' and 'moderate' SRV values is where the surface recombination current density goes from being a negligible to a considerable part of the

total recombination current [50,51]. 3) At higher SRV values, the efficiency will go towards an asymptotic value. There, higher SRV will have a vanishing impact because the recombination at the surface will be limited by transport of carriers to the surface instead of by recombination of the carriers. The difference between 'moderate' and 'high' SRV values here is characterized by the SRV being greater than or equal to the diffusion velocity D/L. In summary, changes to the SRV only have a significant effect on efficiency when it varies across moderate values of SRV.

Surface recombination velocity in III-V materials is commonly measured by photoluminescence. As a background to this technique, this section will present literature results on the surface recombination of the material GaNP through time-resolved photoluminescence (TRPL).

The dilute nitride material $GaN_{0.02}P_{0.98}$ provides lattice matching with Si [52] and a nearly ideal bandgap for use in a two-junction, three-terminal configuration [53]. The record GaNP efficiency has been 7.9% [54] in a p-GaP/i-GaNP/n-GaP device grown on a GaP substrate; but the record drops to 0.7% for GaNP cells grown on a Si substrate [55]. The GaNP-on-Si cell suffered a high bandgap-voltage offset, W_{oc}, of 1.15 V, which indicates carrier lifetime as a key metric for GaNP on Si. GaNP grown on GaP substrates has demonstrated room-temperature lifetimes of 10 ns [56] and below [57]; but layers grown on Si have exhibited lower carrier lifetimes - estimated at room temperature as 0.01 ns through the fitting of the EQE in [55]. The lower lifetime of GaNP on Si substrates may result in part from the heterovalent interface at the GaP/Si interface.

Research has repeatedly shown the importance of annealing in improving dilute nitride material systems, but optimal annealing conditions change with defect activation

energy and material thickness. My results in Ref. [58] present photoluminescence across different annealing conditions.

Hydrogenation has been used to improve carrier lifetime - especially for silicon [59]. It has also been shown to be useful for delocalizing carriers in III-V dilute-nitride materials, including GaInNAs [60]. Hydrogen may either passivate or activate defects. For example, GaNP on GaP hydrogenated using ion-beams showed activation of new defects [61]. In Section 5.I, the benefits of annealing and hydrogenation of GaNP/Si are assessed with TRPL.

VI. Previous Works on Photonic Power Converters

PPCs can be far more efficient than solar cells, with a theoretical PPC efficiency of 91% at 100 W/cm^2 [62] compared to 34% efficiency for a single-junction solar cell at 1 sun. A PPC runs efficiently because the incident monochromatic light can be tuned to the PPC absorber bandgap, in contrast to sunlight that has energy that is too high or too low to be efficiently absorbed. Record PPC efficiencies include 70% for a multijunction device [63] and 68.9% for a single-junction device achieved in 2021 [64], but they still have room to reach their theoretical maximum. Further enhancements can be made by increasing absorption as well as reducing recombination and parasitic resistance. A strong enhancement of absorption enables thinner cells, which are less sensitive to bulk material quality.

Conventional Si solar cells create light trapping with KOH wet etching, creating random pyramids resulting in isotropic light scattering after several internal reflections. Due to internal reflection, these materials can in principle have an internal path-length

enhancement of nearly 50x, which has become critical to maximizing absorption in silicon with an indirect bandgap. (The path-length enhancement is the ratio between the effective absorber thickness and the actual absorber thickness. Planar cells with perfect rear reflectors give a 2x enhancement due to a double pass through the absorber). While nanophotonics has been used to achieve path-length enhancement over 50x (the Lambertian limit) in narrow energy ranges for Si, only this past year in 2022 has the effect been optimized for a device that operates solely within a narrow energy range [65]. Furthermore, III-V devices (which, due to their high performance, are the standard materials used in PPCs) have never achieved a path-length enhancement over 12x [28], [29], [30], [66].

This project is distinct from earlier work on nanophotonic light trapping because it applies light trapping to PPCs, where there is only one incident energy of light to scatter. Theoretically, this allows for extreme path-length enhancement by targeting solely the photon energy of the laser or other monochromatic light source. Such a breakthrough would yield drastic improvements in absorption while also enabling thickness and bulk recombination reduction. Hence, this project could lead to a paradigm shift in the development of PPCs. Insights may well extend from PPCs to other optoelectronics – especially light trapping for solar cells.

Recently, the first works on PPC light trapping have been published. In 2020, Takeda showed that PPCs could exhibit 1200x path-length enhancement [67]. This is a drastic increase over the path-length enhancement in the Lambertian limit for an isotropic light distribution. Takeda achieved this value with simulations of an angularly selective filter deposited on top of a flat GaAs cell, which was itself integrated with a diffuse rear

reflector. This seminal paper demonstrates the exciting possibilities for light trapping in PPCs. However, the 1200x value assumes a stack without any parasitic absorption, and the rear surface is assumed to be 100% reflective. Furthermore, the angular selective filter requires the deposition of a stack of 43 dielectric layers, and the sensitivity of performance to small variations in the layers has not yet been assessed. Alternative designs were proposed by Nouri et al. in 2021 [68]. They simulated nanostructures on the rear mirror, yielding a path-length enhancement of 7.8x. Cavity resonances were said to be responsible for the recent breakthrough record in PPC efficiency, but the spectral response curve shows a path-length enhancement of only 1.9x. Until this year, a path-length enhancement above 2x has not yet been experimentally demonstrated for a III-V PPC [69] – and PPCs are generally made with III-V material.

The investigation of narrowband light trapping will be a primary topic in the work reported here – along with an examination of the interaction between light trapping, sub-bandgap reflection and the thermal behavior of photovoltaics.

VII. Summary of the Thermal Dependence of Photovoltaics

Higher temperatures tend to lead to lower efficiencies [70] and higher degradation rates [71] for most photovoltaic materials. The overall temperature dependence of PV cell power is a function of the temperature dependence of the open-circuit voltage, fill factor, and short-circuit current. While the short-circuit current often increases with temperature due to a decrease in the material bandgap, and the fill factor can increase or decrease with temperature (most commonly decreases), the overall temperature effect is almost always negative due to strong decreases in the open-circuit voltage [72].

For most high efficiency PV technologies, the open-circuit voltage is responsible for 80-90% of the overall change in the PV efficiency with temperature [72]. While the change in V_{OC} with temperature is a product of a change in many device parameters, including the diffusion length, doping concentration, and the width of the depletion region, in many cases the primary thermal effect is found to come from the increase in the intrinsic carrier concentration with temperature [73]. At higher temperatures, more carriers are thermally excited, leading to a higher equilibrium recombination current density, i.e., a higher diode saturation current density – and thus a lower open-circuit voltage. The next two sections will overview two passive cooling mechanisms for reducing temperatures in photovoltaics.

VIII. Previous Works on Enhanced Infrared Emissivity

The ability to reduce a material's temperature by tailoring the spectral emissivity of its surface has been scientifically established since at least 1975 [74]. If the material is insulated from conduction convection and with the surrounding environment, selective emissivity enables its temperature to be brought well below that of the ambient temperature [74,75]. The ability to shape the emissivity spectrum can be achieved through designs includes plastic coatings [74], micro-textured glass [76,77], and photonic crystals [75,78,79]. In the last decade, literature on radiative cooling has greatly expanded since the advent of photonic crystals in the design of selective emitters. Many more selective emitter designs can be found in the comprehensive review by Sun et al. [80].

Much of these advances involve designing an emissivity that is high in the atmospheric window, i.e., the 8-13 μm range where the atmosphere is transparent. In that

range, the downwelling longwave radiation from the sky is low, allowing the material to absorb less longwave radiation from its environment than it emits. In sum, the net radiative flux out of a selective emitter increases, yielding a lower temperature than that than the case where the emissivity is high outside of the atmospheric window [80].

In general, the ideal emissivity of a module depends on whether the module temperature is higher or lower than the surrounding ambient. If the module temperature is significantly lower than the ambient temperature (about 0-5°C lower), then a selective narrowband emissivity at the atmospheric window leads to the lowest temperatures; but when the module temperature is near or above the ambient temperature then a broadband emissivity of 1 leads to lower temperatures [80]. Note, for materials under solar irradiance, the emissivity should be 0 for wavelengths λ over 4.5 μm to avoid heat generation through absorption of sunlight, so the "broadband" emissivity is really a step function. For photovoltaics under full sunlight, module temperatures are expected to be above ambient temperatures, so the broadband emissivity of 1 for $\lambda > 4.5$ μm is ideal. Nevertheless, an understanding of the ideal selective emissivity yields insights into how to best optimize a module's emissivity even when the ideal emissivity is broadband, as seen in Chapter 7.

It was shown in 2020 that the ideal selective emissivity for below-ambient cooling is not exactly a flat band in the atmospheric window, but is a series of discrete, infinitesimal peaks in emissivity [81]. Moreover, the wavelengths of the peaks change with environmental conditions. Such a complex emissivity spectrum allows for the atmospheric window to be divided up into smaller wavelength ranges, giving greater resolution for the true transmittance of the atmosphere. The higher resolution gives

higher control in turning on *or* off radiation at a particular wavelength to emit radiation *or* to block absorption of incident longwave radiation, depending on the relative magnitude of the sky downwelling radiation to the blackbody radiation at that wavelength. Compared to an emissivity that is one in the atmospheric window and is zero elsewhere, this ideal, discrete selective emissivity can give significant temperature gains. 25°C is the calculated difference between the simple and the ideal selective emitter under one sun and with the condition that there is no conduction or convection to the surrounding environment. However, the temperature gains decrease to zero quickly if relatively low values of convection are considered, such as 3 W m^{-2} K^{-1}. So, while a flat, high emissivity in the atmospheric spectrum is not the absolute ideal selective emissivity, it leads to a nearly identical temperature as the ideal emissivity. A flat, high emissivity in the atmospheric window can thus be considered as close approximation of the ideal selective emissivity for typical photovoltaics scenarios.

In the current work, presented in Chapter 7, the potential gains of radiative cooling are assessed, with a particular emphasis on quantifying the normalized impact of the emissivity inside versus the outside of the atmospheric window. The modeled gains of radiative cooling will then provide context for Chapter 8, which examines an alternative passive cooling technique – that of sub-bandgap reflection.

IX. Previous Works Sub-Bandgap Reflection

Recently, solar panels have been deployed in a growing variety of thermal configurations. While standard test conditions (STC) consider module temperature to be 25°C, vehicle-integrated solar can face temperatures over 85°C [82]. These temperatures

can occur when an insulated rear surface reduces overall cooling. Insulated configurations thus run hotter than conventional open-rack configurations, where modules experience convective and radiative cooling at their rear surface. Building-integrated photovoltaics lie between open-rack and fully insulated configurations, depending on ventilation [83].

Insulated configurations call for innovative designs to reduce the performance loss that occurs with higher temperatures [70]. Crystalline silicon experiences a greater loss in efficiency with operating temperature compared with CdTe and GaAs [73]. GaAs, the core material for space applications [84], is very expensive but offers multiple performance advantages over Si. These advantages include higher power density, lower sensitivity to module temperature, and lower module operating temperatures. The two main effects causing a low operating temperature in GaAs modules are a high V_{oc} [85] and a high sub-bandgap reflectance [86].

Sub-bandgap reflection has been argued as a particularly effective way to lower module temperatures [86],[87],[88],[89],[90]. These reports have focused on open-rack configurations. The report in Chapter 8 evaluates the impact of sub-bandgap reflection across thermal configurations. It is argued that light trapping severely limits the benefits of sub-bandgap reflection for Si temperatures – a novel contribution to the literature. Results are published in IEEE Journal of Photovoltaics [91].

CHAPTER 3

METHODS

The various methodologies used in the underlying research will be detailed here.

I. Detailed Balance Modeling

The general theory of detailed balance is explained in Section 2.III. The detailed balance methods detailed here can be organized into A) conventional detailed balance B) detailed balance with limited carrier collection C) material parameters.

A. Detailed-Balance Equations

Solar cell efficiencies are calculated by maximizing power density as a function of voltage V with the general equation

$$JV = \left(q \int_0^\infty (A_\mathrm{f} S - A_\mathrm{f} B - A_\mathrm{r} B') dE \; - \; J_A \right) V, \tag{3}$$

where A_f is both the absorptance in the absorber material of light incident from the front, which is equal to the emittance of light from the semiconductor bulk to the front according to Kirchhoff's Law [31]. A_r is the emittance from the semiconductor bulk to the rear, determined analytically from the absorptance of light from the rear of the absorber material. J_A is the Auger recombination current density. Shockley-Read-Hall recombination, surface recombination, and resistance losses can be integrated in a straight-forward manner, but the current work focuses on intrinsic loss mechanisms.

S is the incident sunlight taken as the AM1.5G spectral photon flux ($s^{-1}\ m^{-2}$) without sunlight concentration [92], whereas *B* is the cell's blackbody radiation,

$$B = \frac{2\pi}{c^2 h^3} \frac{E^2}{e^{\frac{E-qV}{kT}} - 1}, \tag{4}$$

with cell at room temperature, T = 298.15 K. This equation is valid for emittance into the cell's front, where Snell's Law dictates that $1/n_r^2$ of isotropic photons emit from the semiconductor with an index of refraction n_r with $1\text{-}1/n_r^2$ of photons reflected by the semiconductor-air interface. The change in front internal reflectance due to ARC layers between the semiconductor and air is negligible to the first order [44]. Photons emitted into the rear substrate do not, however, necessarily face such a reflective interface, so the rear blackbody radiation is scaled with the index of refraction n_r as $B' = n_r^2 B$ [93]. In calculations, the Maxwell-Boltzmann approximation $(e^{\frac{E-qV}{kT}} - 1)^{-1} \approx e^{\frac{-E+qV}{kT}}$ is used in favor of the Bose-Einstein expression because the Bose-Einstein statistics become numerically dense at the singularity near energy $E = qV$.

Photon recycling is automatically considered through calculation of radiative recombination as the energy-resolved product of absorptance with the blackbody photon flux through a surface. Photon recycling needs to be calculated separately if one instead calculates radiative recombination from the bulk recombination rate and the radiative recombination coefficient.

Equations for absorptance and emittance for both the front and rear for both planar and Lambertian cases are derived from Eq. 5 of Martin Green's 2002 paper [94], rewritten as

$$A = (1 - R_{ext}) \frac{(1 - e^{-\alpha L})(1 + R_b e^{-\alpha L})}{1 - R_b R_f e^{-2\alpha L}}, \tag{5}$$

with α the absorption coefficient and L the path length taken by a photon through one pass across the absorber. Here, an assumption is made that the transmission of light as it travels across the bulk is the same in the downwards and upwards direction, i.e., in terms of Green's symbolism, $T^{+} = T^{-}$.

A material's emittance is equal to the absorptance resolved by energy and angle as per the principle of detailed balance. One determines the equation for each case by identifying the path length and reflectances as depicted in the figure below, and the resultant expressions are given in Equations (6)-(9). In the Lambertian cases, photon directions are considered to randomly redistribute each time they reach the front surface. In practice, it makes negligible difference to J_{sc} whether such diffraction occurs at the front or back [44].

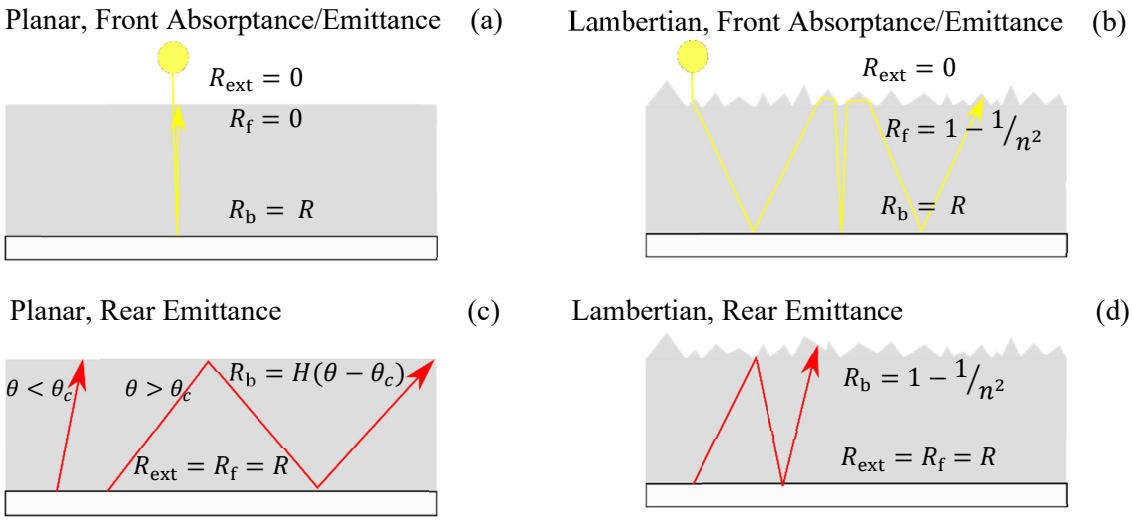

Fig. 5. Internal light distribution scenarios (a-d) and corresponding external, front, and back reflectance values for deriving absorptance/emittance to the front a and emittance to the rear a′ with Equations 6-9. The emittance to the rear is found as a hypothetical absorptance from the rear surface of the absorber.

The figure above depicts the absorptance and emittance from and to the front of a planar cell, useful for deriving the four equations below. The equations for absorbance

and emittance are given in their angularly-averaged form, but the quantities of A_{f}, A_{r}, α, R, and n_{r} are considered to be functions of photon energy.

Planar, Front Absorptance/Emittance

$$A_{\mathrm{f}} = (1 - e^{-\alpha W})(1 + Re^{-\alpha W}). \quad (6)$$

Lambertian, Front Absorptance/Emittance

$$A_{\mathrm{f}} = \frac{(1-e^{-\alpha L_t})(1+Re^{-\alpha L_{\mathrm{t}}})}{1-R\,(1-1/{n_{\mathrm{r}}}^2)\,e^{-2\alpha L_{\mathrm{t}}}}. \quad (7)$$

Planar, Rear Emittance

$$A_{\mathrm{r}} = (1 - R)\int_0^{\frac{\pi}{2}} 2\sin\theta\cos\theta\, d\theta \times \frac{(1-e^{-\alpha W/\cos\theta})(1+H(\theta-\theta_c)e^{-\alpha W/\cos\theta})}{1-R\,H(\theta-\theta_c)e^{-2\alpha W/\cos\theta}}. \quad (8)$$

Lambertian, Rear Emittance

$$A_{\mathrm{r}} = (1 - R)\frac{(1-e^{-\alpha L_{\mathrm{t}}})(1+(1-1/{n_{\mathrm{r}}}^2)e^{-\alpha L_{\mathrm{t}}})}{1-R(1-1/{n_{\mathrm{r}}}^2)e^{-2\alpha L_t}}. \quad (9)$$

We assume zero external front reflectance through an ideal anti-reflection coating, but an empirically measured external front reflection could be readily substituted for $\mathrm{R_{ext}}$. In the planar case, light that transmits from the front will also transmit out the front by symmetry, hence the internal front reflection is 0. The rear surface reflectance is R. The path length is roughly the absorber thickness W due to strong refraction within a semiconductor.

For the Lambertian cell of Fig. 5(b), diffraction enhances the effective path length of a photon traveling across the cell to

$$L_t = \frac{2+0.935(\alpha W)^{0.67}}{1+0.935(\alpha W)^{0.67}} W, \quad (10)$$

because the path extends into oblique angles with the average path length dependent on absorption [94]. The internal front reflection of the Lambertian case becomes $1 - 1/n_r^2$, i.e., the chance a photon lies outside of the surface's escape cone. In the limit that αW → 0, Eq. 5 simplifies to Yablonovitch's $4n_r^2$ limit for path-length enhancement [41].

In Figures 5 (c) and (d), the emittance to the rear is found as hypothetical absorptance from the rear substrate, because they are equal through the detailed-balance principle [95]. The cell is conceptually reoriented with R_b at the cell's front and R_{ext} and R_f now being the rear reflectance R. As bulk radiative recombination is isotropic, in both the planar and Lambertian rear cases, the photons are considered to originate in a Lambertian distribution, but only in Lambertian cells does the light redistribute into a Lambertian distribution with each pass. Fig. 5(d) identifies R_b with $1 - 1/n_r^2$, as the reflection for an LLD by the semiconductor-air interface, but for the planar case of Fig. 5(c), this identification cannot be made as the light distribution is Lambertian for only the first pass. Instead, the rear planar case is solved by considering the angle Θ with the normal for each possible photon path. The reflectance R_b changes from 0 to 1 for angles over the critical angle $\Theta_c = \arcsin(1/n_r)$, which is incorporated by the Heaviside step function $H(\Theta - \Theta_c)$. The $\sin\theta$ is used for integrating within spherical coordinates, the $\cos\theta$ arises from the projection of isotropic radiation onto a Lambertian surface, and the 2 results from the normalization of the $\sin\theta\cos\theta$ space. The redistribution in the rear Lambertian case allows for effective expressions for R_b and L, thus making integration unnecessary, which quickens computation time by an order of magnitude.

Equations 6 and 8 correspond with the planar equations used by Miller [96]; Eq. 7 corresponds with the front Lambertian equation used by Schafer [49], whereas Eq. 9 is a new development.

Finally, the Auger current density is calculated from Ref. [46] as

$$J_A = qCWn_i^3 e^{\frac{3qV}{2kT}}, \tag{11}$$

with Auger recombination coefficient C and intrinsic carrier concentration n_{i} given in the Section 3.I.C. The Auger recombination for silicon, as a more substantial current, is calculated more precisely using (18) of the Richter parametrization [97].

B. Detailed-Balance Unified with Diffusion Modeling

The previous section presents the detailed-balance theory used in the earlier conference paper, Ref. [98]. The following section presents part of my published formulism for merging detailed balance with the diffusion model, as published in Ref. [99]. The algorithm is made available for download on GitHub platform at https://github.com/npirvin/Radiative-Transport-PV.

The core algorithm is depicted in the figure below. Nonlinear dependencies between radiation and transport are solved through iterative calculations, with the convergence target in L set at 0.01%. The models for radiative and nonradiative recombination are used to determine the bulk lifetime. Then, the lifetime is combined with the diffusivity models to calculate the diffusion length. Finally, the diffusion length is used to determine carrier concentrations and the current density J by using an analytical solution adapted from Kowalczewski et al. [100].

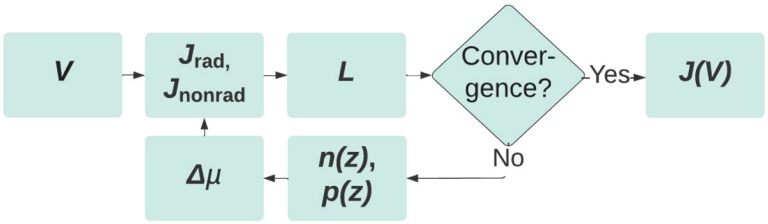

Fig. 6 Depiction of the algorithm flow, showing feedback between radiative recombination J_{rad} and diffusion length L. The volt model allows for a first calculation of the radiative recombination J_{rad}, whereas the quasi-Fermi level splitting $\Delta\mu$ can be used for a more accurate calculation after the depth-dependent carrier concentrations n, p are found.

For the sake of generalization, we consider the semiconductor to consist of a single absorber region with generic auxiliary layers, as illustrated in the figure below. Results assume a perfect anti-reflective coating (ARC) and an ideal front contact. The rear contact is assumed to be perfectly conductive, but its surface recombination velocity (SRV) is used to parametrize the contact quality. Generic contacts enable the comparison of different absorber qualities without presupposing contact architecture, such as p-n junctions, heterojunctions, and carrier-selective contacts, which would be different for each absorber.

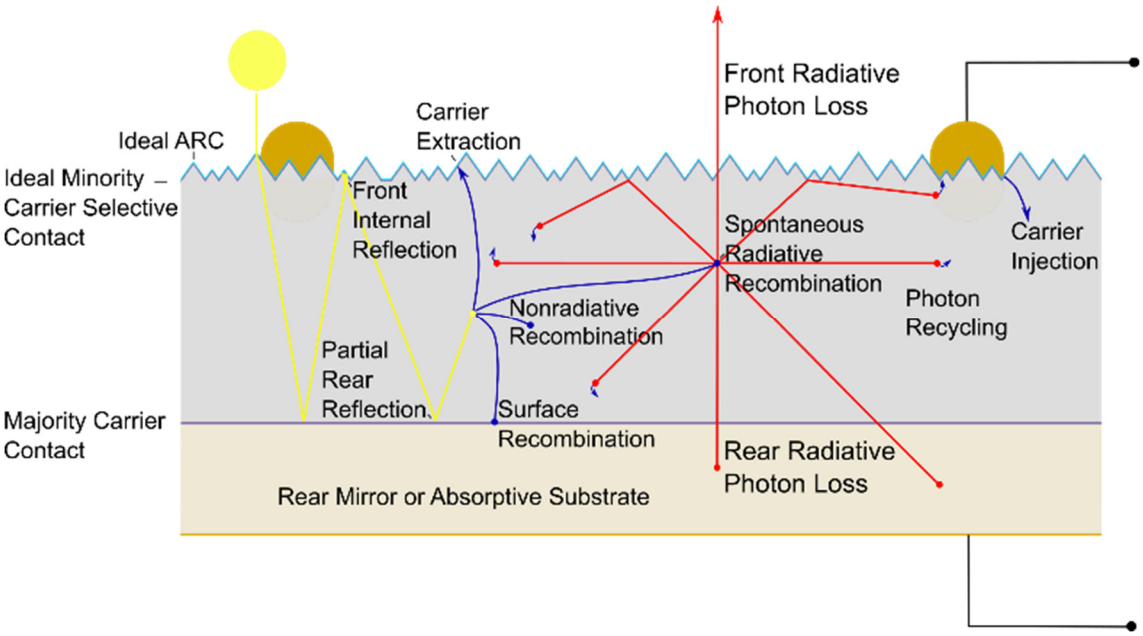

Fig. 7 Representation of the physical models used in the algorithm. Yellow lines indicate incident photon paths, red lines represent internally generated photons from radiative recombination, while blue curves symbolize electron movement. An ideal carrier selective contact is placed at the front surface of the absorber material, while nonidealities of the contacts are incorporated by surface recombination at the rear only.

We acquire an analytical solution to the diffusion equation by assuming the electric field to be zero across the absorber. The simplifications used at the interfaces allow for rapid calculations and comparisons across absorbers.

The net radiative recombination current density is

$$J_{\mathrm{rad}}(V) = J_{\mathrm{rad,front}} + J_{\mathrm{rad,rear}} + J_{\mathrm{rad,FCA}} \tag{12}$$

where $J_{\mathrm{rad,FCA}}$ is the current density corresponding to photons from radiative recombination lost by free carrier absorption (FCA), or other parasitic light absorption mechanisms which do not generate electron-hole pairs. The FCA term is typically negligible. The methods for calculating each term are detailed in Ref. [58], Appendix A2. This approach above uses detailed balance for radiative recombination. Alternatively, net radiative recombination can be found as spontaneous radiative recombination minus the photon recycling current density [101]. Detailed balance offers a more direct determination of net radiative recombination than by explicitly considering photon recycling.

$J_{\mathrm{rad,front}}$ is the radiative-recombination current density corresponding to photons lost due to transmission or absorption at the front. On first iterations of the algorithm, $J_{\mathrm{rad,front}}$ is found with Eq. 1, on subsequent iterations it is found with Eq. 2. Similarly, the radiative-recombination current density corresponding to photons lost due to transmission or absorption at the rear is found as, $J_{\mathrm{rad,rear}}$ is found with

$$J_{\mathrm{rad,rear}}(V) = \begin{cases} q\int_0^\infty A_{\mathrm{r}}(V,E)n_{\mathrm{r}}^2 b(E)dE\ \left(e^{\frac{qV}{kT}} - 1\right), & \text{first iteration} \\ q\int_0^\infty A_{\mathrm{r}}(V,E)n_{\mathrm{r}}^2 b(E)dE \int \frac{1}{W}\left(e^{\frac{\Delta\mu(z)}{kT}} - 1\right)dz, & \text{subsequent.} \end{cases} \tag{13}$$

$J_{\mathrm{rad,rear}}$ goes to 0 for cells with an ideal rear reflector. However, the rear radiative current loss, $J_{\mathrm{rad,rear}}$, often exceeds the front radiative current loss, $J_{\mathrm{rad,front}}$, due to the significant internal reflection that occurs at the front interface. For materials with a large index of refraction, such as GaAs and Si, the rear reflectance must be over 92% to bring the rear radiative current loss below that of the front [102].

The net radiative lifetime τ_{rad} (which incorporates photon recycling) is calculated from the excess carrier concentration $\Delta n(z)$ through

$$\tau_{\mathrm{rad}}(V) = \begin{cases} q\ W\ \Delta n(0)\ /\ J_{\mathrm{rad}}, & \text{first iterations} \\ q\ \int \Delta n(z)dz\ /\ J_{\mathrm{rad}}, & \text{subsequent iterations} \end{cases} \quad (14)$$

where W is the absorber thickness. The excess carrier concentration Δn is first found at the minority carrier contact in by the Law of Mass Action and then found throughout the absorber in Equation 23. The excess carrier concentration is sampled across 201 points through the material.

In a previous model on incorporating photon recycling and the diffusion model, [103] subsequent iterations were not used. That method gets the radiative lifetime by using assuming low-level injection. The iterative method presented here extends the analysis to high-level injection by determining the radiative lifetime from the radiative recombination current density.

The procedures for the other recombination processes are detailed in Ref. [58], Appendix A2. Trap-assisted recombination (also known as Shockley Read-Hall (SRH) recombination) is parametrized with a fixed lifetime $\tau_{\mathrm{trap-assisted}}$, while the Auger-Meitner recombination, $\tau_{\mathrm{Auger-Meitner}}$, is recalculated with each iteration of $\Delta n(V)$. Then the effective bulk lifetime is

$$\tau_{\mathrm{bulk}}(V) = (1/\tau_{\mathrm{rad}}\,(V) + 1/\tau_{\mathrm{trap-assisted}} + 1/\tau_{\mathrm{Auger-Meitner}}(V))^{-1}. \quad (15)$$

The lifetime for surface recombination becomes indirectly incorporated later on through Equation 25. The bulk lifetime determines the diffusion length L through

$$L = \sqrt{\tau_{\mathrm{bulk}} D}, \quad (16)$$

with D the total diffusivity. The models for determining the diffusivity and lifetime values are detailed in Ref. [99]

The minority-carrier diffusion equation solves for the excess carrier concentration Δn as a function of depth z through

$$D\frac{d^2\Delta n(V,z)}{dz^2} - \frac{\Delta n(V,z)}{\tau_{\mathrm{bulk}}(V)} + g(z) = 0. \tag{17}$$

The generation rate is considered to be a superposition of generation from light incident at the front surface and light reflected at the rear surface:

$$g(z,E) = g_{-}(E)\,\mathrm{e}^{-\alpha_{\mathrm{lt}}(\mathrm{E})\,z} + g_{+}(E)\mathrm{e}^{\alpha_{\mathrm{lt}}(\mathrm{E})\,z}, \tag{18}$$

where $g_{-}(E)$ and $g_{+}(E)$ are the incident and reflected generation components, respectively. They are

$$g_{-}(E) = \frac{\alpha}{\alpha_t}\frac{(1-R_{\mathrm{f0}})\,\alpha_{\mathrm{lt}}(\mathrm{E})\,\phi_{\mathrm{AM}}(\mathrm{E})}{1-R_{\mathrm{b}}\,R_{\mathrm{f}}\,\mathrm{e}^{-2\alpha_{\mathrm{lt}}(\mathrm{E})\,\mathrm{W}}}, \tag{19}$$

$$g_{+}(E) = g_{-}(E)\,R_{\mathrm{b}}\mathrm{e}^{-2\alpha_{\mathrm{lt}}(\mathrm{E})\,W}, \tag{20}$$

where ϕ_{AM} is the spectral photon flux of the AM1.5G solar standard ($\mathrm{s^{-1}\ m^{-2}\ eV^{-1}}$) [104]. For the planar case, R_{f} is just equal to the external front reflectance $R_{f,\mathrm{ext}}$; for the textured case, $R_f = \frac{R_{\mathrm{f,ext}}(E)}{n_{\mathrm{r}}^2(E)} + 1 - \frac{1}{n_{\mathrm{r}}^2(E)}$, where n_{r} is the index of refraction.

The implicit boundary conditions for our generic absorber are identical to those used by Kowalczewski [100] for the base region:

$$D\frac{d\Delta n(V,z)}{dz}\Big|_{z\,=\,W} = -S\,\Delta n(V, z = W), \tag{21}$$

$$\Delta n(V, z = 0) = \frac{n_{\mathrm{i,eff}}^2}{n_{\mathrm{maj}}|_{z=0}}\left(\mathrm{e}^{\frac{qV}{kT}} - 1\right), \tag{22}$$

where S is the surface recombination velocity of the lower, nonideal contact. $n_{\mathrm{i,eff}}$ is the effective intrinsic carrier concentration as found through the bandgap narrowing models,

as explained in the main paper Ref. [99]. $n_{\mathrm{maj}}|_{z=0}$ is the majority carrier concentration at $z = 0$, as calculated from both Eq. 22 and the law of mass action.

The latter boundary condition shows the voltage's role in increasing injecting carriers from one side. Here the minority carrier contact is considered to be on the front, sunward side, but solutions for an absorber with the minority carrier contact at the rear can be readily derived from Kowalczewski's solution for the emitter region [100].

The particular solution to these conditions is

$$\Delta n(V,z) = \int_0^\infty \left[C_1 \cosh\left(\frac{z}{L}\right) + C_2 \sinh\left(\frac{z}{\mathrm{L}}\right) + \gamma(g_- \mathrm{e}^{-\alpha_{\mathrm{lt}}\mathrm{z}} + g_+ \mathrm{e}^{\alpha_{\mathrm{lt}}\mathrm{z}})\right] dE, \qquad (23)$$

where $\gamma = L^2/(D\left(1 - \alpha_{\mathrm{lt}}^2\, L^2\right)$. The expressions for the coefficients are

$$C_1(V,E) = \Delta n(V, z=0)\left(\frac{\phi_{\mathrm{AM}}\, A_{\mathrm{f}}}{\int_0^\infty \phi_{\mathrm{AM}}\, A_{\mathrm{f}}\, dE}\right) - \gamma\,(g_- + g_+), \qquad (24)$$

$$C_2(V,E) = \frac{\left[-C_1\left(\frac{D}{L}\sinh\frac{W}{L} + S\cosh\frac{W}{L}\right) - \gamma\left(g_-\mathrm{e}^{-\alpha_{\mathrm{lt}}W}(S-\alpha_{lt}D) + g_+\mathrm{e}^{\alpha_{\mathrm{lt}}W}(S+\alpha_{\mathrm{lt}}D)\right)\right]}{\left[\frac{D}{L}\cosh\frac{W}{L} + S\sinh\frac{W}{L}\right]}. \qquad (25)$$

Using $j = qD\,\frac{d\Delta n}{dz}|_{z=0}$, Kowalczewski gives the solution for the spectral current density as

$$j(V,E) = qD\left(\frac{\mathrm{C_2(V,E)}}{L(V)} + \gamma(V,E)\left(-\alpha_{\mathrm{lt}}(\mathrm{E})\, g_-(\mathrm{E}) + \alpha_{\mathrm{lt}}(\mathrm{E})\, g_+(\mathrm{E})\right)\right). \qquad (26)$$

The total current density $J(V)$ is then found by integrating $j(V,E)$ with respect to photon energy. In conventional modeling, the current density J is simply taken as the photogeneration current density from incident light minus the recombination current density.

The external quantum efficiency is found from

$$Q(E) = \frac{\Delta j(E)}{q * \Delta\phi(E)}, \tag{27}$$

where Δj is the change in the spectral current density incurred by an infinitesimal change in incident spectral flux $\Delta\phi$ at a particular energy. The QFLS is found through the law of mass action to be

$$\Delta\mu(z) = kT \ln\left(\frac{n(z)\, p(z)}{n_{i,eff}^2}\right), \tag{28}$$

n and p are carrier concentrations found from the sum of Equation 23 and the equilibrium concentration of the majority carrier.

The carrier concentrations are used to recalculate the radiative and nonradiative recombination currents, the bulk lifetime, the photon recycling diffusivity, and the diffusion length. For materials in high-level injection, convergence can be sped up by setting values for the next iteration as the average of the previous iteration's input and output values. Looped iterations repeat until the diffusion length converges to within 0.01%, corresponding to a 0.001% precision in efficiency.

Computational methods for finding V_{mp} and V_{oc} can then be readily applied.

C. Material Parameters

Intrinsic carrier concentrations and Auger coefficients used are given in Table 1.

Table 1
MATERIAL PARAMETERS FOR DEVICE MODELING

	CIS [105,108]	Si [106]	GaAs [107,109]	CdTe [105,110]
Bandgap (eV)	1.016	1.125	1.423	1.514
n_i (1/cm^3)	8.4×10^{9}	8.28×10^{9}	1.79×10^{6}	8.19×10^{5}
C (cm^6/s)	6×10^{-30}	1.7×10^{-30}	7×10^{-30}	9×10^{-32}

The silicon Auger recombination coefficient is given here as a reference as silicon's Auger current is calculated with the Richter parametrization.

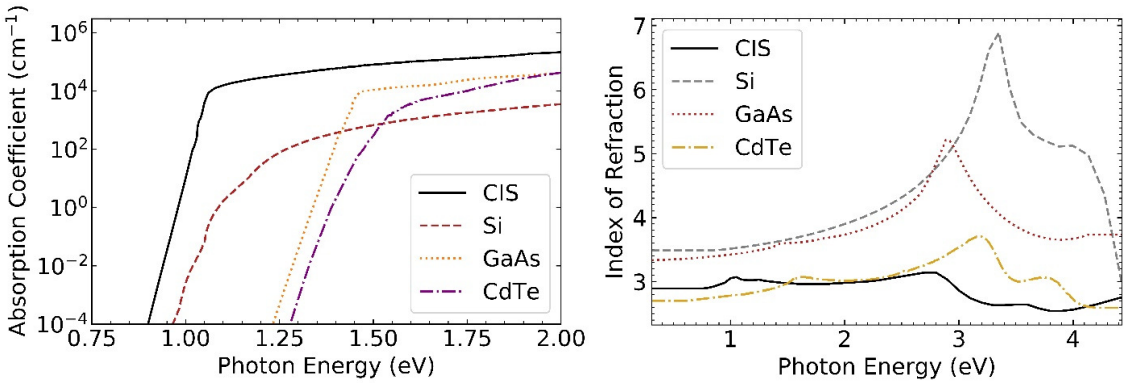

Fig. 8. Spectral absorption coefficient (left) and index of refraction (right) used in the absorptance calculations.

Absorption coefficients [105], [106], [107], [105] and indices of refractions [108], [106], [109], [110] are plotted in Fig. 8.

II. Methods for Bulk and Surface Recombination Characterization

Recombination in III-V materials can be characterized by time-resolved photoluminescence (TRPL) measurements of the effective minority-carrier lifetime. TRPL is done on double heterostructures of a uniform doping type so that minority carriers are contained within the passivation layer. The containment of a double heterostructure enables the correlation of a reduction in the photoluminescence signal over time with the carrier recombination rate.

The general equation to separate bulk and surface recombination uses the relationship between the total effective lifetime τ_{eff} and absorber thickness W:

$$\frac{1}{\tau_{eff}} = S\frac{2}{W} + \frac{1}{\tau_{bulk}}, \qquad (29)$$

where τ_{bulk} is the bulk lifetime and S is SRV [111]. The standard procedure to extract τ_{bulk} and S is to graph $1/\tau_{eff}$ and $2/W$, apply a linear fit, and then identify $\frac{1}{\tau_{bulk}}$ and S as the fit's y-intercept and slope, respectively.

In Section 6.I, TRPL is taken to determine the carrier lifetime for intrinsic GaP/GaNP/GaP/Si double heterostructures. The TRPL system chops 540-nm emission from a Fianium laser into a 100-fs pulse with a rep rate of 0.5MHz. The laser power used was on the order of 10 mW with a beam diameter of 1 mm. The TRPL signal is thus much lower than available with a continuous-wave PL signal, so for this material, the TRPL signal falls below the background noise at around 170 K.

For characterization of the GaInP/GaAs/GaInP double heterostructures of Section 6.II, the TRPL measurements use a Carbide solid-state laser with an Orpheus optical parametric amplifier from Light Conversion Inc. This setup used a 0.627 MHz repetition rate, a 217-fs pulse duration, a 532 nm excitation wavelength, and a 3 μW laser power with a 2.1 μm beam diameter. This laser was also used for the samples of Section 6.III but with a focused beam diameter and a varied beam intensity.

For TPRL characterization of the nanostructured samples of Section 6.III, the laser beam must be focused on small areas. Small areas are required because the electron beam lithography (EBL) processing is only done over small areas (as the EBL tool takes several days to process just a 1 mm by 1 mm area). Hence, photoluminescence excitation must be restricted to the small nanostructured area. The array widths range between 100 μm and 800 μm, with typical widths of 250 μm (corresponding to hundreds of nanostructures in each of the X- and Y- directions). To confine incident light to such areas, a lens is used to collimate the laser beam from 2100 μm to a 39 μm beam diameter.

Additionally, a 1-mm iris aperture is placed above the lens to limit stray light. While the incident beam is oriented normal to the sample, the sample's emitted photoluminescence is collected with a fiber optic angled at 45-60° to the normal. A stepper motor is used to move the sample stage and position the measurement area under the laser beam, while a camera with a maximum of 180x magnification was used to identify alignment of the laser beam and the EBL array. With this setup, less than 1% of incident laser light strays outside of the nanostructure array, as determined for an array of 250 μm. As the nanostructured array typically yields equal or higher photoluminescence than the surrounding area, the impact of light hitting outside of the nanostructured area is considered to be negligible.

III. Methods for PPC Simulation

The photonic power converter (PPC) simulations involve in-house device modeling along with electromagnetic modeling simulated in the finite-difference time-domain (FDTD) Ansys Lumerical program.

A. PPC Device Modeling

Device modeling is performed to determine the optimal incident wavelength and the benefits of light trapping for PPCs. The device efficiency is determined from an analytic solution to the minority-carrier diffusion equation presented in Section 3.I.B. The change here is that the PPC study models GaAs with varying levels of light trapping by modifying the carrier generation rate. In both studies, the generation rate is found from a superposition of two traveling waves. The amplitude of the front-incident wave is taken as

$$A_{-} = \frac{\alpha}{\alpha_t} \frac{\left(1+\frac{X}{50}\right)\alpha\,\phi}{1-\left(1-\frac{4}{X}\right)e^{-X\alpha W}}, \qquad (1)$$

where X is the path-length enhancement due to light trapping, α is the band-to-band absorption coefficient, α_t is the sum of α and free-carrier absorption (FCA), and W is the absorber thickness, and ϕ is the photon flux density of incident light.

The PPC structure in consideration is an n-GaAs absorber with generalized carrier selective contacts. The generalized contacts enable modeling to apply to both homojunctions and heterojunctions, and it focuses results on the effect of light trapping on the absorber. The contact layers are characterized with a rear surface recombination velocity of 3600 cm/s, and the 40 nm absorber has a doping of $2 \cdot 10^{17}$ cm^{-3} with a bulk lifetime of 10 ns, which are the material parameters characteristic of material grown with the molecular beam epitaxy tool at Arizona State University. At this bulk lifetime, Auger and radiative recombination were determined to be negligible compared to trap-assisted recombination.

B. FDTD Optical Modeling

Modeling of the absorptance gains was primarily done with the commercial software Lumerical. Lumerical runs on a finite-difference-time-domain (FDTD) method. The method discretizes the electromagnetic field into a numerical grid to solve Maxwell's equations [112]. As this is then tracked in time for each grid point, FDTD solvers become very computationally expensive unless the volume can be kept small. Consequentially, the method becomes feasible only for situations where symmetry arguments can be used.

The default settings used for the simulations were the following. The analysis wavelength was 866 nm. The wave source was a Bloch plane wave. The simulation temperature was room temperature, i.e., 298.1 K.

A simulation time of 270 fs was used as the default, but an early shutoff setting of 0.002 was used to stop the computation when the power left in the simulation region drops below 0.2% of the injected power. The boundary conditions used were anti-symmetric on the x boundaries, symmetric on the y boundaries, “metal” on the negative z boundaries, and perfectly matched layer (PML) on the positive z-boundaries; where the z-axis is oriented from the substrate to the point source, and the electric filed polarization oriented in the x-axis direction. The mesh size was set at 3 on a scale of 1-8, and the “conformal variant 1” was applied on the mesh. The early shutoff, boundary conditions, simulation time, and mesh size were carefully selected to give faster simulations while keeping simulation accuracy to the order of 1%.

The simulated material stack was a nanostructure array on top (or bottom) of a stack of GaInP/GaAs/GaInP/SiO_2/Ag. The top GaInP layer fixed at 250 nm and the bottom Ag layer fixed at 250 nm. At times, the nanostructures themselves were covered with a variable-thickness layer of SiO_2, which was varied from 0 to 200 nm. The nanocone diameter was optimized from 0.01 to 1.5 μm while the height was varied from 0 to 1.5 μm. The ratio of the center-to-center period to the diameter was varied from 1 to 1.5. The GaAs thickness was varied from 50 to 120 nm. The SiO_2 thickness was varied from 0 to 400 nm. The cone sidewall angle was varied from 0 to 110°, with respect to the horizontal.

The absorption of the GaAs layer was determined using the "pabs_adv" monitor published by Lumerical in 2012. This solver finds the absorption in a region as $-\frac{1}{2}\omega|E|^2\,\epsilon_i$, where ω is the frequency, E the electric field, and ϵ_i is the imaginary part of the dielectric constant. This "advanced" of determining absorption differs from Lumerical's "simple" method in that it finds the absorption in each the three Cartesian coordinates before integrating over the volume to find the total absorption.

As for material constants, the Ag, Al, and Au optical constants used were from the CRC handbook of Chemistry and Physics, with original sources at [113,114,115]. The AlGaAs ($Al_{0.3}Ga_{0.7}As$) values were refractive index $n = 3.37209$ and extinction coefficient $k = 0$, values which were taken in the file given by Lumerical at [116]. The front anti-reflection coefficient's extinction coefficient was taken as 1.8026, which was originally calculated as an ideal value, but also closely matches the value for Al_2O_3. The rear dielectric value was set as 1.3745, representative of MgF_2 [117]. The GaAs values used were that of Palik [118], namely $n = 3.666$ at 826.6 nm and $n = 3.614$ at 885.6 nm. The default Lumerical material library does not include literature data between those wavelengths, which would lead to a coarse estimation of near-bandgap absorption. Fortunately, Palik et al. gives k values (without n values) in that range: 0.0557 at 864 nm and 0.0572 at 867 nm. The Lumerical program then applies a linear fit between these literature values to find the GaAs values at 866 nm: $n = 3.62991$ and $k = 0.0567009$.

The n and k values for GaInP were directly measured at Arizona State University by my colleague Sean Babcock. The epitaxial material was grown by Veeco Instruments Inc. through metal-organic chemical vapor deposition (MOCVD) upon a GaAs substrate. The ellipsometry data was analyzed by J.A. Woollam. The parameter extraction was done

in the Complete Ease software, finding an appropriate fit with a GaAs substrate, a GaInP layer, and a 1.78 nm GaP oxide. The extracted values of the index of refraction n and extinction coefficient k around this study's principal simulation wavelength, 866 nm, are n=3.269 and k=0.000167 at 866.64 nm and n=3.270 and k=0.000182 at 865.08 nm. At lower wavelengths, the k doesn't go above 0.001 until 822 nm and above 0.01 until 678 nm. Such low extinction coefficients enable high photonic power converter (PPC) efficiencies to be found at greater GaInP thicknesses. Appendix A gives the measured values of the index of refraction n and extinction coefficient k for GaInP lattice matched to GaAs.

IV. NANOTEXTURING METHODS

The samples for the nanotexturing process were provided by VEECO Inc. They were made by Metal-Organic Chemical Vapor Deposition (MOCVD). The substrates used were p-GaAs substrate, 5° miscut toward <110, with $(0.5\text{-}5.0)\times10^{19}$ cm^{-3} Zn doping. Zn was also the dopant used for the epitaxial layers.

For the texturing process, multiple fabrication plans have been explored for nanocones on the front of the material. These include 1) nanosphere lithography 2) nanoimprint lithography and 3) optical lithography. Nanosphere lithography is the most readily available but gives low spatial uniformity [119] – and modeling results showed the spatial uniformity in structure-to-structure spacing to be critical for the project. Nanoimprint lithography gives better geometric control but takes a much longer time to set up. Optical lithography may be the most direct route, but the available tools have too

coarse of resolution (700 nm critical dimension) for nanotexturing. Thus, e-beam lithography (EBL) followed by plasma etching has been chosen for the development.

The target baseline EBL geometry is an etch depth of 150 nm in a 150 nm gap between nanocones of 600 nm diameters in a hexagonal array, which translates to a 750 nm center-to-center spacing. Here, the critical dimension of fabrication is the 150 nm gap width. The electron-beam resist used was the positive resist ZEP520A. The electron beam lithography (EBL) conditions used were:

The electron beam lithography (EBL) conditions used were:

- Resist spun at 2500 repetitions per minute
- Resist soft bake for 3 min at 180ºC
- EBL dose exposition of 100 $\mu C/cm^2$
- Resist development for 90 s in n-amyl-acetate
- Rinse for 60 s in isopropyl alcohol

The resist nanostructures are then transferred into the III-V material through plasma etching. The baseline plasma etching conditions are:

- 10 sccm Ar flow
- 10 sccm Cl_2 flow
- 0.3 Pa chamber pressure
- 140 W inductively coupled plasma (ICP) power
- 70 W platen bias power
- 65 seconds etch time
- 20°C substrate temperature

Note: A newer round of etching used an ICP power of 65 W and a bias power of 25 W, which has been observed to give a better ability to reproducibly etch thinner layers.

The etch chemistry used for GaInP is Cl-based. While fluorine is commonly used to etch silicon, F does not have a volatile enough reaction with indium to etch GaInP. Cl will have a higher volatility, but not high enough to cause significant chemical etching.

For this Cl_2/H_2 dry etching of GaInP, it is expected that the platen bias power needs to be increased to create physical sputtering through desorption of the surface [120,121,122]. While chamber pressure can be used to change the etch rates in Si F-based etching, the volatility of In in GaInP is so low that the pressure does not strongly affect the etch rate for this process. As the etch is not limited by the chemical diffusion of chemical but by the ability of the ions to cause InCl subproduct desorption from the ion bombardment. As platen bias power drives desorption in this process, it has a dominant influence on the etch rate and geometric shape of the nanostructures. If the bias power is reduced below around 20 W, then the etch rate is dramatically reduced. 25 W bias power has recently been identified as an appropriate value that gives an etch rate in GaInP around 200 nm per minute.

At bias powers at 20 W or below, the etch rate starts very low but can dramatically increase during the etch if the top-surface temperature goes above the InCl boiling point, which is 150°C at vacuum pressures [123, 124]. The back of the substrate should be near the 20°C platen temperature, but the top surface of the sample is likely to be at a much higher temperature due to plasma bombardment. High temperatures should be avoided because the ZEP520A resist undergoes reflow at around 85°C.

With the high bias power conditions, the approximately 500 nm of ZEP500a was generally completely removed during the one minute of etching, meaning that resist removal was not needed. At the lower plasma etch bias power, some EBL resist remained after etching. In that case, the resist is removed by a 5-minute rinse in MICROPOSIT™ Remover 1165, followed by rinses in acetone and isopropyl alcohol.

The selectivity of the etch for GaInP over the ZEP500a was found to be around 0.4. Originally, PMMA was used as the EBL resist, but the selectivity was close to 0, which motivated the choice of ZEP500a as a positive resist more resistant to plasma etching.

V. METHOD FOR OUTDOORS THERMAL EXPERIMENT

The second work examines the interaction of texturing, sub-bandgap reflection, and temperature. This research requires three distinct methodologies: A) Experimental design of the temperature measurements B) Modeling details for calculated temperatures C) Calculations for enhanced sub-bandgap reflection.

A. *Experimental Design of the Temperature Measurements*

The outdoors test facility is installed at Merced, CA, 37.3746° N, -120.5788° W, and 58 m elevation. Six solar panels were mounted flush with a black-anodized aluminum sheet, as depicted in Fig. 9. These modules include two single-crystalline Si modules (SC-Si), two multi-crystalline Si modules (MC-Si), and two thin-film GaAs modules. A variety of Si modules were chosen for a range of efficiencies and sub-bandgap reflectances.

The solar modules are mounted in an experimental structure that can be changed between two different thermal configurations: open-rack and insulated. This structure is presented in Fig. 9. In the insulated configuration, the rear is covered with 15 cm of fiberglass batt, which is held up by plywood. In the open-rack configuration, the rear backsheet is exposed to the air and ground below. All modules were connected to the structure using insulating material to isolate them from the frame and racking. The mounting structure is 2.4 m^2 and mounted 1 m above ground. The surface has a 5° tilt due south to repel rainwater.

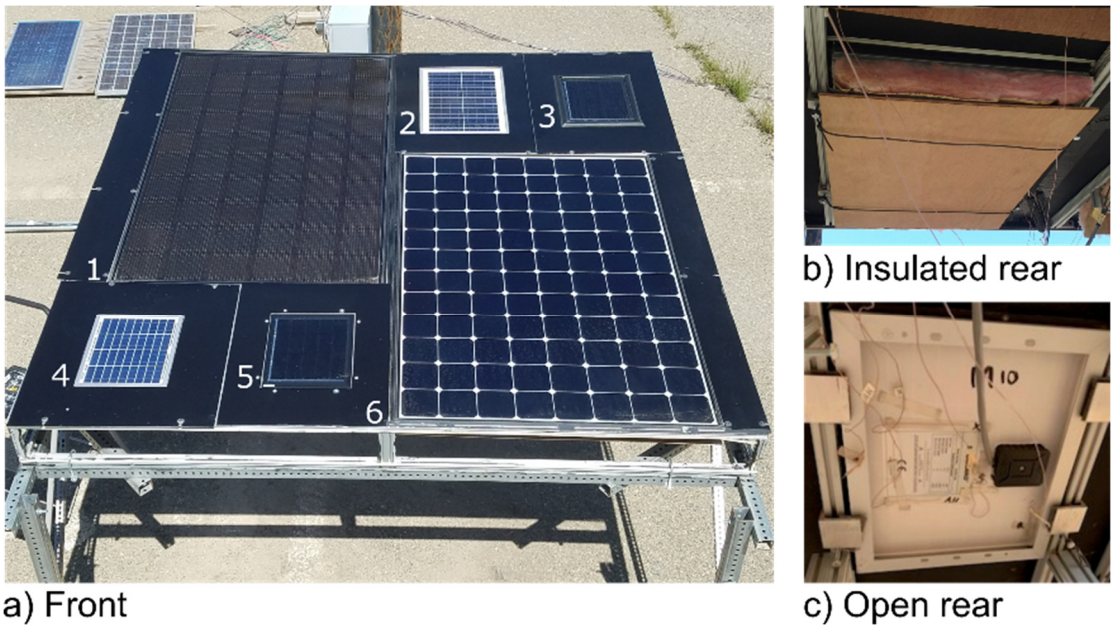

Fig. 9. a) Image of the experimental rack with two single-crystalline Si cells (1, 6), two multi-crystalline Si cells (2, 4), and two GaAs cells (3, 5). At different test times, the modules' rear are either b) insulated with fiberglass batt or c) open from backsheet to ground.

Measurements were sampled every 3 minutes and logged with a Daystar MT5 multi-tracer. Between each current-voltage measurement, modules were biased at their maximum power point. Temperatures were measured with T-type thermocouples attached to the center of backsheets via tape of an appropriate expansion coefficient. An

in-plane thermopile pyranometer records irradiance, while a cup anemometer records wind speed and direction. Relative humidity was recorded with an Omega HX71-V2 sensor, finding an average of 35% humidity.

B. *Analytical Thermal Modeling*

The module temperature is calculated through the thermal balance equation [125]:

$$A_{\mathrm{t}}G = h_{cf}(T_{\mathrm{mod}} - T_{\mathrm{amb}}) + \varepsilon_{\mathrm{g}}\left(\sigma T_{\mathrm{mod}}^4 - R_{\mathrm{sky}}\right) + \delta_{\mathrm{cf}}\,\varepsilon_{\mathrm{b}}\sigma\left(T_{\mathrm{mod}}^4 - T_{\mathrm{gnd}}^4\right) + \eta G, \qquad (30)$$

where A_{t} is the module's total full-spectrum absorptance (inclusive of parasitic absorption in contact and encapsulant layers), G is the solar irradiance, $\mathrm{h_{cf}}$ is the convection coefficient (particular to each configuration), $\mathrm{T_{mod}}$ is the module temperature in K, $\mathrm{T_{amb}}$ is the ambient temperature, $\varepsilon_{\mathrm{g}} = 0.84$ is the emissivity of glass while $\varepsilon_{\mathrm{b}} = 0.893$ is the backsheet's emissivity [125], σ is the Stefan–Boltzmann constant, $\mathrm{R_{sky}}$ is the downwelling thermal radiation from the sky, $\mathrm{T_{gnd}}$ is the ground temperature, and η is the photovoltaic efficiency calculated with respect to the active area. δ_{cf} is 0 in the insulated configuration and is 1 in the open-rack configuration, as rear radiation only occurs in the open-rack configuration. G, $\mathrm{T_{mod}}$, $\mathrm{T_{amb}}$, $\mathrm{T_{gnd}}$, and the maximum power were remeasured every three minutes. $\mathrm{R_{sky}}$ is found by inputting humidity and ambient temperature into (4) in [126]. For experimental data where power is measured, the efficiency η is calculated from power and area.

To extrapolate the model to different cities, inputs, including irradiance, ambient temperature, and wind speed, are taken from typical meteorological year (TMY) data. Variation in efficiency with temperature is incorporated with the substitution $\eta = \eta_{\mathrm{STC}}(1 + \gamma[\mathrm{T_{mod}} - 25])$ into Eq. 30, which is then solved numerically to acquire $\mathrm{T_{mod}}$.

The temperature coefficients γ are taken from previous measurements [127]. The STC efficiency η_{STC} was extracted using a linear fit to extrapolate to 25°C while simultaneously filtering the data for irradiances near 1000 W/m^2 [127]. The efficiency relative to STC efficiency, defined by $\eta_{rel} = \eta/\eta_{STC}$, is considered to isolate the effects of temperature on performance. The performance ratio is then an irradiance-weighted average of the relative efficiency over a year. The module-level performance ratio in this report considers the effects of temperature but not of soiling, shadowing, the inverter, or other system-level issues [128].

The value of A_t, the full absorptance of all layers in the active area, is found once for each module from

$$A_t = \frac{\int (1-R(E))G(E)dE}{\int G(E)dE}, \tag{31}$$

where R is the total reflectance from the module. The reflectance curves for encapsulated modules are given in Fig. 10, showing high reflection for energies below the bandgaps (1.12 eV for Si, 1.42 eV for GaAs). The GaAs curves show a substantial improvement over modules used in Silverman's 2012 report [85]. Nevertheless, parasitic absorption in the encapsulant reduces sub-bandgap reflection at specific energies, including 0.72 eV. The GaAs reflectance curves were measured directly with an Agilent Cary spectrophotometer by Alta Devices Inc. The Si curves are taken from the experimental encapsulated results of [129]. For the high-efficiency, single-crystalline modules, we use the passivated emitter and rear contact (PERC) reflectance with line contacts. For the multi-crystalline modules, we use the aluminum back-surface field (Al-BSF) reflectance. The fitted A values are given by Table 2.

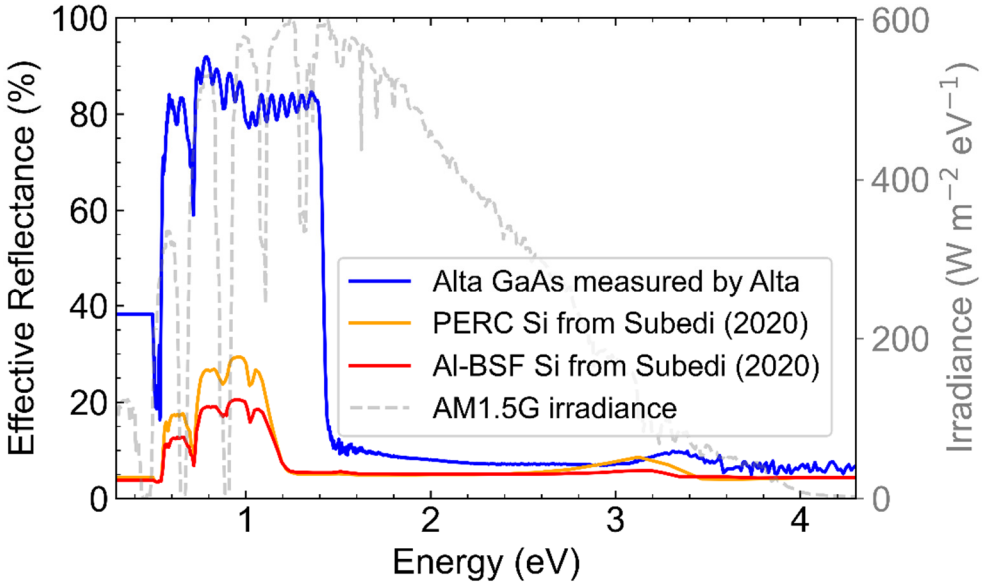

Fig. 10. Measured reflectance curves of the encapsulated cells. The GaAs modules reflect more sub-bandgap light due to a higher bandgap and a higher sub-bandgap reflectance.

Table 2
FULL-SPECTRUM ABSORPTANCE A_T

GaAs	MC-Si	SC-Si
0.721	0.923	0.909

The final model parameter, the convection coefficient for the configuration h_{cf}, is found by fitting the thermal balance equation to the whole set of measurements, including T_{mod}. Similar to [86], the fitting is done upon the insulated configuration and then extended to the open rack configuration through the piecewise function:

$$h_{cf} = [(h_1 * v + h_2)^3 + h_3^3]^{1/3} + \delta_{cf}\, h_3, \tag{32}$$

where v is the wind speed, and δ_{cf} is 0 for insulated and 1 for the open-rack configuration. Allowing for different convection coefficients (h_1, h_2, and h_3) for each module reduces root-means-square (RMS) error by 30% between model and measurement. The fitted values are given in Table 3. The resultant h values are smallest for the largest-area modules and are biggest for the modules positioned at the rack's

corners, which can be expected as air is colder at the rack's edge than its center. The fitted forced-convection values $h_1 * v + h_2$ align closely with models of [130,131,132]. The natural convection coefficient h_3 for an object can be calculated from its characteristic dimension [133], but here the effective characteristic dimensions are uncertain because of the presence of the large mounting rack. The fitted h_3 values lie between the number expected based on the geometry of the module alone and of that from the geometry of the entire rack.

Table 3
FITTED CONVECTION COEFFICIENTS

	GaAs1	GaAs2	MC-Si1	MC-Si2	SC-Si1	SC-Si2
h_1	3.7	3.2	3.6	4.1	1.4	0.8
h_2	0.97	0	0.14	2.2	6.3	6.4
h_3	9.2	8	9.1	12	4.6	4.7

The units are W m^{-2} K^{-1}.

C. Calculations of Sub-Bandgap Reflection

Sub-bandgap reflection can significantly reduce a module's heat input. However, the effective sub-bandgap reflectance for commercial Si modules has been measured as 15-22% - values far below optimal [129].

The sub-bandgap reflectance R_{sub} can be derived through ray tracing [134] or conservation methods [135]. For planar modules,

$$R_{sub}(E) = R_{ext} + \frac{(1-R_{ext})R_b\, T_{pb}^2\, T_{pf}^2 (1-R_{int})}{1-R_b\, T_{pb}^2\, T_{pf}^2\, R_{int}}, \quad (33)$$

where R_{ext} is the external front reflectance, R_{int} is the internal front reflectance, and R_b is the back-surface reflectance. T_{pb} and T_{pf} are the transmission of light through the bulk

and front layers, respectively. Transmission is calculated as the product of $e^{-W\alpha}$ for each layer, where W is the layer thickness and α the absorption coefficient.

Sub-bandgap reflection depends strongly on parasitic absorption (PA) [135], [136]. The tabulated absorption coefficients for PA in encapsulation materials are taken from [137]. The encapsulant material, typically ethylene vinyl acetate (EVA), absorbs strongly at wavelengths above 1700 nm. The encapsulant is responsible for reflectance minima at 0.72, 0.88, 1.02, and energies below 0.56 eV. Experimental reports have shown EVA encapsulation to reduce sub-bandgap reflection of point-contact PERC cells by 34% [129]. The encapsulation is taken as 0.4 mm thick and the glass as 3.2 mm. PA in Si layers is modeled with free carrier absorption (FCA) [138]. For a p-type 180 μm base, the hole concentration is taken as $7.6 \cdot 10^{15}$ cm^{-3}, characteristic of PERC [139]. For an n-type 0.7 μm emitter, the electron concentration is modeled with one of two Gaussian doping profiles. A moderate-doping profile with a maximum of $2 \cdot 10^{20}$ cm^{-3} and a total dose of 10^{15} cm^{-2} represents a typical commercial profile, which is used to compare calculations to experimental values [140]. Alternatively, a low-doping profile with a maximum of $9 \cdot 10^{18}$ cm^{-3} and a total dose of 10^{14} cm^{-2} is later used to represent the level that can be achieved through selective emitters [140].

For textured modules, the thicknesses W are scaled by two due to the longer path when light scatters into angles (at an average of 60°) [141]. Light refraction will also cause some photons (around 10% per pass) to transmit from Si into encapsulation materials before reflecting at the glass/air interface. So, for textured modules,

$$R_{sub}(E) = R_{ext} + \frac{(1-R_{ext})R_b\, T_{pb}^2 T_{pf}^2 (1-R_{int})}{1-R_b\, T_{pb}^2 \left(R_{i1}+(1-R_{i1})R_{i2}T_{pf}^2\right)}, \quad (34)$$

where $R_{i1} = 1 - n_2^2/n_1^2$, $R_{i2} = 1 - 1/n_2^2$, $n_1 = 3.5$ is the index of refraction in Si, and n_2 = 1.5 the index in the encapsulant/glass.

CHAPTER 4

BENEFITS OF LIGHT TRAPPING AND PHOTON RECYCLING

This chapter details my results from two papers. The first section is recombination from my paper, Ref. [98], published in the proceedings of the SPIE. The second section is efficiency results made with the device modeling I developed in "Feedback Between Radiation and Transport in PV Material," which is published in the journal Prog. Photovoltaics [99].

I. RECOMBINATION ANALYSIS

The effects of Lambertian light distribution and back reflectance on GaAs radiative recombination is examined in Fig. 11. The radiative recombination emitted out the front is higher for Lambertian cells than planar cells, which is due to increased absorptance/emittance. Unexpectedly, the rear emission reduces with Lambertian light. This reduction is due to redistribution of the internal radiation: photons outside of the escape cone in the planar case remain out of the escape cone leading to light trapping and full absorptance/emittance, whereas photons outside of the escape cone in the Lambertian case get diffracted into the escape cone leading to reduced absorptance/emittance. The net radiative recombination for GaAs, nonetheless, is larger in a Lambertian cell. At a given voltage, most absorbers show higher recombination currents for Lambertian cells. For GaAs and CdTe, this increase in recombination results in a V_{oc} loss on the order of 10 mV. For CIS, however, net radiative recombination can be reduced in a Lambertian light distribution. The CIS cell at 80% reflectance, for instance, experiences less net radiative recombination under Lambertian conditions for $W > 300$ μm. Texturing does not necessarily increase recombination. For a CIS cell with $W = 0.1$ μm at $R = 0$, the

reduction in rear radiative recombination combined with a J_{sc} gain results in a V_{oc} gain for the Lambertian configuration.

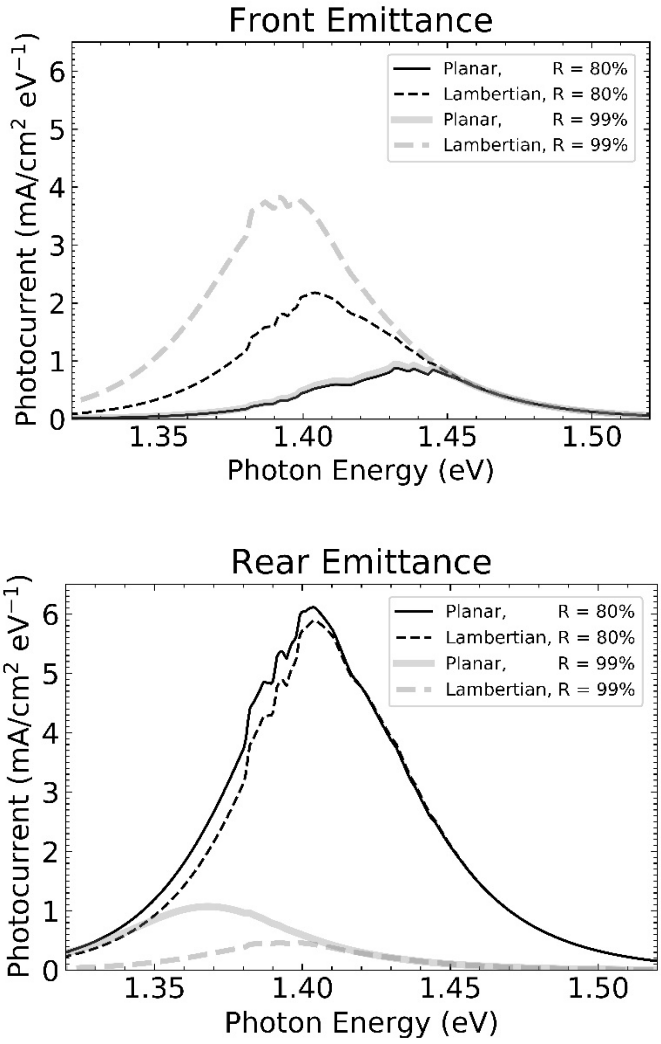

Fig. 11. Spectral photocurrent for a 3-μm GaAs absorber layer at 1 V. Front radiative recombination is increased in the Lambertian case, but rear radiative recombination is

It is interesting to note an apparent contradiction that higher radiative emission [142] and lower radiative emission [143,144] can both be associated with higher photovoltaic efficiencies. On one hand, higher voltages will lead to higher radiative recombination rates through stimulated emission, but on the other hand, higher radiative recombination will lead to lower current densities. The contradiction is resolved by

noting that recombination should be reduced when the change does not lead to a decrease in photogeneration. So, in the directions and energies where incident light is negligible, a reduction in radiative emission can lead to overall efficiency gains [143,144]. For examples, monofacial cells receive an efficiency gain if a reflector is placed on the back of the cell, because monofacial cells will not receive photogeneration from light in that direction anyways – thus a decrease in net radiative recombination is achieved without a loss in photogeneration [145]. As *non*-radiative recombination is not generally linked to photogeneration, reduction in non-radiative recombination currents such as Auger or trap-assisted recombination will generally lead to efficiency gains.

Fig. 12 presents statistics on Auger and radiative recombination currents under various rear reflectances and absorber thicknesses at V_{mp}. The direct bandgap materials (CIS, GaAs, CdTe) experience mostly radiative current, with higher bandgap materials experiencing lower recombination currents. The GaAs and CdTe Auger recombination currents are a negligible component of the total recombination current, but the low-bandgap material CIS experiences significant Auger recombination in a few cases due to a higher n_i - see Eq. 11. As a thicker low-bandgap material, silicon experiences significant Auger recombination current with some radiative current.

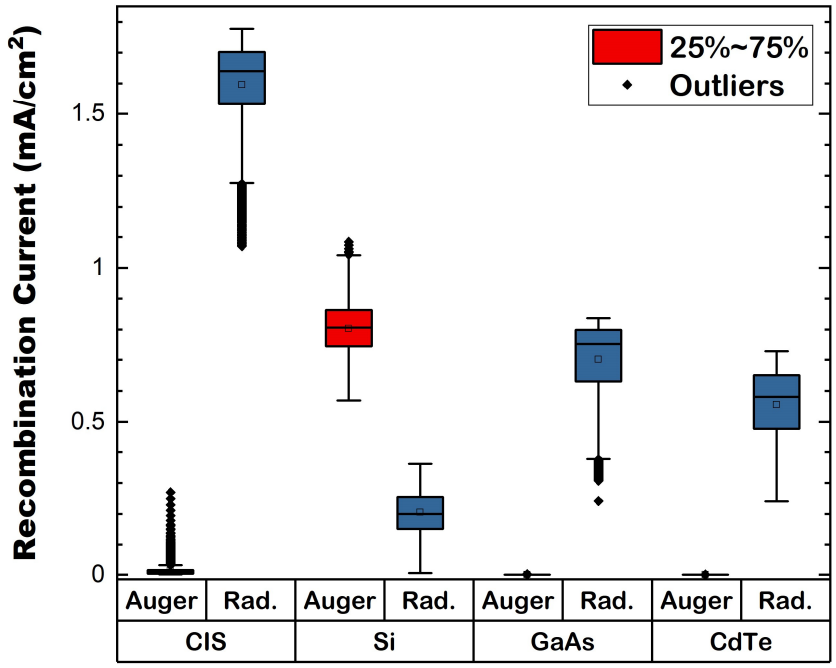

Fig. 12. Statistical depiction of Auger and radiative recombination currents at the voltage of maximum power V_{mp} for various rear-mirror reflectances and Lambertian and planar structures. The absorber thickness is ranged between 0.1 and 10 µm for direct bandgap materials and between 10 and 1000 µm for silicon.

II. Benefits of Light Trapping on Efficiency

Note that while the previous section are earlier results made from just the detailed balance model, presented in Section 3.I.A and Ref. [98], this section uses the theory that merges detailed balance with the diffusion model, presented in Section 3.I.B and Ref. [99]. As such, carriers need to be within a diffusion length away from the contacts in order to be efficiently collected, which makes the accounting of absorber thickness in simulations more realistic.

The ability of the unified model to simulate both detailed balance effects (photon recycling) and diffusion effects is examined in Figure 13. The modeled material is a 3 µm p-GaAs absorber with doping at $2 \cdot 10^{16}$ cm^{-3}, a rear reflection of 100%, and zero

surface recombination. The impact of the diffusion model is determined by comparing it to calculations made without the diffusion model, where the total current density is taken simply as photogeneration minus recombination. With successive drops in the trap-assisted lifetime, the efficiency curves of both models initially flatten and fall at the same pace due to the falling V_{oc}. At lower lifetimes, around 10 ns, the diffusion model's efficiency values begin dropping faster as the material becomes diffusion limited and the collection efficiency and J_{sc} begins to collapse.

For high lifetimes, the impact of photon recycling is seen through a substantial increase in V_{oc} with increasing rear reflectance. For an infinite trap-recombination lifetime, V_{OC} increases by 70 mV with increasing rear reflection – compared to an increase under 1 mV if photon recycling is not modeled. These results were found using the GaAs absorption coefficient of Miller to allow for a comparison with that seminal paper on photon recycling [34]. The agreement with those results shows the present diffusion model to be consistent with the phenomenon of photon recycling.

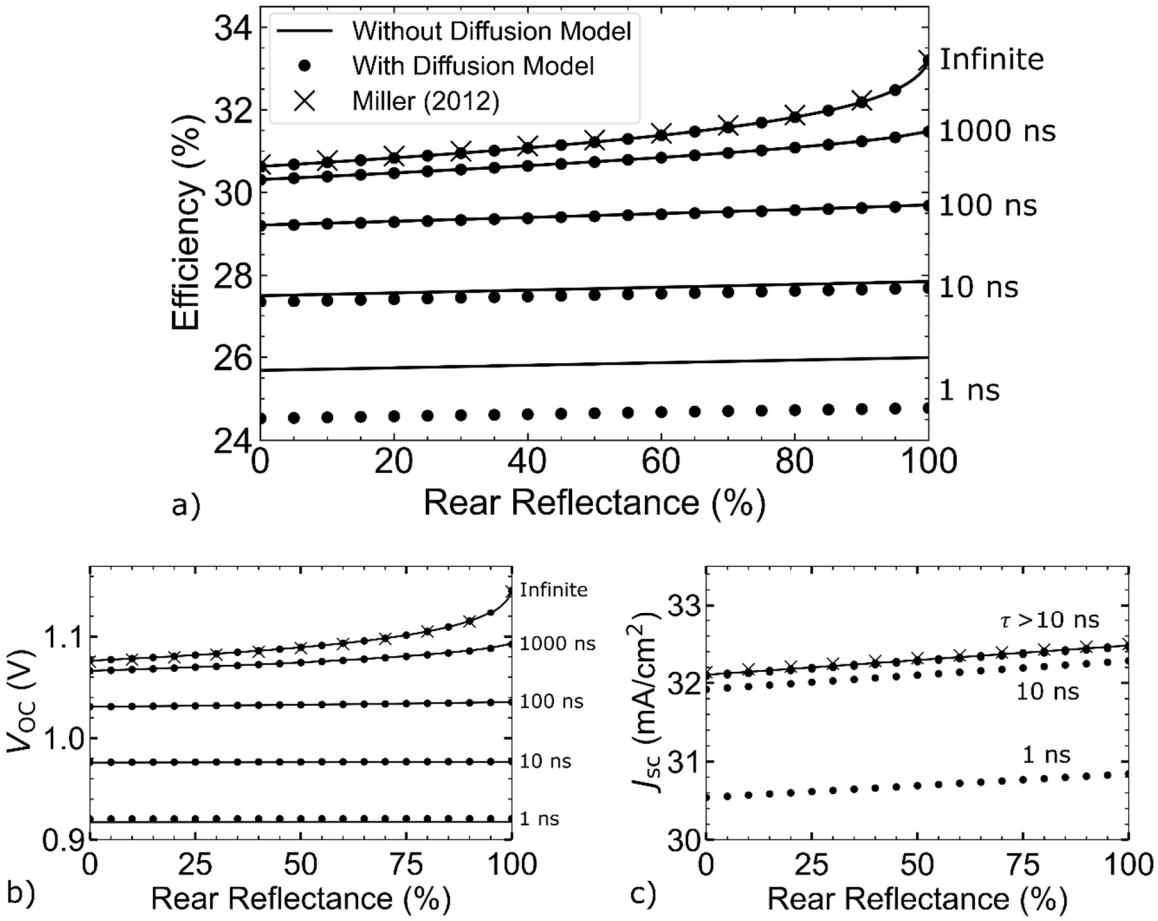

Fig. 13. Comparison of results with and without the diffusion model for GaAs for a range of trap-assisted recombination lifetimes.

Next, the optimal thickness and efficiency of a planar p-GaAs absorber of 10^{17} cm^{-3} doping is examined in Fig. 14. In this plot, it is seen that the material with the low lifetime achieves maximal efficiencies around 1-5 μm, but the high-lifetime material (without trap-assisted recombination), can also achieve high efficiencies at much larger thicknesses because the diffusion length can be long. For the high-lifetime materials, any losses in voltage for thicker layers are approximately canceled out by gains in current.

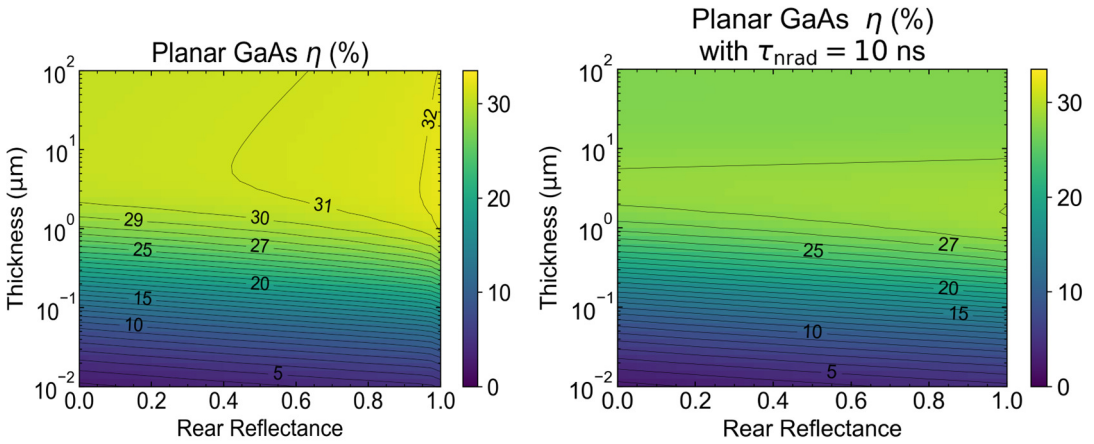

Fig. 14. Solar cell efficiency for a high lifetime (left) and a low-lifetime (right) p-GaAs absorber with 10^{17} cm^{-3} doping.

The plots above also show greater gains due to increases in rear reflectance for the high-lifetime than the low-lifetime material. For the low-lifetime material, increases in the rear reflectance only yield absorption gains; photon recycling does not contribute to the low-lifetime material as it is nonradiative limited. But, for the high-lifetime material increasing rear reflectance leads to a lower net recombination rate due to photon recycling in addition to the absorption gains that occur for thinner GaAs materials.

Next, the impact of light trapping on multiple materials is examined in Figure 15. The materials were all modeled as doped p-type, with 10^{14} cm^{-3} for CdTe, 10^{16} cm^{-3} for Si, 10^{17} cm^{-3} for GaAs and CIGS. Here, only intrinsic recombination is considered, i.e., radiative and Auger recombination, so these are results for ideal materials.

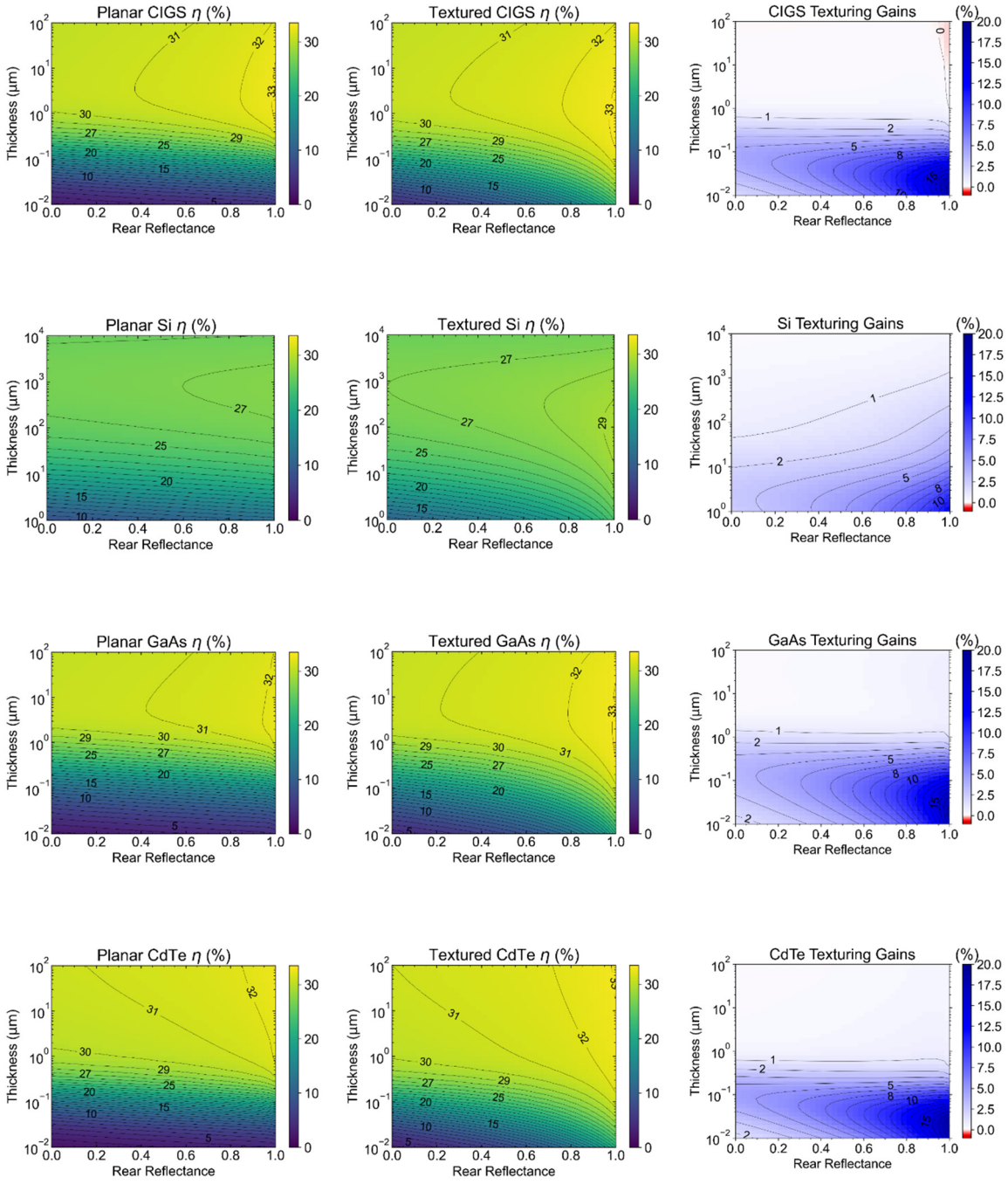

Fig. 15. Solar cell efficiency gains from light trapping for solar materials under planar. A textured cell with a Lambertian light distribution is strongly beneficial to direct-bandgap absorbers that are thin with near-ideal rear reflectance.

Technically, these plots only include two of the three effects of texturing as discussed in Section 2.I: the effect of internal reflection and light trapping is considered,

possible benefits on carrier collection of photogeneration moved to the front of the cell is considered, but no changes in the external front reflection are considered. The external front reflection is generally considered to be 0 in this chapter, i.e., a perfect antireflective coating is assumed.

The advantage of texturing – or more exactly the benefits of a Lambertian light distribution – is greatest in silicon as it brings the optimal efficiency up by 2% as well as decreases the optimal thickness from 1000 to 100 μm. Silicon efficiency is more sensitive to rear-mirror reflectance in the Lambertian case, as path-length enhancement increases from 1 to 2 with just texturing or with just rear reflectance, but it increases to $4n^2 \approx 50$ with the benefit of both texturing and rear reflectance. This result shows that the rear reflector is crucial to silicon efficiency – not just thin films. At 20 μm, bringing textured silicon's rear reflector from 0 to 1 boosts efficiency by 5% absolute.

As seen in the isocontour plots of Figure 15, the advantage of texturing is greatest in silicon as it brings the optimal efficiency up by 2% as well as decreases the optimal thickness from 1000 to 100 μm. Silicon efficiency is more sensitive to rear-mirror reflectance in the textured case, as path-length enhancement increases from 1 to 2 with just texturing or with just rear reflectance, but it increases to $4n^2 \approx 50$ with the benefit of both texturing and rear reflectance. This result shows that the rear reflector is crucial to silicon efficiency – not just thin films. At 20 μm, bringing textured silicon's rear reflector from 0 to 1 boosts efficiency by 5% absolute.

Figure 15 shows that most materials typically yield higher efficiencies under a Lambertian light distribution. Note again that these calculations assume ideal material without trap-assisted recombination, parasitic absorption, or series resistance (although

those effects can be increased as a consequence of texturing). Some thin films do, such as CIGS, however, yield lower efficiencies at high thicknesses with R = 1, where the benefits of increased J_{SC} are outweighed by the impact of increased radiative recombination. There is an apparent synergy between the material qualities in Fig. 15: more efficiency gains are available from rear reflectance when the absorber is thin and textured. Another interesting feature is sharp contour bending for the planar CdTe values near ideal rear reflectance. This bending can be explained by the enhanced benefits of photon recycling as rear-radiative recombination nears zero. V_{OC} has a logarithmic dependence on the radiative flux through $V_{oc} = (kT/q)\ln(J_{sc}) - (kT/q)\ln(J_{front} + J_{rear} + J_A)$, which describes the superlinear behavior of CdTe efficiency as J_{rear} reaches 0. The other direct bandgap materials experience higher J_{front} due to their lower bandgap, which reduces the significance of J_{rear} reaching 0.

Finally, the possibility that light trapping can increase surface recombination is examined. For the simulations in the next two figures, it is considered that light trapping increases surface recombination by a factor of five. Five is the effect of texturing on surface recombination that is found in the experiments of Glunz et al. upon Si, as reported by Altermatt et al. [146]. Schafer et al. published a similar value of 4× for the effect of texturing on SRV for Si [147]. For GaAs, this number will depend on the texturing and passivation, but it seems that a 5× amplification of surface recombination is a reasonable expectation for the effect of texturing.

Finally, the role of surface recombination is examined in Fig. 16. This is shown for a p-GaAs absorber with 10^{17} cm^{-3} doping and without extrinsic bulk recombination. For the plot on the left, the SRV of the planar cell is considered to be 100 cm/s, while the

surface recombination of the textured cell is 500 cm/s. The plot on the right also considers a 5× difference, but the planar cell SRV is 10^6 cm/s and the textured one is $5 \cdot 10^6$ cm/s. We see that for the GaAs material starting with the low planar surface recombination velocity, the efficiency generally increases with texturing - despite the increase in texturing. The maximum efficiency goes from 32.6% to 32.8% with the change in texturing and SRV. For the material with the higher planar SRV, however, some thicknesses will experience a lower efficiency due to texturing. For thicknesses roughly between 0.4 μm and 3 μm, the efficiency drops up to 1.1% absolute due to the effect on SRV. For larger thicknesses, light trapping has little to no impact. Note that these simulations were done with only surface recombination at the back of the cell. They were also done without bulk trap-assisted recombination. The succeeding figure shows the impact of texturing considering a bulk nonradiative lifetime of 10 ns. It is seen that the overall trend of the efficiency gains does not change. For the case of a material with a planar SRV of 100 cm/s, however, the maximum thickness at which a cell with an ideal rear mirror benefits from light trapping changes from 0.8 μm to 2 μm after including low bulk lifetimes.

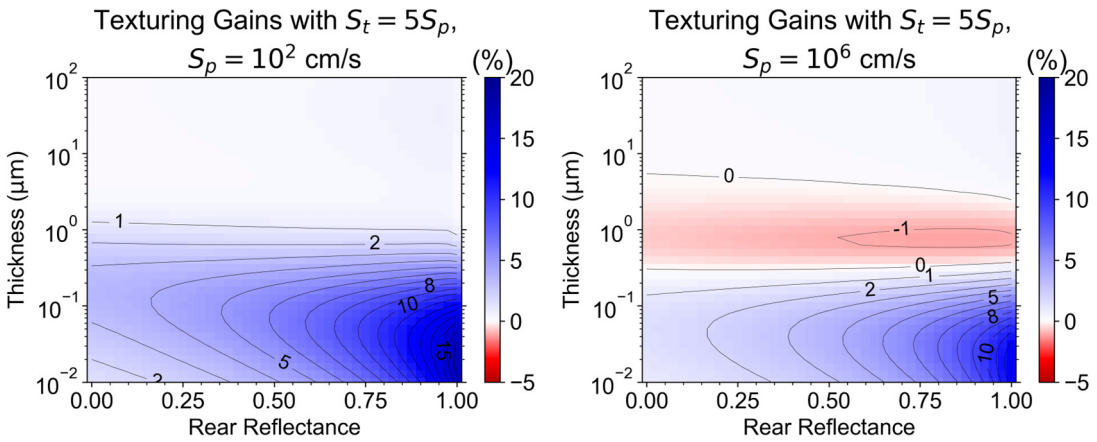

Fig. 16. Impact of Lambertian light trapping on GaAs, considering a 5× amplification of surface recombination due to texturing. The two plots are for the cases of a low (left) and a high (right) surface recombination velocity of the planar material, S_p.

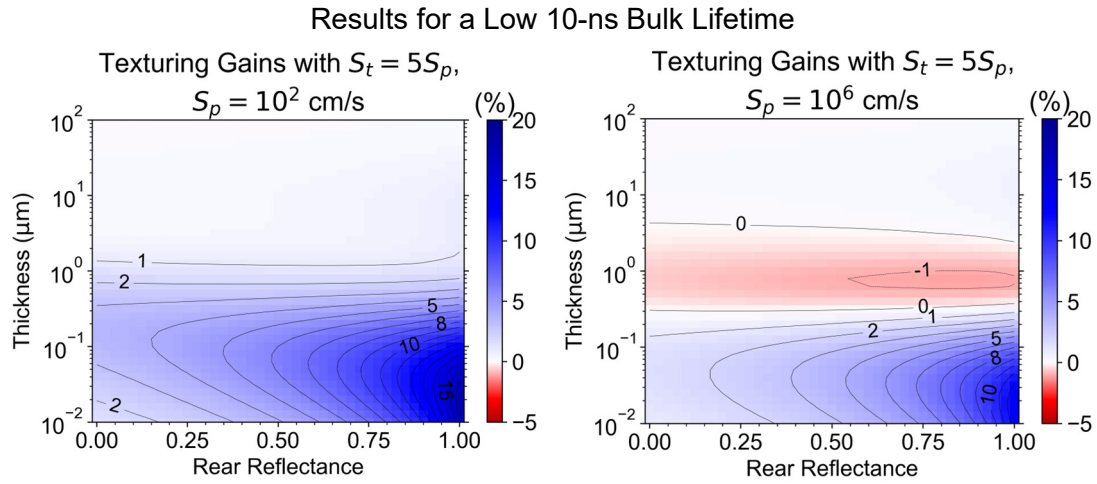

Fig. 17. Impact of light trapping and increased surface recombination velocity on GaAs cells with a 10 ns bulk lifetime.

While maximum thickness at which GaAs on a rear mirror will benefit from light trapping is changed from 0.8 to 2 μm for lower bulk lifetime materials in the case of low surface recombination, that thickness stays at 0.4 μm for the higher surface recombination regardless of bulk lifetime. In general, it is seen that light trapping yields more benefits to materials that are either thin or have low surface recombination velocity. Furthermore, for materials with a lower surface recombination but high bulk nonradiative

recombination, light trapping allows for one to reduce the absorber thickness to reduce the overall recombination density.

III. Conclusion of the Benefits of Light Trapping

A novel equation for rear emittance was derived for materials with partial rear reflectance and internal Lambertian light distribution (LLD). A cell under LLD light trapping incurs more radiative recombination emitted out the front but less out the back relative to a planar cell. A V_{oc} gain in silicon cells is expected under LLD due to a second-order effect of increased J_{sc}. A V_{oc} loss is generally seen in direct bandgap cells due to LLD enhancement of front radiative recombination. Nevertheless, thin films were shown to benefit significantly from a Lambertian light distribution for low thicknesses and high rear reflectance. Except for some thicker CIGS, the net effect of an LLD light trapping is to increase the photovoltaic overall efficiency – at least when only considering the fundamental effect of LLD on absorption and radiation. When considering the possibility that light trapping strategies can increase surface recombination velocity, however, it shown how the efficiency gains – or losses – due to light trapping depend on the absorber thickness, rear reflectance, and relative amounts of surface to bulk nonradiative recombination.

CHAPTER 5

BULK AND SUFRACE RECOMBINATION OF III-V MATERIAL

The extent to which light trapping benefits a material depends significantly on carrier lifetime. If the carrier lifetime of a material is relatively low, then many charge carriers will recombine before reaching electrical contacts. By increasing absorption, light trapping allows for a reduction in absorber thickness, reducing the distance to contacts. Thus, light trapping is particularly beneficial for materials with low bulk lifetimes.

In this chapter, the recombination characteristics of GaAs, a mature material with high mobilities, and GaNP, a novel material system with relatively low mobilities, will be measured. The effect of light trapping on each system will then be assessed.

I. DILUTE NITRIDE GANP

Si-based tandems are increasingly investigated as single-junction silicon approaches its practical efficiency limits. A key challenge for integrating Si and III-V into a tandem cell is the lattice mismatch between Si and most III-V materials. Dilute nitrides in the InGa(N)PAs system can achieve both lattice matching and the optimum bandgap for a Si-based double junction. This work focuses on $GaN_{0.02}P_{0.98}$. This GaNP material was verified lattice-matched to Si through XRD.

This section gives select results from my conference proceedings, Ref. [58]. The materials were mainly prepared by my colleagues Chaomin Zhang and Srinath Murali [148]. The steady-state photoluminescence was carried out by colleagues at University of Oklahoma, including Hadi Afshari. The dissertation author performed the time-resolved photoluminescence.

A. Steady-State Photoluminescence

Unlike GaAs, dilute nitride material typically experiences substantial benefits from post-growth annealing, partially due to a lower growth temperature. The optimal annealing conditions were 875°C for 2-5 min, as documented in my paper [58]. This RTA condition leads to higher PL at the bandgap and lowers PL and sub-bandgap (defect) energies. Hydrogenation conditions have not yet been optimized.

Fig. 18 compares the as-grown and annealed samples (200-nm GaNP heterostructure) at varying PL temperatures.

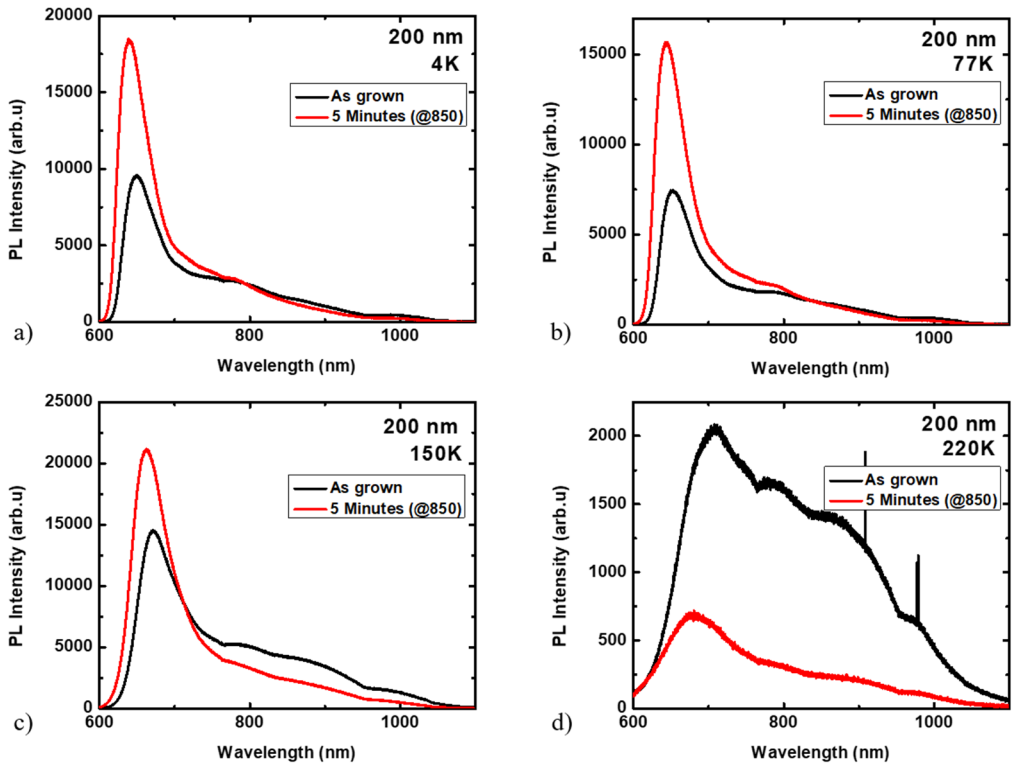

Fig. 18. Temperature-dependent photoluminescence. At low temperatures, the annealed sample shows high photoluminescence at the bandgap of 600 to 650 nm, thus exhibiting higher radiative efficiency for annealed samples. At high temperatures the unannealed sample shows higher photoluminescence sub-bandgap energies, which indicates a higher trap density in the unannealed sample.

At higher temperatures, the unannealed sample exhibits higher long-wavelength luminescence suggesting worse carrier localization than the annealed sample. The band-to-band luminescence, centered near 630 nm across the temperature range, is higher for the annealed sample, which also indicates greater radiative efficiency for the annealed sample.

Fig. 19 shows the evolution of the PL peak over temperature (for the 500 nm sample under a 424 nm laser after hydrogenation and annealing). The peak intensity begins dropping at 35K and then decreases by orders of magnitude by 295K. The peak energy decreases and then increases, whereas typical III-V material will only show decreasing peak energy with temperature.

The shift in peak energy, traced in Fig. 20a, exhibits an S-shaped curve typical in dilute nitrides experiencing carrier localization at low temperatures [61]. The minimum of the curve is at 200K. At 200K, the peak energy is also dependent on the laser power, as shown in Fig. 20b. The increase in peak energy at this temperature shows saturation of states within the bandgap, pushing luminescence to higher energies. The phenomenon suggests partial localization of carriers at low temperatures. This localization complicates the interpretation of TRPL data, which was only detectable at low temperatures.

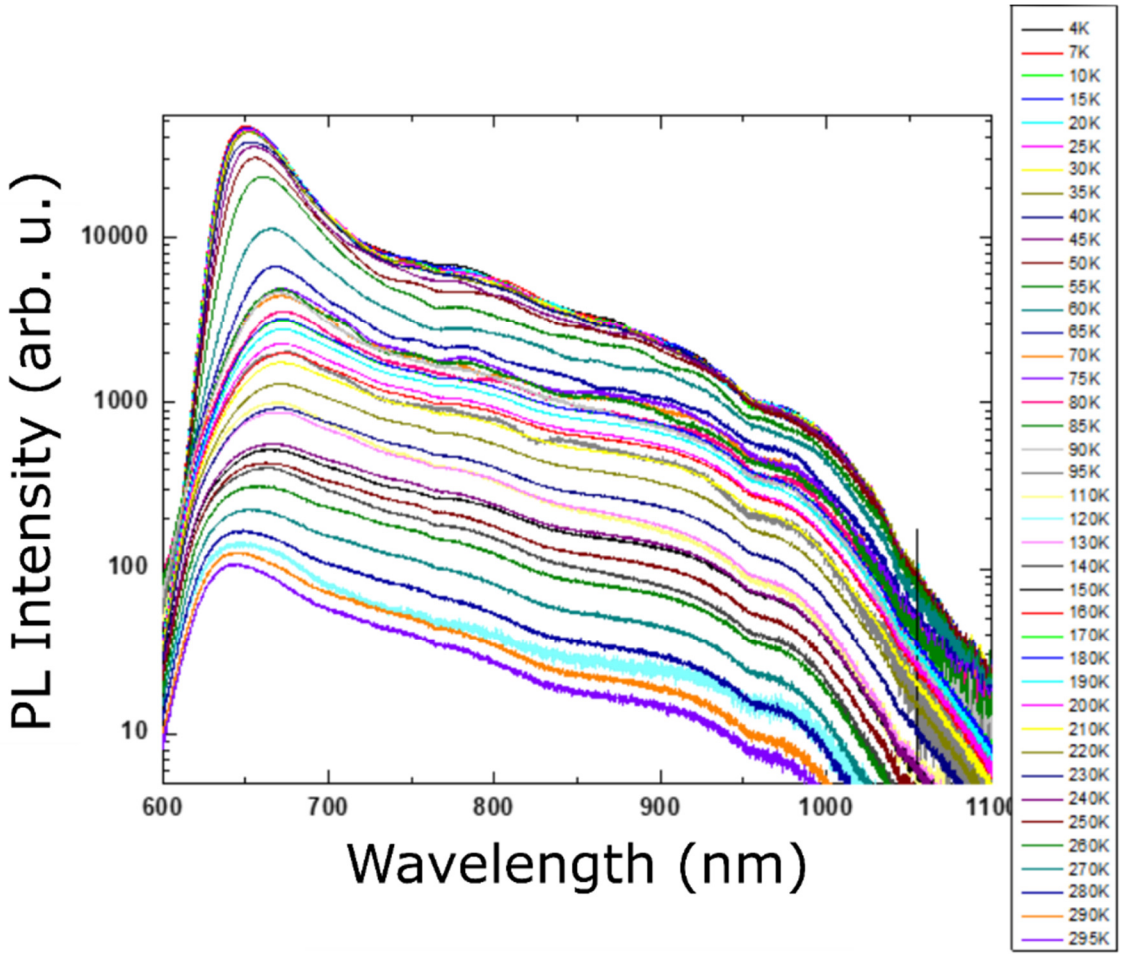

Fig. 19. PL curve of the annealed and hydrogenated sample at varying measurement temperatures. The main peak first shifts rightwards, then leftwards with increasing temperature.

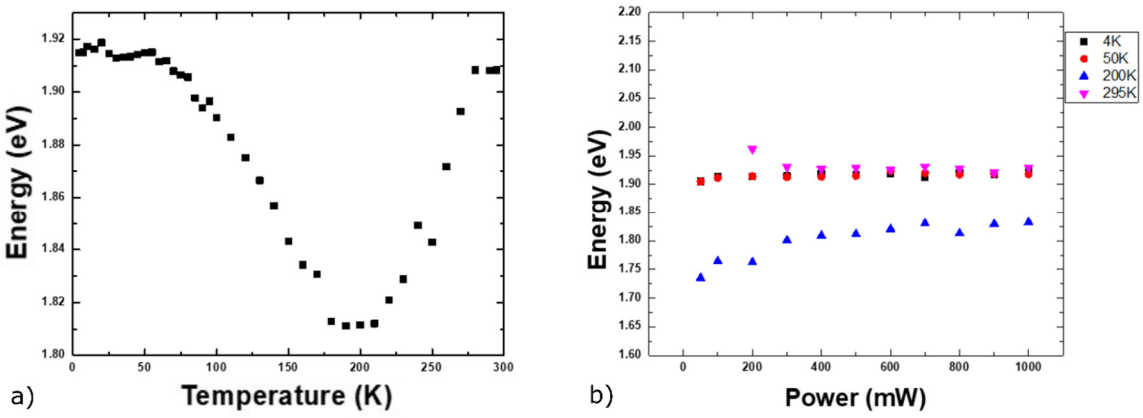

Fig. 20. Evidence of carrier localization at low temperatures. a) Temperature dependence of the PL peak. The peak energy of 0 follows an S-shaped curve with a critical point at 200K. b) Power dependence of the PL peak. At the critical point of 200K, the peak energy changes with laser power, implying saturation of localized states.

B. Time-Resolved Photoluminescence on GaNP

Time-Resolved Photoluminescence (TRPL) was taken to determine the carrier lifetime for intrinsic GaP/GaNP/GaP/Si double heterostructures. The TRPL system chops 540-nm emission from a Fianium laser into a 100-fs pulse with a rep rate of 0.5MHz. The TRPL signal is thus much lower than a regular PL signal, and for this material, the TRPL signal falls below the background noise at around 170 K.

Fig. 21a presents TRPL curves taken at 78K on the 500 nm sample. The curves correspond to different detection wavelengths. The shorter wavelengths exhibit a bi-exponential curvature, whereas the longer wavelengths show only one large exponential component. Global analysis was performed to fit two lifetimes across seven detection wavelengths. Amplitudes were allowed to vary but the two lifetimes held fixed across the wavelengths. The lifetimes here were fit at 5 and 115 ns.

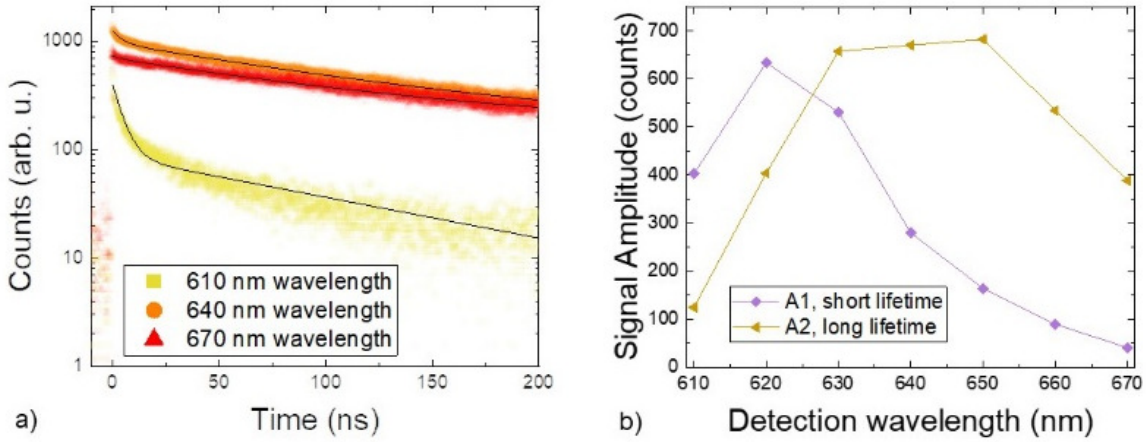

Fig. 21. Influence of detection wavelength on decay curve at 78K. a) TRPL curves and biexponential fits, where the two lifetimes are fixed across the detection wavelength through global analysis. b) Decay-associated spectra, which show the short-lifetime component peaks at a shorter wavelength.

Decay-associated spectra are given in Fig. 21b. The short-lifetime component is seen to peak at 620 nm, whereas the long-lifetime component peaks at 650 nm. Authors differ on how to identify each component. Some authors associate the short component with free carrier recombination and associate the long component with localized carrier recombination [57]. Other authors associate the short-lifetime component with transient behavior and associate the long component with recombination [149]. This report will now focus on the long component as it yields a greater signal.

Decay curves for hydrogenated and as-grown samples are compared in Fig. 22a. The as-grown signal decays noticeably faster. The hydrogenated (and annealed) sample decays almost identically to the sample that was only annealed.

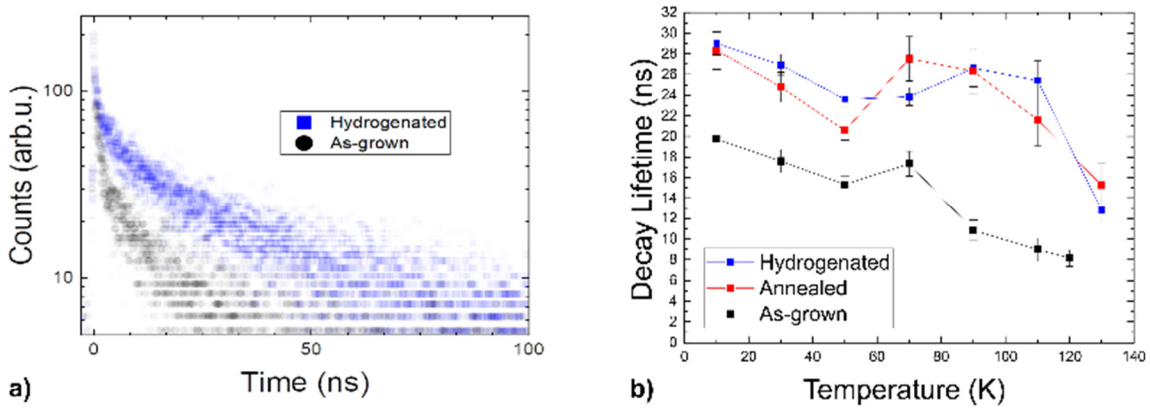

Fig. 22. Representative TRPL Decay curves for the 500-nm, unannealed GaNP sample (a) and corresponding lifetime-vs-temperature chart (b). TRPL curves were fit by an exponential with a y-offset. Lifetimes dropped gradually while the peak signal dropped with increasing temperature.

Changes in lifetime with temperature are depicted in Fig. 22b. The as-grown samples show a relatively monotonic decrease in lifetime with measurement temperature, whereas the treated samples show higher lifetimes and a significant peak around 80K. Similar features were also found by Balanta in [57].

The dependence of lifetime on absorber thickness W is investigated in Fig. 23 for as-grown samples. The thinner samples of 100 and 150 nm GaNP are excluded from the analysis as their lifetimes are orders of magnitudes smaller than the 200 nm sample. The thin samples do not fit the classical theory, possibly due to quantum effects. Using Equation 28, the SRV is found as $S = 730 \pm 130$ cm/s. The extracted bulk lifetime is $\tau_{bulk} = 300 \pm 400$ ns. The large uncertainty in the bulk lifetime results from the intercept being relatively close to the axis origin.

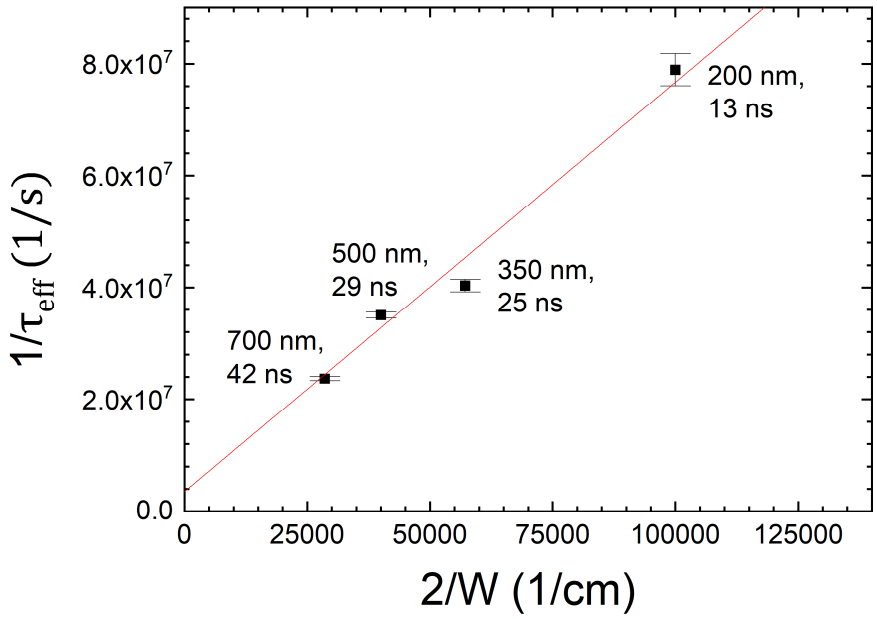

Fig. 23. Relationship between effective lifetime and absorber thickness at 11K. The plotted variables are chosen to linearize the relationship. The extracted SRV is 730 cm/s.

The measurement temperature for SRV, however, was 11K, so the carriers are partially localized and may not follow conventional surface recombination analysis. To determine SRV at room temperature, the team plans to fabricate contacts and fit SRV to the quantum efficiency curve.

C. Interaction between GaNP recombination and light trapping

The impact of light trapping is given in Fig. 24 for a GaNP solar cell with an SRV of 730 cm/s. Two material sets are used: one for the 300 ns bulk lifetime measured at 11K and another for the bulk lifetime extrapolated to room temperature. The extrapolation was done with data from [150] by assuming the same 600x decrease in lifetime with temperature seen by their $GaN_{0.012}P_{0.38}As_{0.608}$/GaP material, giving 0.6 ns.

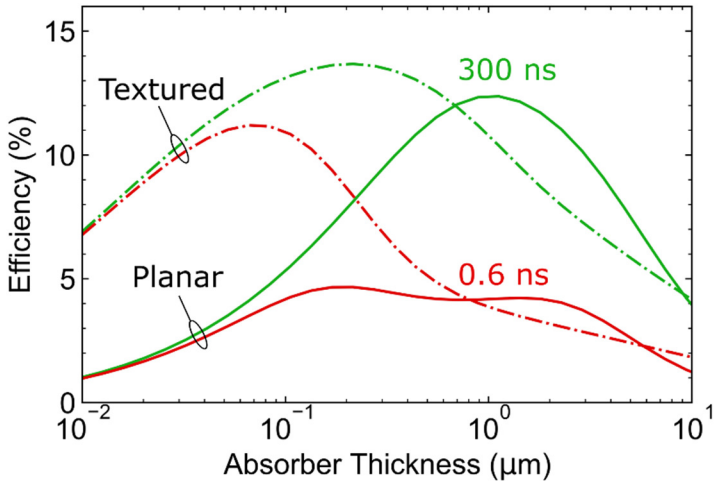

Fig. 24. a) Benefits of Lambertian light trapping (texturing) for two sets of GaNP: high bulk lifetime (measured in low-temperature TRPL) and low bulk lifetime (extrapolated for room temperature material).

The plot shows that light trapping is critical to the low-lifetime material, more than doubling the maximum efficiency. Note that the planar curve already assumes a perfect rear reflector, otherwise the calculated efficiency would be even lower.

II. GaInP/GaAs/GaInP

In this section, two different GaAs growths methods are compared for: 1) material grown with metal-oxide chemical vapor material (MOCVD) grown by our industrial partner VEECO Inc. and 2) material that I grew with molecular beam epitaxy (MBE). MOCVD uses a relatively large-scale chamber, making it more appropriate for manufacturing. MBE uses an ultra-high vacuum chamber with lower deposition rates, making it better suited for researching quantum well structures that require abrupt interfaces.

For each material, four double-heterostructures were grown with variable absorber thicknesses, as shown in Fig. 25. The variable thickness allows for the separation of bulk and surface effects during analysis. The material stack was identical, except different doping sources were available. It is expected that the Te dopant used for MOCVD could yield slightly higher lifetimes than the Si dopant used for MBE, as Te can act as a surfactant [151] and experiences lower diffusion [152].

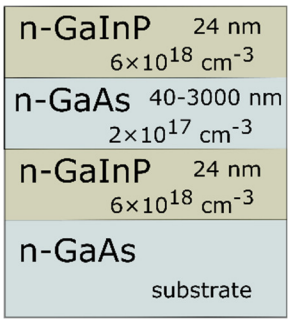

Fig. 25. Material stack for both the MBE and MOCVD-grown double-heterostructures. The only difference besides the growth method was that the n-type dopant was Si for MBE growth and Te for MOCVD.

A. General Material Characterization for GaAs

After the growth of the MBE material, I performed various characterization techniques - the most critical being x-ray diffraction (XRD). XRD was used to calibrate Ga/In flux ratio for lattice matching between GaAs and GaInP. Fig. 26 compares XRD

results of lattice matches, showing the Ga/In flux ratio third sample to give proper lattice matching.

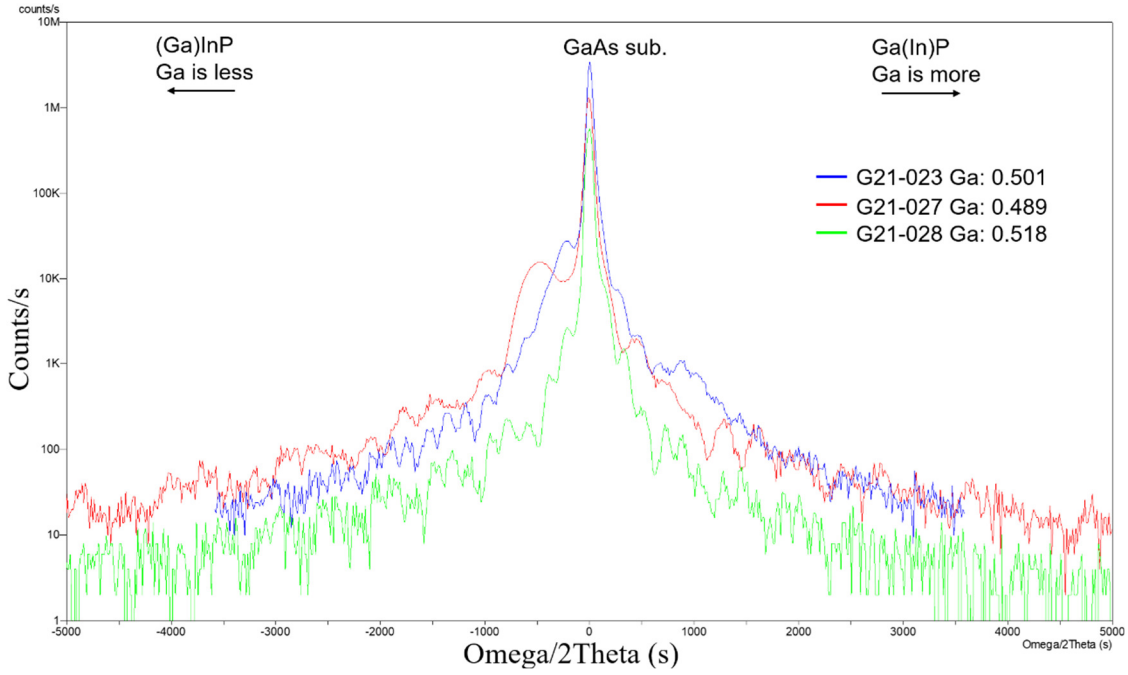

Fig. 26. X-ray diffraction (XRD) was used to calibrate the Ga/In flux ratio. The last sample exhibits lattice matching between the GaInP epitaxial layer and GaAs substrate.

Other tools I used to characterize the material include scanning electron microscopy (SEM), secondary mass electron mass spectroscopy (SIMS), Hall measurement, and time-resolved photoluminescence (TRPL). The SEM and SIMS were used to verify the growth speed. The SIMS and Hall measurements were used to verify doping concentrations. The SIMS could not detect the level of contamination, as background levels in the measurement chamber – particularly H, C, and O – were too high.

B. Time-Resolved Photoluminescence (TRPL) on GaAs

TRPL was performed on the material of Fig. 25 with the method of Section 3.II at room temperature. The measurement used a laser of 700 nm with a 443mW pulse power. Decay curves are given in Fig. 27.

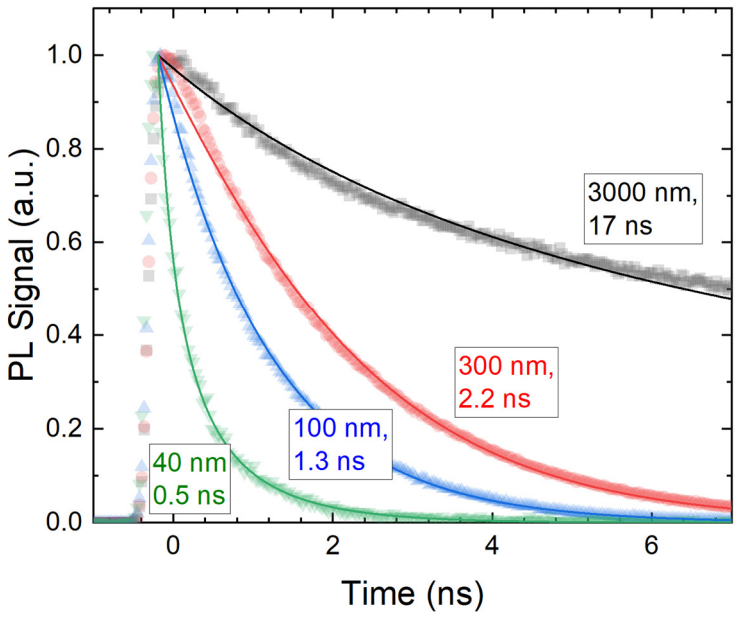

Fig. 27. TRPL decays curves for MBE-grown GaAs. Also plotted are the fitted exponential-decay curves with the fitted effective lifetime. Thicker absorbers yield greater lifetimes, as expected.

The fitted lifetimes as a function of thickness were then analyzed to separate surface and bulk effects. The inverse of effective lifetime τ_{eff} and absorber thickness W is plotted in Fig. 28, which linearizes the relationship in Equation 28. From this equation, the slope is identified as the reciprocal bulk lifetime $1/\tau_{bulk}$, and the slope is identified as the SRV S. Extracted values are given in Table 4.

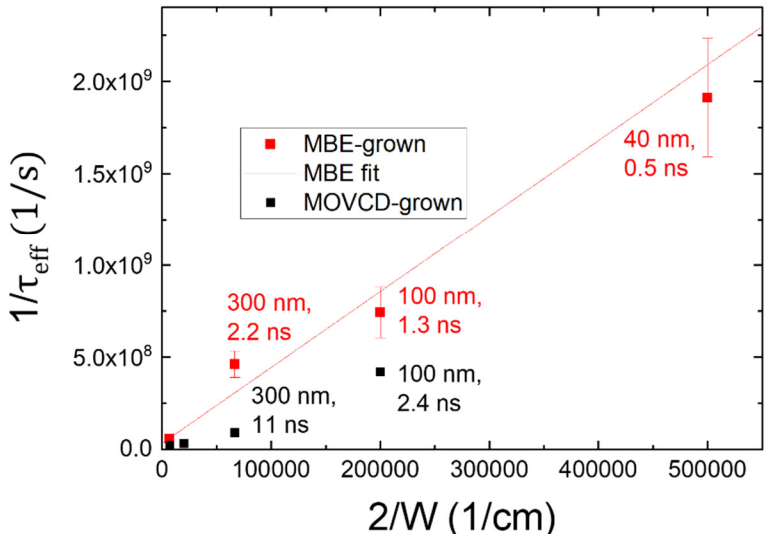

Fig. 28. a) Extraction of bulk lifetime and SRV from thickness W dependance of the effective lifetime τ_{eff}. b) Resulting values for both MBE and MOCVD-grown GaAs. The MBE-grown material is seen to have worse bulk lifetimes and SRV by factors of 3-4.

Table 4
EXTRACTED MATERIAL PARAMETERS

	τ_{bulk} (ns)	SRV (cm/s)
MBE-Grown	32 ± 5	4100 ± 800
MOVCD-Grown	100 ± 30	1210 ± 60

The lower value of bulk lifetime in MBE compared to MOCVD lifetimes is seen in various literature sources [152], [153], [154], [155], [26]. For example, the MBE-grown material in [153] received 4x lower lifetimes than the MOCVD material – even though MBE growth parameters were more thoroughly optimized! The difference in material quality may occur for many reasons, including the different growth rates, impact energies, and dopant (Si for MBE vs. Te for MOCVD).

C. Interaction between GaAs recombination and light trapping

If the material has low bulk lifetimes, then light trapping allows for thinning the material to support carrier collection. The interaction of recombination parameters and light trapping is shown in Fig. 29 (calculated assuming perfect rear reflectors). The optimal MBE-grown efficiency increases by 5.3% (relative) from texturing, whereas the MOCVD material benefits by only 3.8%. For the lower-lifetime material, texturing allows increases absorption and allows for increased collection efficiency through thickness reduction.

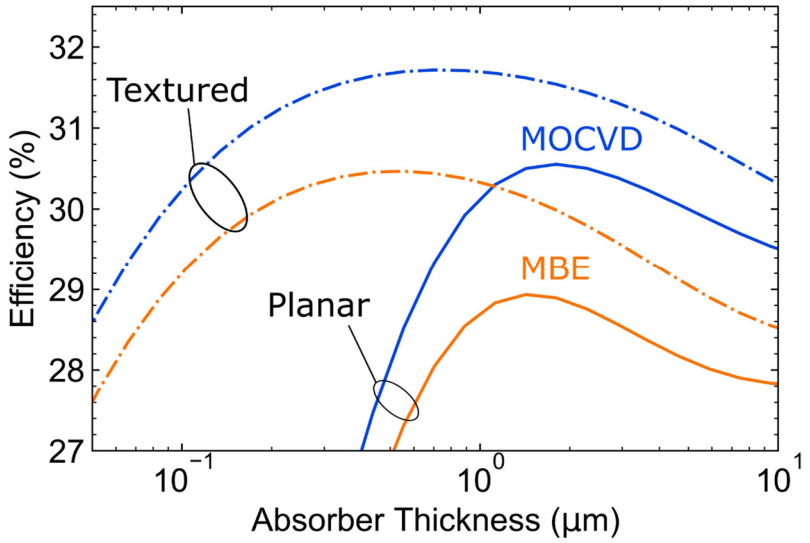

Fig. 29. a) Benefits of Lambertian light trapping (texturing) for the two GaAs material qualities. The MBE-grown material can benefit more from light trapping due to its lower bulk lifetime.

CHAPTER 6

NARROWBAND LIGHT TRAPPING FOR PHOTONIC POWER CONVERTERS

Photonic power converters (PPC) convert narrowband light into electricity. As the light source is oftentimes a laser, PPCs are also called laser power converters (LPC). PPCs are used to transmit energy over space. The benefits of transmitting energy in optical guides instead through conventional electrical wires are multifarious, as discussed in Chapter 1.

To achieve extreme light trapping, we propose to use nanostructures, such as those pictured in Fig. 30, to diffract incident light outside of the material's escape cone - thus trapping light inside the absorber. PPCs only require absorption of a single wavelength and angle, which offers new possibilities for advancing the limits of light trapping.

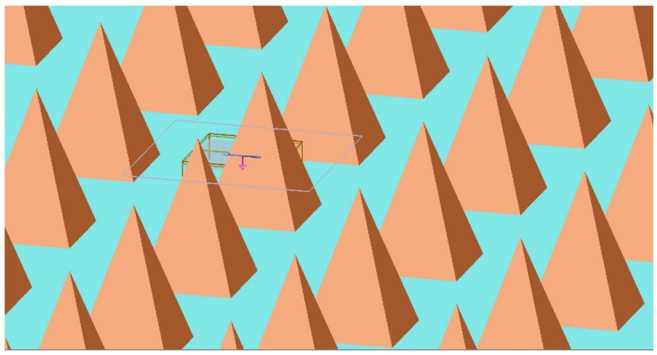

Fig. 30. Nanostructures for light trapping in thin films.

I. Device Modeling

Modeling was done to determine the efficiencies of PPC that could be achieved with the material grown with our MBE. The bulk lifetime and the SRV were inputted into the modeling of Section 3.I.B. The absorber thickness, the incident laser wavelength, and the path length enhancement X were varied. Results are given in Fig. 31 plotted for

optimal laser wavelength. Light trapping allows for greater efficiencies and lower optimum thicknesses. Extreme light trapping of 6000x increases the maximum efficiency by 16.1% absolute [156].

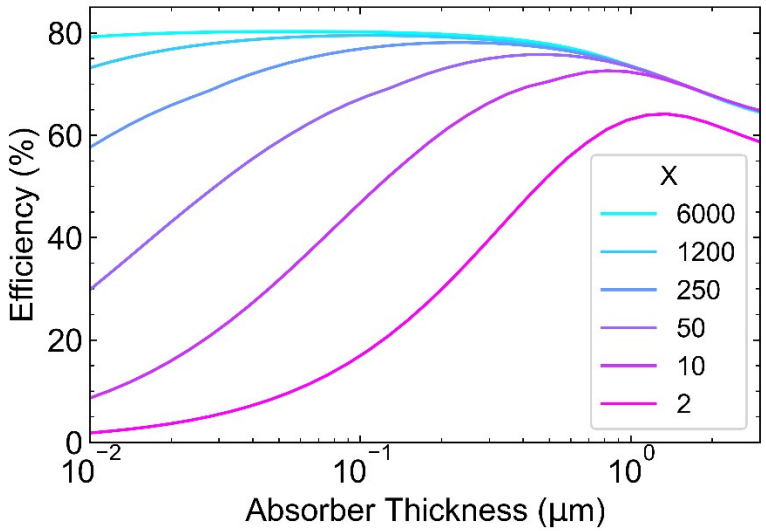

Fig. 31. PPC efficiency with increasing path-length enhancement X calculated with our measured lifetime and SRV. Increasing X from 2 (the planar limit) yields substantial efficiency gains.

Table 5
PPC Efficiency Calculated for Measured Lifetimes

Path-Length Enhancement X	**2**	**10**	**50**	**250**	**1200**	**6000**
Max. Efficiency	64.2%	72.6%	75.8%	78.1%	79.5%	80.3%

The impact of laser wavelength is examined in Fig. 32. The optimal laser wavelength is seen to be 871 nm. These calculations ignored, however, any distribution in the laser wavelength, whereas most lasers have a full width of half maximum (FWHM) around 1 nm. Future simulations will thus consider an 870 nm incident laser.

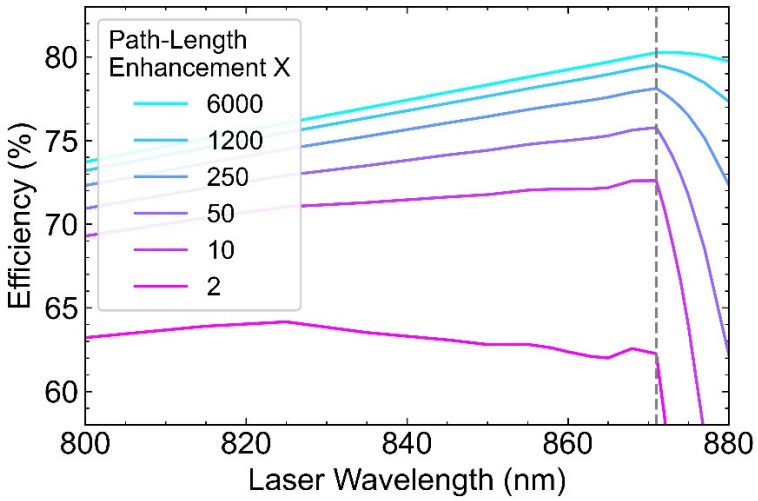

Fig. 32. Optimization of PPC laser wavelength. For $2 < X < 6000$, the optimal laser wavelength is 871 nm.

II. Optical Modeling

The electromagnetic modeling is primarily performed in the Ansys Lumerical finite-difference time-domain (FDTD) program, as detailed in Section 3.III.B.

A. Model Verification

To verify the utilization of Lumerical, results for a simple planar slab were compared against three other methods: 1) Macleod software 2) Beer-Lambert's equation with partial rear reflection at the rear, yielding a double-pass formula and 3) Beer-Lambert's equation with partial rear reflection at the rear and front, solved with an infinite series. The results, shown in Fig. 33, show general agreement between the methods, except that the absorption solved by the software shows resonant behavior.

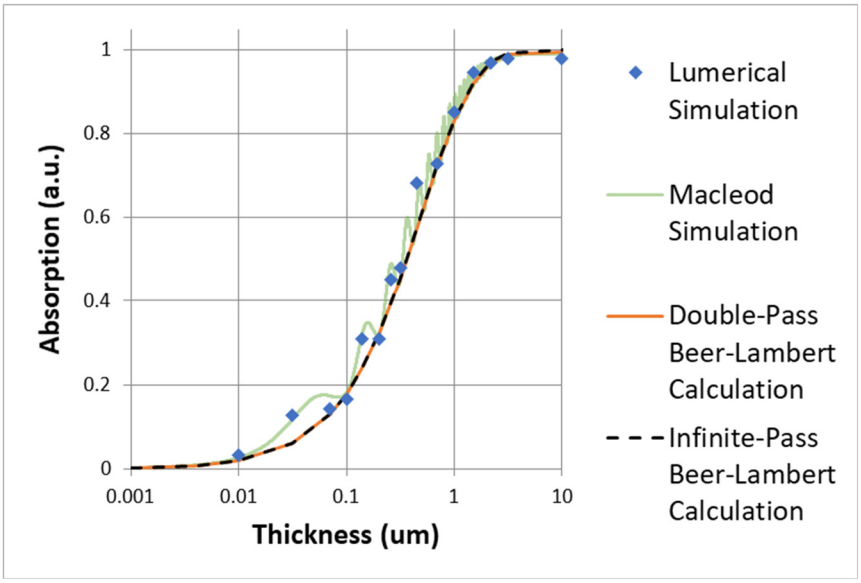

Fig. 33. Verification of Lumerical simulation by comparing to other results for a simple slab of GaAs with a rear mirror. The simulation results exhibit cavity resonances, whereas the Beer-Lambert results ignore such interference effects.

This comparison introduces the effect of cavity resonance, i.e., Fabry-Perot resonance. Here, reflection/transmission at the front interface causes two different wavefronts that can interfere. When destructive interference occurs between these waves at the front interface, the light becomes trapped inside the semiconductor. Cavity resonance can yield path length enhancement of around 7x for an air/GaAs interface. If an anti-reflection coating is added, then the interference is repressed, and cavity resonance becomes lost [157]. Surprisingly, a photonic power converter may before better without an anti-reflective coating.

B. Modeling of nanocones

The first nanostructure design used nanopyramids, but soon they were replaced with nanocones, as nanocones are more readily fabricated with anisotropic etching. Within FDTD simulations, the nanocone array is optimized over parameters such as nanocone geometry, layer thicknesses, and the index of an anti-reflective coating (ARC).

The baseline design as well as the parameters of optimization are detailed in Section 3.III.B. Importantly, the absorptance of the GaAs absorber was optimized from thicknesses of 70 nm to 120 nm.

Optimal performance was achieved without an ARC with truncated nanocones with a diameter 772.22 nm, a sidewall angle of 37.237°, a center-to-center spacing of 865.42 nm, and a height of 1.5 μm (but the height of the structures was not particularly critical to the absorption). A schematic of this design is shown in Fig. 34. This design achieves a 25x path-length enhancement for 866 nm light, which corresponds to an absorptance in the absorber layer of 91.17% for an absorber thickness of only 120 nm. This performance was up drastically from the optimal of the first campaign, which achieved only a 1.9x enhancement. The increase in enhancement occurred with many design changes, but the main improvement occurred after changing the rear metal from Al to Ag, and the insertion of a 217 nm SiO_2 layer between the rear semiconductor and the metal.

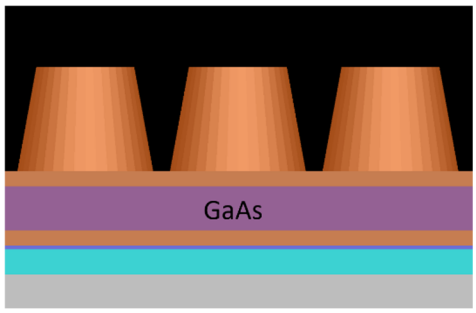

Fig. 34. Current nanocone design with highest path-length enhancement: $X = 25$.

A comparison of different nanostructure shapes, materials, and positions was performed with more particle-swarm optimization of absorptance. The absorption coefficient of GaAs at 866 nm is 8228 cm^{-3}. The resulting maxima absorptions and corresponding path-length enhancement of each optimization are given in Table 6 for a

GaAs absorber varied from 70 to 120 nm. While the front GaInP truncated nanocones showed the highest absorptance, the front GaInP nanodomes achieved the same path-length enhancement of 25× but with a thinner absorber material.

Table 6
OPTIMAL ABSORPTANCE (%) AND PATH-LENGTH ENHANCEMENT (X) ACROSS DESIGNS

	Front	Rear	Front and rear	Asymmetric front and rear
GaInP truncated nanocones	91.2%, 25x	74.4%, 17.7x	77.8%, 15.2x	77.8%, 15.2x
SiO2/GaInP truncated nanocones	88.6%, 22x			
SiO2 truncated nanocones	77.9%, 17.4x			
ARC/GaInP nanodomes	78.1%, 18.8x			
GaInP nanodomes	87.5%, 22.9x		62.6%, 12.1x	
SiO2 nanodomes	78.1%, 17.5x			

The absorber thickness optimized between 70 and 120 nm for each design.

The simulations with the antireflective coatings (ARC) nanostructures tended to do worse than those without. Similarly, the simulations with rear nanostructures did worse than the ones only with front nanostructures, possibly because the nanostructures are the features that provide resonant in-coupling into the material, so rear nanostructures could lead to greater transmission out into the rear metal layer.

The “asymmetric” column in the table refers to simulations where the rear nanostructures were optimized with different heights and diameters than the front nanostructures – but the position and the spacing were the same between the front and the rear nanostructures in order to set periodic boundary conditions within the simulation. Such boundary conditions are required to allow for extrapolation of a single unit cell, as

larger volume FDTD simulations would be too memory intensive for the simulation computer. If, however, the spatial periods of the front and rear nanostructures were allowed to be different, then it is expected that the front-and-rear optima could be greater than the front-only optima. This expectation is informed by the sensitivity of the design to the array spacing, as seen in the next plot.

The sensitivity of the optimal nanocone design is shown in the figure below. The absorptance is seen to be sensitive to the nanocone diameter and especially to the nanocone spacing. Just a 2% change in the spacing results in a 20% loss in absorptance. This is why electron beam lithography was chosen as the fabrication technique instead of self-assembled lithography, such as nanosphere lithography.

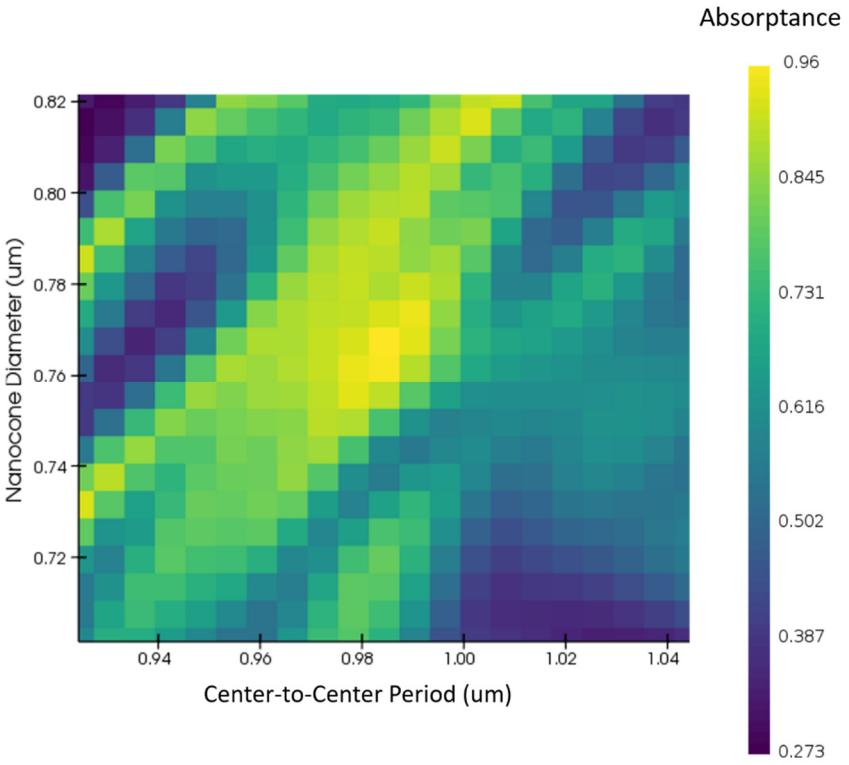

Fig. 35. Sensitivity of PPC absorptance to nanocone diameter and spacing.

Next, the sensitivity of the design to the GaAs thickness is explored in the figure below. For the nanocones with anti-reflective coating (ARC), strong resonances are seen

to lead to high and low absorptance values, with periodicity on the order of 50 nm. These resonances could be amplified versions of cavity resonances, i.e., Fabry-Perot resonances, perhaps hybridized with guided-mode resonances, judging by the amplitude and the periodicity of the resonances in the planar mirror curve. For the design without ARC, tolerance of the design to the GaAs thickness is improved. This design does not require an ARC as the nanocones give an in-coupling effect through nanostructure resonance.

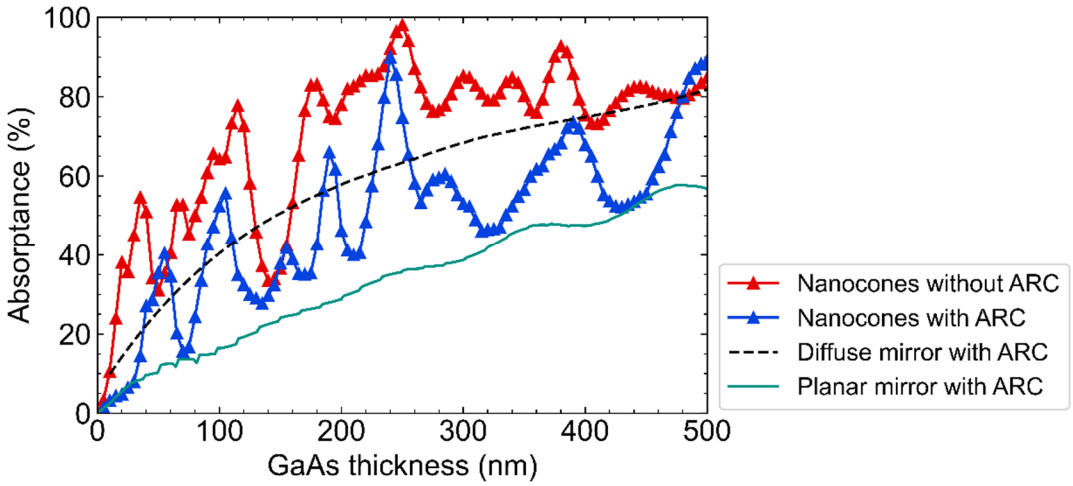

Fig. 36. Sensitivity of PPC absorptance to nanocone diameter and spacing.

The reason for the sensitivity to GaAs thickness is explored in the next figure. In the off-peak thickness, much more of the incident light reflects off the rear mirror and escapes out of the front of the device. At the peak absorber thickness, the light escaping out of the front mirror is far lower. This phenomenon suggests that the presence of constructive versus deconstructive interference at the front surface largely determines the efficiency of the light trapping, explaining the sensitivity of the absorptance on the GaAs thickness. This sensitivity is reduced for the material without the ARC because there the internal front reflection is higher, leading to greater light trapping.

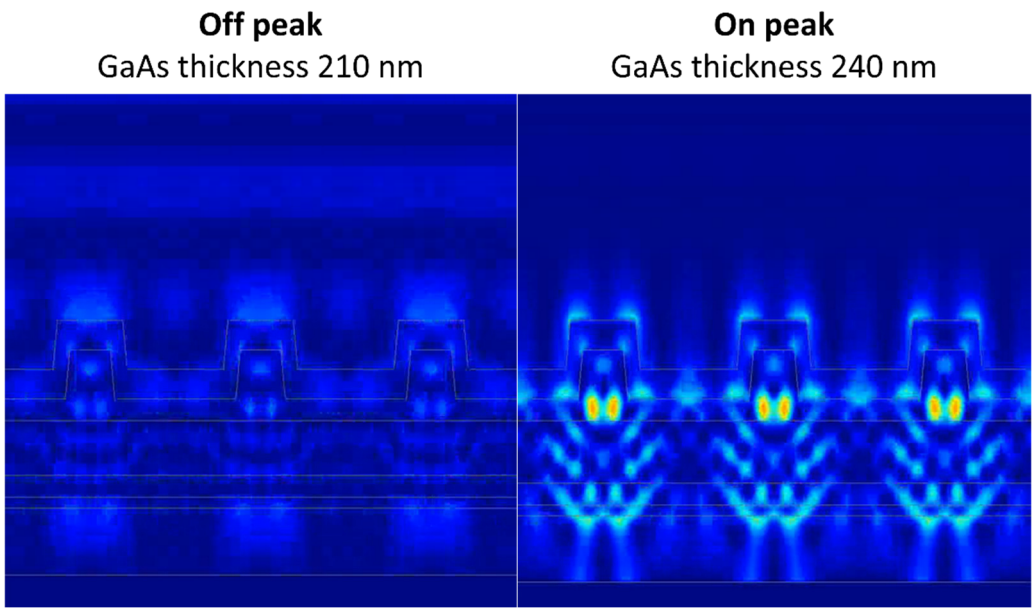

Fig. 37. Electromagnetic leakage out of the front of a PPC device with sub-optimal (left) versus optimal (right) GaAs thickness.

III. NANOTEXTURING RESULTS

A. Fabrication of nanocones

This fabrication of nanocones was done at the University of Ottawa. Most of the fabrication was done by Mathieu de Lafontaine, only with some reactive ion etching done by this dissertation's author. The fabrication technique was electron-beam lithography, as detailed in Section 3.IV. The nominal geometry is disks in a hexagonal lattice with diameters of 600 nm and gaps of 150 nm. The electron-beam resist used was ZEP520A. The EBL steps are detailed in Section 3.IV.

The atomic force microscopy (AFM) image of the EBL structures is given in the figure below. Although the shape does not look completely circular, possibly due to a tilt in the AFM tip, the gaps do look uniform from structure to structure, which was the

principal reason to use EBL over self-assembled lithography such as nanosphere lithography.

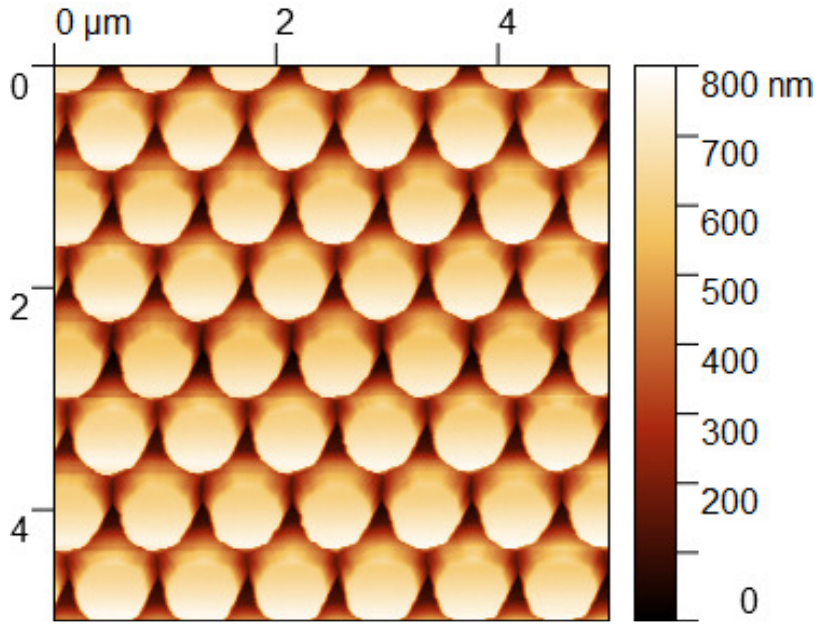

Fig. 38. Atomic force microscopy (AFM) surface roughness of resist nanostructures after lithography but before etching. The ZEP520A resist is patterned on top of a GaInP surface.

Although AFM images give quantitative information, they are liable to introduce artifacts. In particular, they are not typically able to sense undercutting. It is thus useful to combine AFM with microscopy imaging to characterize nanostructures. Microscopy images from focused ion beam scanning electron microscopy (FIB-SEM) are presented below.

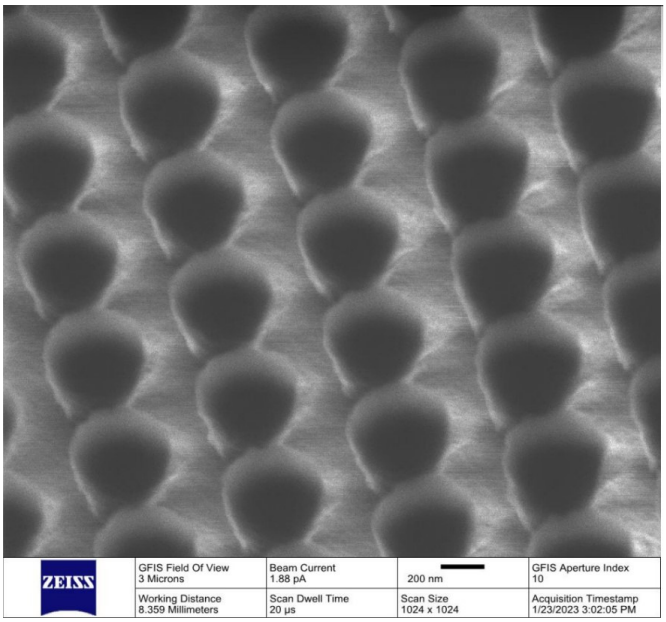

Fig. 39. Image from focused ion beam scanning electron microscopy (FIB-SEM) of resist nanostructures after lithography but before etching. The ZEP520A resist is patterned on top of a GaInP surface.

After EBL, the next main step in fabrication is plasma etching. The plasma etch conditions are detailed in Section 3.IV. The AFM and SEM characterizations of the etched nanostructure shapes are in the two figures below.

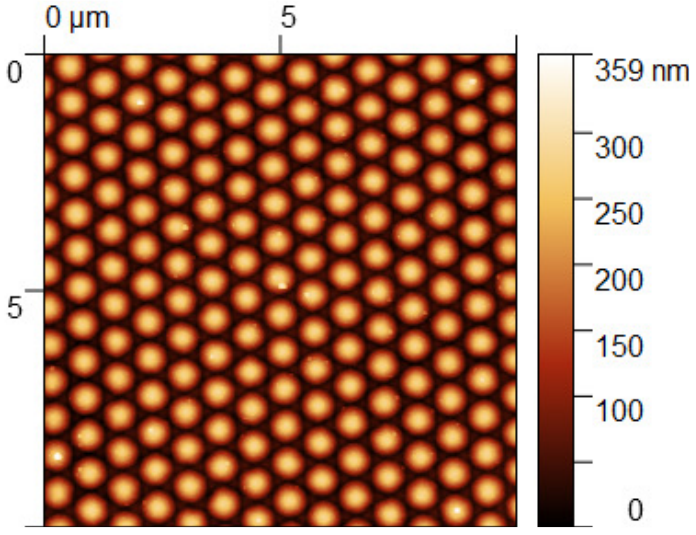

Fig. 40. AFM of GaInP nanostructures. Imaging was done after plasma etching transferred the pattern from the resist into the 250 nm GaInP layer and – partially into the GaAs base layer.

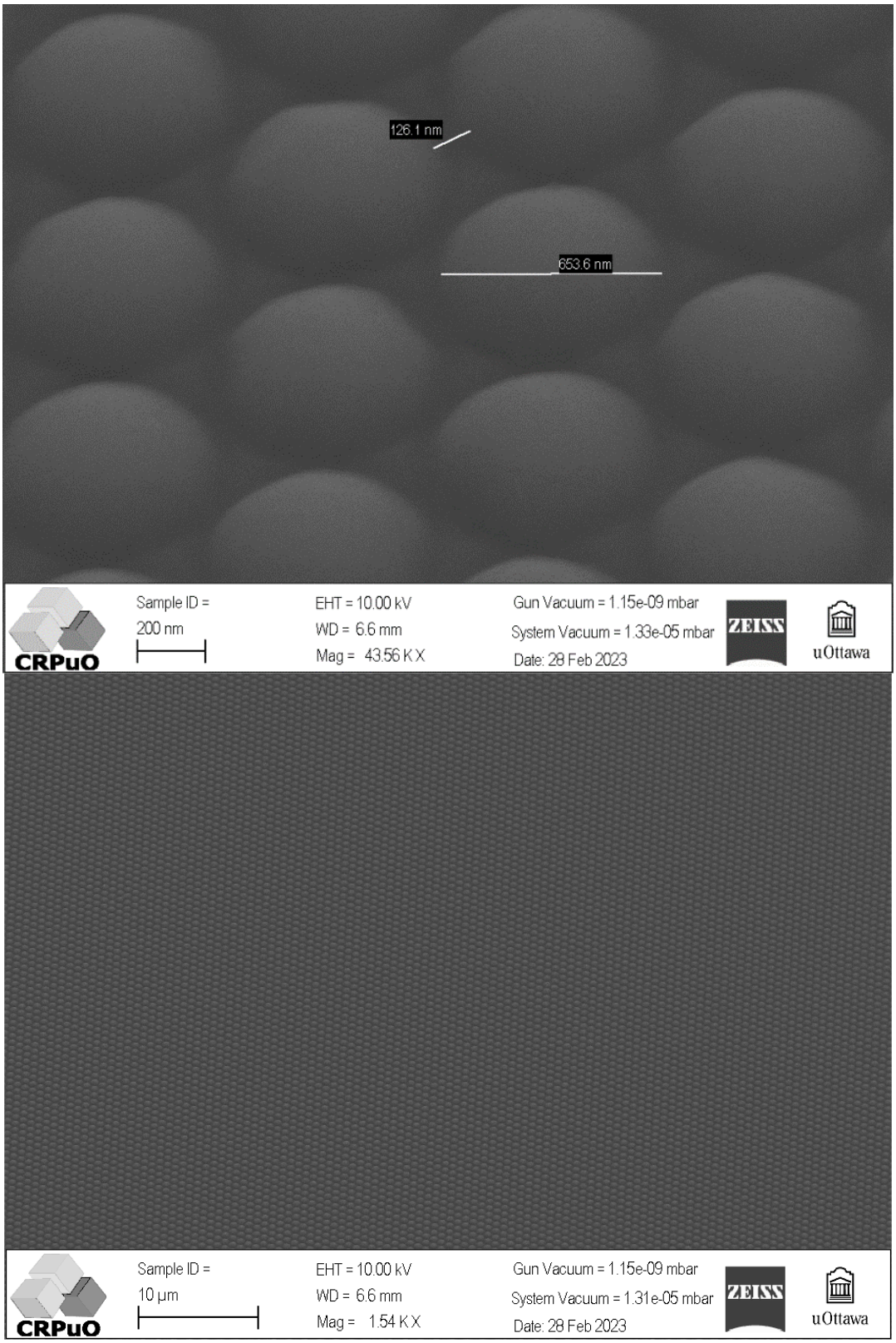

Fig. 41. Image from focused ion beam scanning electron microscopy (FIB-SEM) of GaInP/GaAs nanostructures after plasma etching.

The nanostructure shape within the FIB-SEM images appears to be semi-ellipsoid. If truncated nanocones are desired as opposed to semi-ellipsoid, then a couple of processing changes could be explored. First, a reduced EBL dose could be applied to limit the undercutting seen in Fig. 39. Proper dose reduction would require a study such as the one shown in Fig. 7 of Elsner et al. [158] in order to find the lowest EBL dosage that fully removes the resist layer. The next alteration could involve reducing the bias power to reduce the sidewall faceting of the EBL resist.

An important note to make on the plasma etching is that, with a bias platen power of 70 W, the approximately 500-nm thick EBL resist is completely removed by the time the etch gets through about 200 nm of planar GaInP. In other words, the selectivity of the etch recipe for GaInP over the ZEP500a resist is only about 0.4. To gain greater control over the fabricated nanostructures, then, EBL resists with a higher selectivity could be explored, such as the Micro-Resist-Technology GmbH Ma-N [159] or Hydrogen silsesquioxane HSQ [160]. These resists are, however, negative EBL resists, so their use would require a redesign of the EBL procedure. A similar argument could be made for the use of a SiO_2 hard mask, that it could give a greater selectivity, but it would require development of two plasma etching recipes instead of one.

Nonetheless, the nano-ellipsoids seen in the FIB-SEM image are remarkably uniform across the wafer, satisfying the main requirement as seen from the FDTD simulations. As seen in the previous section, nano-ellipsoids can yield absorptance values that are nearly as high as that of truncated nanocones. The next step to check is whether the nanotexturing process has affected material lifetime.

B. Effect of Etching on Material Lifetime

EBL and plasma etching followed by time-resolved photoluminescence (TRPL) was applied to a double heterostructure to assess the effects of nanostructures on the material lifetime. The TRPL laser was a 532 nm solid-state laser. A 750 nm long pass filter was placed between the sample and the single-photon counter, which was verified to filter photoluminescence from the GaInP passivation layer as well as most laser light from the detector. Further details are given in section 3.II.

The double heterostructure samples are formed of layers of 250 nm GaInP/250 nm GaAs/250 nm GaInP before nanotexturing, with an absorber doping of 5×10^{16} cm^{-3}. The material is initially grown with a 50 nm GaAs cap layer, which is usually removed through a selective wet etch. The material stack is depicted in Fig. 42. In an analysis of the TRPL of four heterostructure different absorber thicknesses, the surface recombination material has been assessed to be 224 cm/s and the bulk lifetime 264 ns. That analysis is not presented in this document, but it is very similar to the analysis in Section 5.II.B.

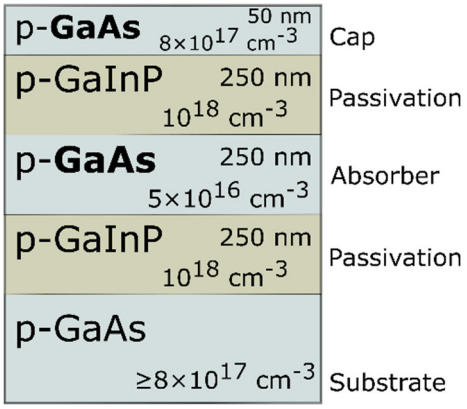

Fig. 42. Material stack for TRPL sample in the nanotexturing study, depicted for the thinnest GaAs absorber of 250 nm. For the baseline nanotexturing process, the GaAs capping layer is removed.

The TRPL decay curves for the 250 nm GaAs absorber are shown below for various etching conditions. While the GaInP passivation layer is etched with a dry plasma etch (using a Cl_2/Ar gas with a 140 W ICP source power and a 70 W platen bias power, as detailed in Section 3.IV), the GaAs cap layer is etched with a selective wet etching to

provide a pristine GaInP layer for the nanotexturing process. (A GaAs cap layer would also be removed in a photovoltaic device to reduce parasitic absorption of the GaAs absorber). The etch solution that removes the GaAs cap is a 100:100:2 proportion of H_2O:H_2O_2:NH_4OH, and it is not expected to etch or otherwise damage the bulk GaInP material.

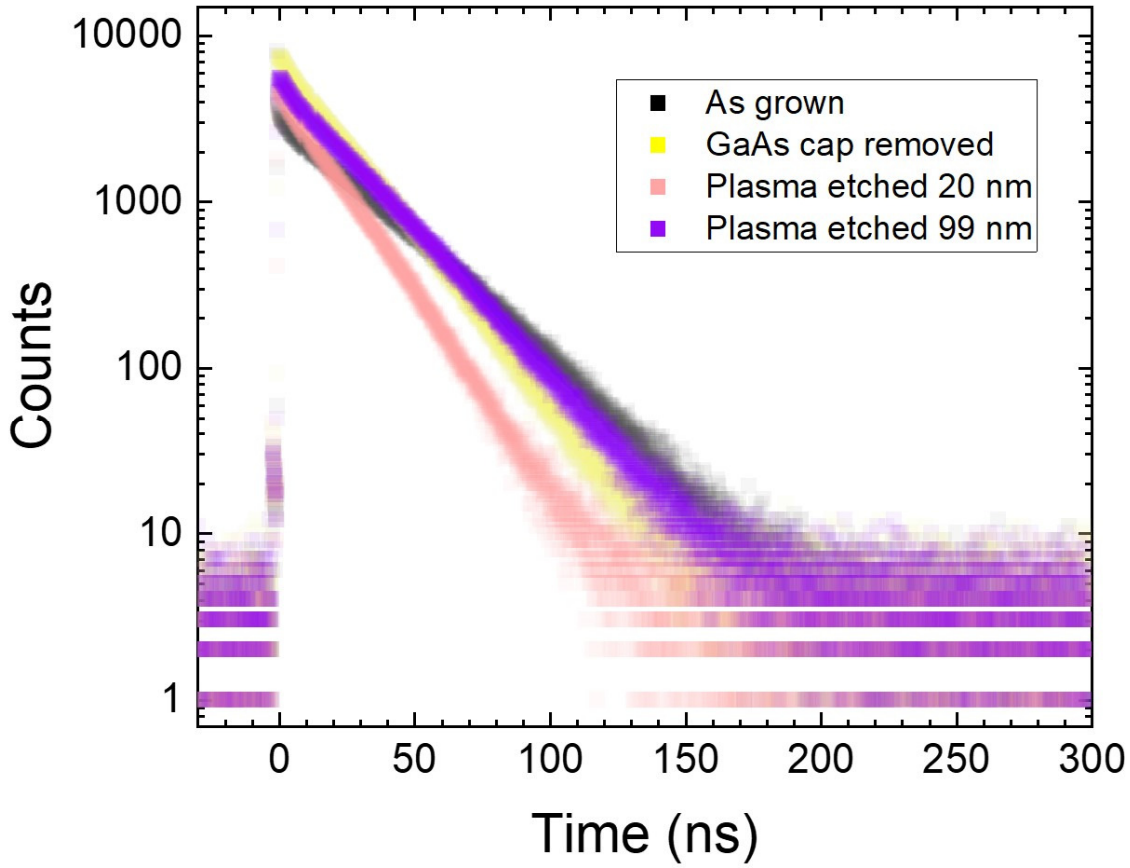

Fig. 43. TRPL lifetime of 250 nm GaAs absorber with 250 nm GaInP passivation layers under a 9 pJ laser pulse with a 39 µm beam diameter. A 50 nm GaAs cap layer is completely removed with wet selective etching in three of the samples (- all but the as-grown sample), while the passivation layer is partially removed with dry plasma etching in two of the samples.

Table 7
LIFETIME (IN NS) WITH WET AND DRY ETCHING

As grown	Cap removed	Cap removed, then plasma etched 20 nm	Cap removed, then plasma etched 99 nm
29.9 ± 0.9	20.5±0.5	17.0±1.0	24.3±0.6

Extracted effective minority-carrier lifetime of the TRPL curves above. The GaAs cap is 50 nm. The GaInP passivation layer is 250 nm thick before plasma etching. The GaAs absorber is 250 nm.

The sample with a cap appears biexponential with a short lifetime associated with recombination in the unpassivated GaAs cap and a longer lifetime associated with the passivated GaAs absorber. The impact of the cap layer is seen to reduce the overall luminescence (due to parasitic absorption of incident light by the unpassivated GaAs cap) but increase the effective lifetime. The cap layer can yield higher lifetimes when it shields the charge dynamics in the passivation and absorber layers from defects at the semiconductor-air interface [161]. The table above compares the lifetime of a sample with a cap layer to samples without a cap layer with various levels of plasma etching. The lifetimes were extracted with a monoexponential fit over the data segment where the signal is both monoexponential and significantly above the noise, from 18 ns to 140 ns. In this regime, the cap layer has the highest lifetime of 29.9 ns.

The order of the greatest lifetime values is somewhat unexpected: the uncapped sample without plasma etching has a lifetime between that of the two uncapped samples with plasma etching. In fact, the uncapped sample with the highest lifetime is the sample that underwent the deepest plasma etching of 99 nm ± 10 nm. These results imply that the plasma etching does not necessarily reduce the material lifetime – as long as the passivation layer is kept sufficiently thick and highly doped.

Note: The samples of Figure 43 and Table 7 above were etched at the Arizona State University plasma etcher using an STS AGE ICP system, while all other plasma etching was done at the University of Ottawa using a SAMCO RIE-110iP ICP system. Although the plasma conditions, as specified in Section 3.IV, were kept the same between the tools (except that the STS system need to run with a chamber pressure twice as high), the etch rate in the STS system in Arizona was about three times slower than the etch rate in the SAMCO system in Ottawa.

A nanostructured sample was made under the high plasma power conditions at the University of Ottawa plasma etcher, but the etched regions between the nanostructures pierced through the passivation layer. Since the absorber became unpassivated, the lifetime was reduced from around 40 ns to 1 ns. After that finding, the default plasma power was reduced in order to achieve a slower etch rate so as not to etch through the passivation layer. The plasma power is henceforth reduced with the ICP source power dropped from 140 W to 65 W and the platen bias power brought from 70 W to 25 W.

The reduction in plasma etching power led to a change in the nanostructure shape, height, as well as lifetime. With a higher plasma power, the nanostructures were seen to be nanodomes, or more precisely semi-ellipsoids, as seen in the SEM images of Figure 41. For the lower plasma power recipe, preliminary SEM images indicate the shapes to be truncated nanocones, with a relatively wide, flat top plateau. The sidewall angle was 55° ± 5°, and the outer diameter was 620 nm ± 18 nm. The AFM results indicate that the height of the nanocones is 149 nm on average, which is about half of the height of the semi-ellipsoids that were made with the higher plasma power, even though the etch time for both recipes was 65 seconds.

With the lower plasma power, the etch depth was adjusted so nanostructures arrays with high lifetimes were fabricated and characterized. The TRPL curves are given in the figure below. As the processed nanostructured area is small (typically 250-µm wide) they require focusing the beam diameter down. They beam is focused down to 39 µm, with further details given in Section 3.II. With such a narrow beam, the TRPL curves can become multiexponential even at a laser pulse of 440 pJ (corresponding to a 0.277 mW time-averaged laser power), because the carrier concentration goes into high-level injection with a focused pulse.

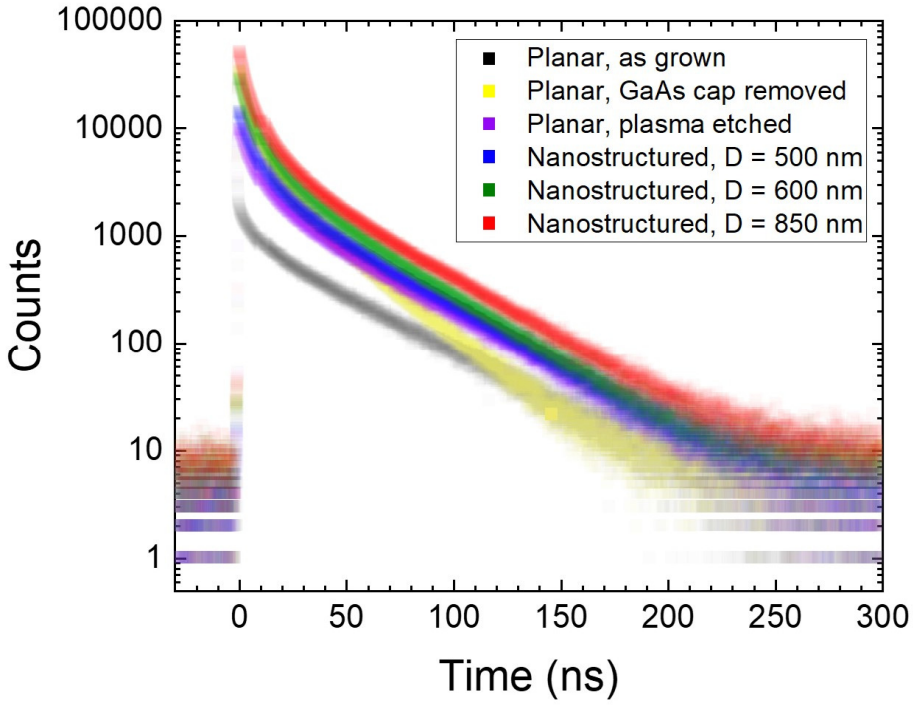

Fig. 44. Effect of etching and nanotexturing on the TRPL of a 250 nm GaAs absorber under a 440 pJ laser pulse. The new plasma recipe uses a lower 25 W platen bias power.

Table 8
LIFETIME (IN NS) WITH WET AND DRY ETCHING

Planar, as grown	Planar, GaAs cap removed	Planar, plasma etched	Nanostructured, D = 500 nm	Nanostructured, D = 600 nm	Nanostructured, D = 850 nm
38.5 ± 2.2	26.2 ± 0.8	38.1 ± 0.7	36.3 ± 0.7	34.4 ± 0.4	36.4 ± 0.3

Extracted effective minority-carrier lifetime of samples of the figure above. The GaInP absorber is 250 nm thick as grown.

It is challenging to visually compare the slopes of the curves as they partially cover each other, but the table above gives the extracted effective lifetimes of each curve. The lifetime was extracted for times from 60 to 215 ns, which is when the curves show monoexponential decay with significant signal-to-noise levels. The tabulated results show that plasma etched *and* nanostructured samples yield lifetimes that are as high as the as-grown sample (to within experimental error). It is curious that the lifetime of the sample with cap removal but no passivation removal (column 2) is lower than the samples with the cap removed and the passivation layers partially removed (columns 3-6). Although PL intensity can increase during thinning of passivation/cap layers due to more carriers getting to the absorber, generating higher carrier concentration [50], the lifetime in the monoexponential segment of the TRPL curve is not expected to depend directly on carrier concentration. The lifetime could, nonetheless, depend on the Fermi level. Therefore, intensity- or temperature-dependent TRPL could be used to see if the order of highest lifetimes is variant.

Finally, TRPL for a thicker GaAs absorber thickness of 2800 nm is presented below. The TRPL conditions are again a 440 pJ laser pulse with a 39 μm beam diameter. Due to the longer lifetime of a thicker absorber the decay occurs over a longer time, so the multiexponential part of the curve can be taken into account with a biexponential fit, as shown. For the long-lifetime component of the biexponential decay, the extracted effective lifetimes of the three materials are quite similar, with 175 ns for the nanostructured material, 188 ns for the planar etched material, and 171 ns for the as-grown material. The differences between these numbers are not significant, as the order of highest lifetime values will change if the weighting scheme used in the OriginPro

fitting algorithm is changed. The weighting scheme used was "statistical, $w_i = 1/y_i$," where w_i and y_i are the weight and the value of the ith data point, respectively. In the alternative weighting scheme of "no weighting, $w_i = 1$" the nanostructured material has the highest lifetime, while in the weighting scheme "variance, $w_i = 1/y_i^2$," the nanostructured material has the lowest lifetime of the three. Thus the differences in lifetimes are below the measurement uncertainty.

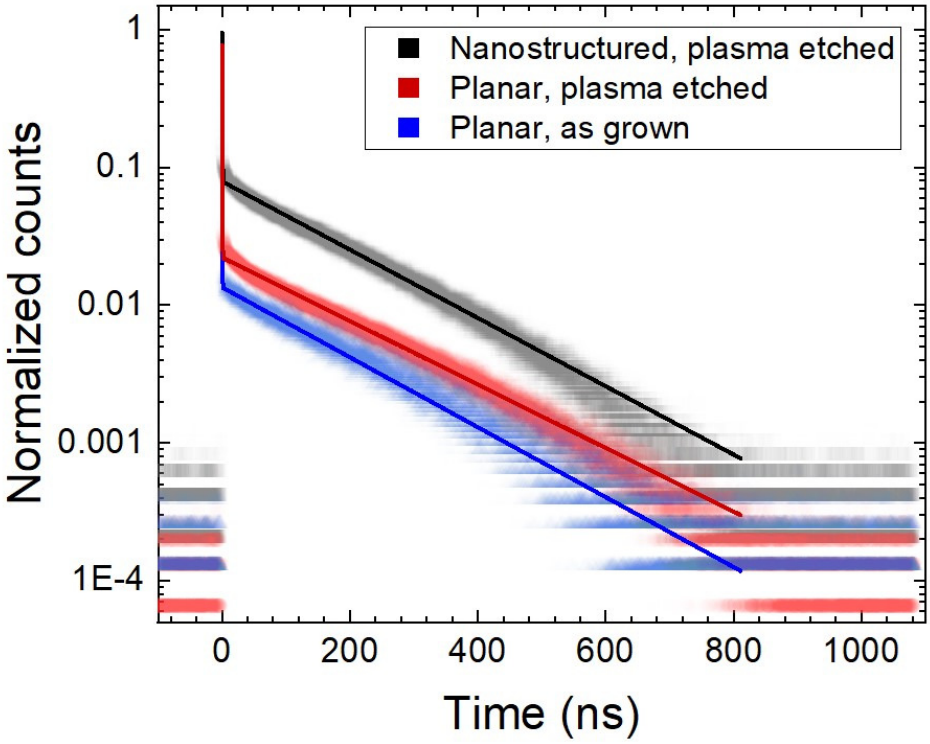

Fig. 45. Effect of etching and nanotexturing on the TRPL of a 2800 nm GaAs absorber. Biexponential fits are shown alongside measured data.

In conclusion, the nanotexturing process did not significantly impact surface passivation after the plasma etched power was reduced. Although the surface area of the GaInP surface was increased, the GaInP layer had a high enough doping (10^{18} cm^{-3}) and thickness (with thickness remaining after etching on the order of 100 nm) that the carriers in the GaAs absorber are effectively passivated from the nanotextured GaInP surface.

CHAPTER 7

WAVELENGTH-SELECTIVE EMISSIVITY

While light trapping can raise module temperatures through reduced sub-bandgap reflection (as seen in the next chapter), it can also lower module temperatures through increased radiative cooling. The enhancement is due to the fundamental equality between absorptivity and emissivity, known as Kirchhoff's law of radiation [31]. Solar irradiance is substantial for wavelengths above 0.3 eV (i.e., below 4.1 μm), whereas thermal irradiance is only significant for wavelengths below 0.35 eV (i.e., above 3.5 μm). There is little intensity in the overlap between solar and thermal irradiance, thus light trapping in $\lambda < 3.5$ μm is likely to increase module temperatures, whereas light trapping in $\lambda >$ 4.1 μm should reduce temperatures.

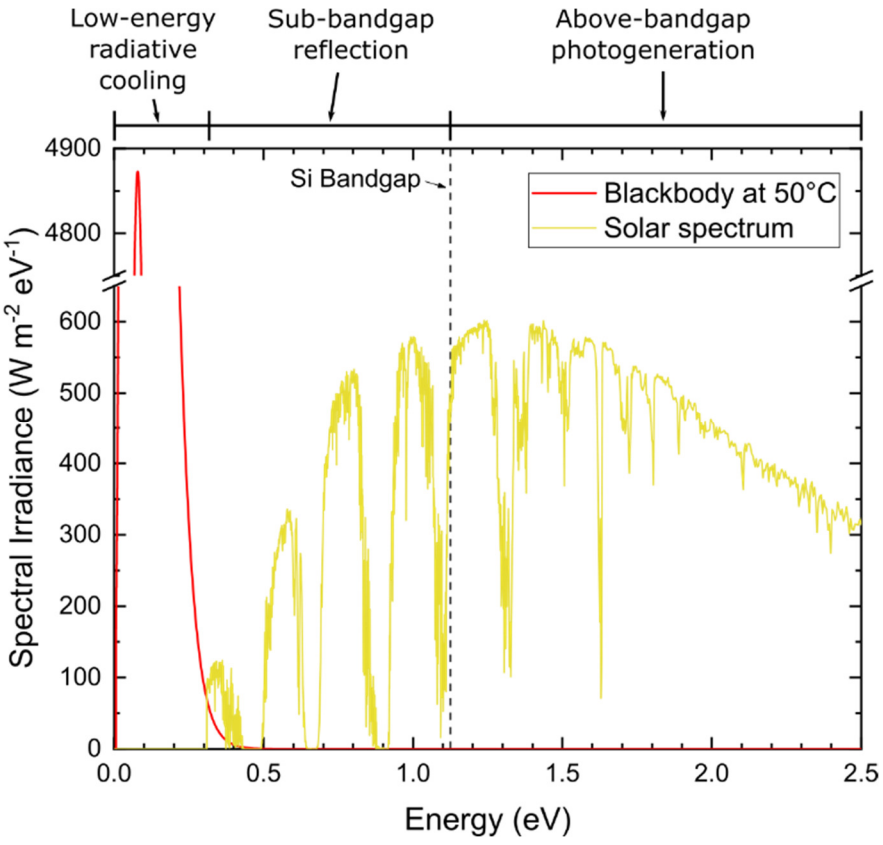

Fig. 46. Spectral regions for different wavelength-selective light trapping techniques.

Light trapping in the mid-infrared region has been shown to increase radiative cooling, as discussed in the literature review of Section 2.VIII. It can be concluded that for PV modules under full sunlight, light trapping – technically light in-coupling – lower module temperatures by increasing bringing emissivity of glass close to 1 for wavelengths over 4.5 μm.

I. Impact of Emissivity Enhancements in and out of the Atmospheric Window on Radiative Cooling and Module Temperature

A more nuanced conclusion, however, can be found if one examines the effects of narrowband enhancements to the emissivity. In particular, we compare the effects of increasing emissivity in the atmospheric window, ϵ_{in}, to increase emissivity outside of the atmospheric window. Now, the wavelength range outside of the atmospheric window, ϵ_{out}, is chosen such that the ϵ_{in} and ϵ_{out} have the same impact on the irradiance-weighted average of emissivity across the full-spectrum. The range inside the window is 8-13 μm. The corresponding range outside of the window with the same amount of blackbody irradiance is 4.581-8 and 12-16.826 μm. Outside of those numbers, the emissivity is held at 0, as seen in Fig. 47.

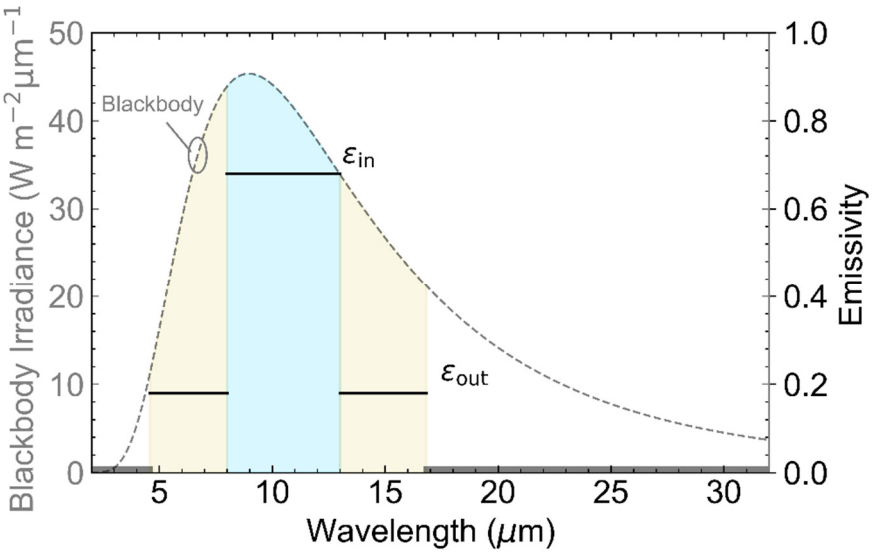

Fig. 47. Wavelength ranges of the two emissivity values that are varied in the simulations, such that the amount of blackbody irradiance added in the two regions out of the atmospheric window (AW) equals the blackbody irradiance within the AW.

Module temperatures are modeled for an open-rack configuration under one sun with a convection coefficient of 17 (W m^{-2} K^{-1}) and ambient and ground temperatures of 25°C. The module considered is a glass-glass single-junction perovskite with a full-spectrum absorptance of 62%, a standard testing condition (STC) efficiency of 20%, and a power-temperature coefficient of -0.14%°C. As the absorptance of the perovskite is low, similar to that of the GaAs, the effect of radiative cooling on temperature here will actually be lower than for a Si module, which generally faces higher heat generation.

Figure 48a shows that emissivity values in the atmospheric window are most effective at reducing module temperatures. The module temperature increases more rapidly with the emissivity in the window, ϵ_{in}, than with the emissivity out of the window, ϵ_{out}. The reason for this difference is explored in Figure 49.

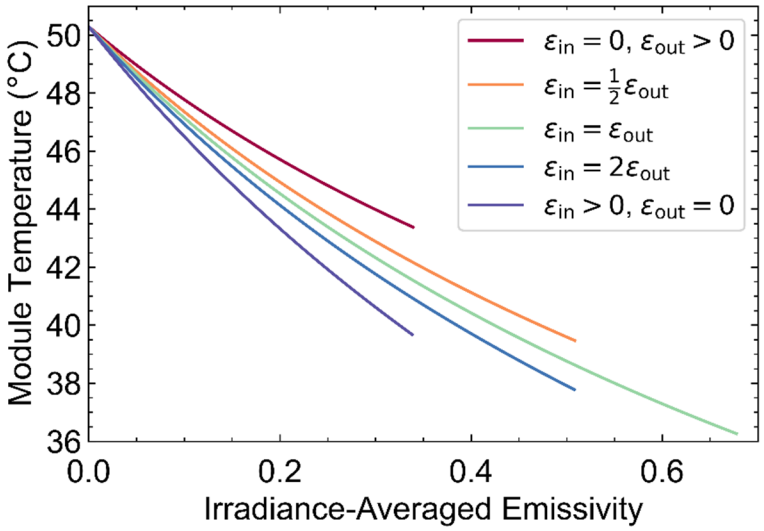

Fig. 48. Impact of increased emissivity on perovskite module temperature, when the emissivity is varied within the atmospheric window, ϵ_{in}, as opposed the emissivity out of the window, ϵ_{out}.

In Figure 49a, we see that increases in ϵ_{in} and ϵ_{out} both lead to similar increases in thermal emission, but increases in ϵ_{in} leads to significantly large increases in net radiative cooling, defined as the difference between emitted and absorbed longwave radiation. Increases in ϵ_{out} are less significant to module temperature, because outside of the atmospheric window there is more thermal downwelling atmospheric radiation that can heat the module. Outside of the window, the cooling achieved with increased emission is counterbalanced by larger absorption of downwelling thermal atmospheric radiation. Thus, increasing the emissivity outside of the atmospheric window raises both thermal emission and absorption, whereas increasing the emissivity inside of the atmospheric window leads to increases in thermal emission with smaller changes in thermal absorption. In conclusion, emissivity values inside of the atmospheric window have a stronger importance on net irradiance than values outside of the window, even after normalizing by the blackbody spectrum.

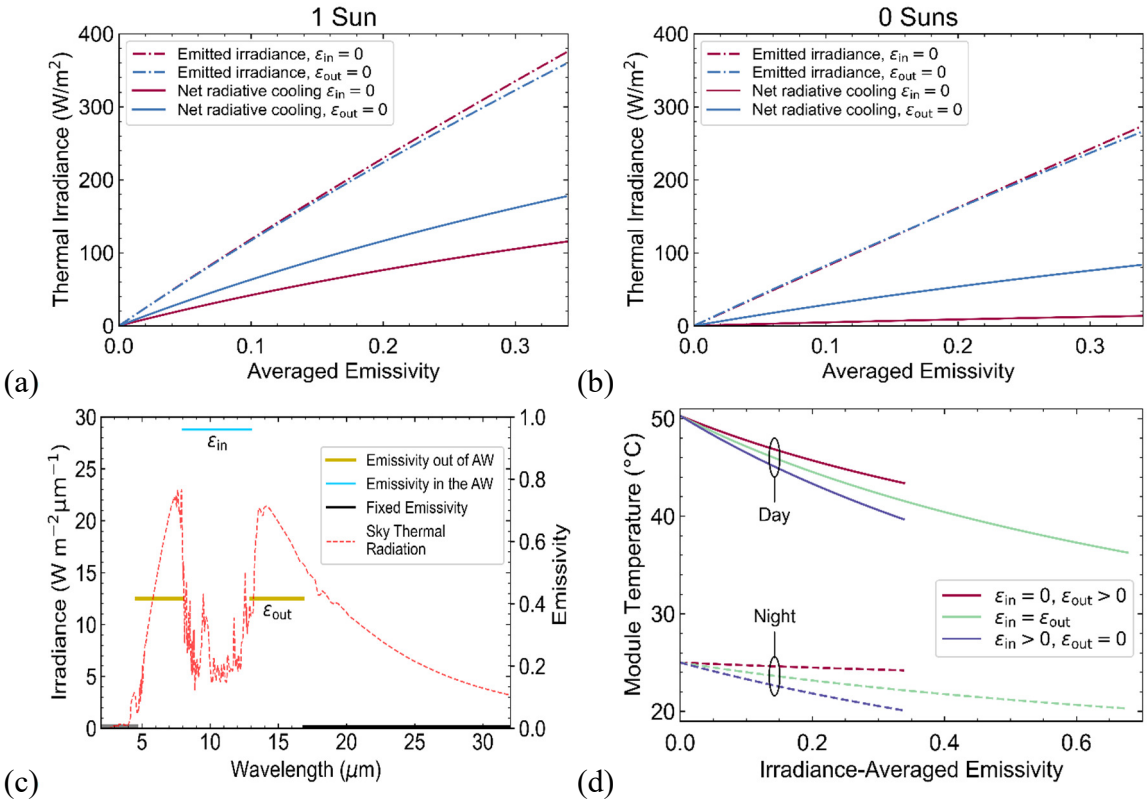

Fig. 49. (a) Reason for the wavelength-sensitive characteristic of increased emissivity on perovskite module temperature. When the emissivity is varied within the atmospheric window, ϵ_{in}, as opposed the emissivity out of the window, ϵ_{out}, the net thermal irradiance out of the cell is higher, leading to greater radiative cooling. (b) The proportional differences in radiative cooling become even greater. (c) The difference between net and emitted irradiance is understood to by the sky thermal irradiance. A greater proportion of this downwelling atmospheric is outside than inside of the atmospheric window. (d) Impact of emissivity and net thermal irradiance on module temperature for 0 suns vs 1 sun.

This phenomenon could inform future optimization to how to weight the values of the emissivity inside the atmospheric window over the values outside of the atmospheric window. Furthermore, if light trapping made in the glass can be focused on increasing the emissivity within the atmospheric window, then higher emissivity values in that range can be achieved. Thus, wavelength-selective light trapping can be used to increase radiative cooling by enhancing thermal emission in the atmospheric window.

The differences between daytime and nighttime cooling are examined in Figures 49 (b) and (d). The environmental conditions, such as ambient temperature, are identical between Figure 49(a) and (b) except for the incident sunlight. In Figure 49(b), the incident solar irradiance is 0 suns, indicating nighttime or deep shadow. At night, increases in emissivity within the atmospheric window is seen to have an even more drastic impact on net longwave radiation increases outside of the window. At night, the thermal balance of a material has an even higher dependence on the longwave thermal radiation received from the atmosphere, as the influence of solar radiation is gone. The near-zero nighttime temperature change for increased ϵ_{out} seen in Figure 49(d) shows how the emissivity inside of the atmospheric window can be essential to reductions in module temperature.

The previous charts considered the emissivity increases with the baseline emissivity considered at 0, but the baseline emissivity of glass as already high at 0.89 [76]. Thus, it can be more realistic to consider a decrease in the emissivity from a baseline value of 1. In other words, values of ϵ_{out} and ϵ_{in} start at 1 and the fixed emissivity of the wavelengths above 16.826 μm are now set at 1 instead of 0. The updated results are given in the figure below, modeled for a glass-glass module with passivated emitter rear contact (PERC) cell of 20% standard testing condition efficiency and a temperature coefficient of -0.35% in power per degree Celsius. It is seen that drops in ϵ_{in} are 60-65% more consequential than drops in ϵ_{out}, for the PERC Si module modeled under one sun. These results elucidate how future study should consider a weighted optimization of the emissivity across the infrared spectrum.

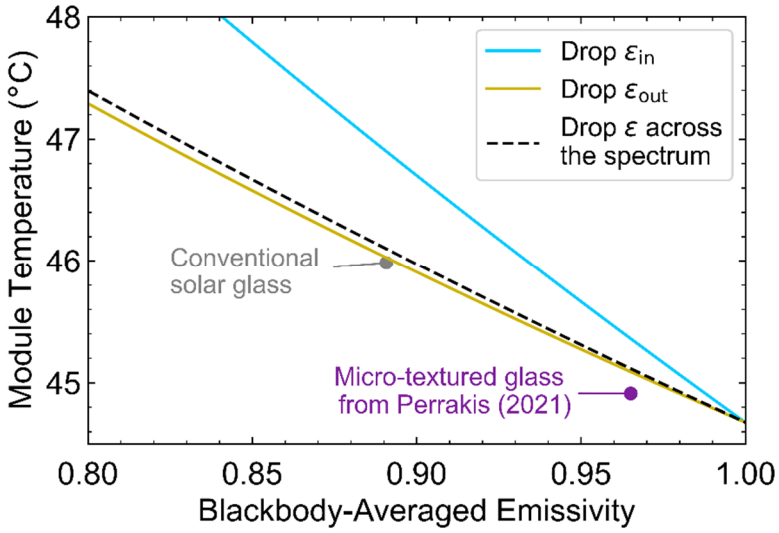

Fig. 50. Impact of drops in the emissivity of a PERC Si module, considering with a baseline emissivity of 1. When the emissivity is reduced within the atmospheric window, ϵ_{in}, as opposed the emissivity out of the window, ϵ_{out}, a 60-65% greater change in the temperature is incurred.

Not only could increasing emissivity in the atmospheric window led to lower module temperatures, but it can also lead to lower environmental temperatures. Much of the thermal emission for wavelengths out of the atmospheric window leads to heating in the atmosphere that will lead to higher temperatures in the local environment. In contrast, much of the emission for wavelengths *in* the window escapes the atmosphere, leading to relatively lower temperatures for the local environment. If PV modules receive a significant portion of the Earth's surface, enhanced emissivity in the atmospheric window could lead to *lower global temperatures*. Thus, advanced photovoltaics could mitigate climate change through targeted radiative cooling in addition to enhanced sub-bandgap reflection, adding to the reduction in greenhouse gases received when replacing fossil fuels with photovoltaics.

Finally, the performance of an ideal emissivity can be benchmarked to the emissivity of conventional cover glass within Figure 50. The module temperature with an ideal emissivity of 1 (but 0 for wavelengths below 4.5 μm as to not incur absorption of

sunlight) is 44.6°C. That temperature can be compared to the 67.8°C value (not shown) for a module with emissivity of 0. The temperature of an open-rack glass-glass module with conventional, flat soda-lime glass, which achieves a temperature of 46.0°C, which corresponds to 94.2% of the potential change with emissivity varied from 0 to 1. Thus, the radiative cooling gains can largely be satisfied by the presence of cover glass. Even more impressive, however, is the nano-textured cover glass of Perrakis et al. [76], which achieves 98.8% of the potential radiative cooling gains for a photovoltaic module under one sun.

In summary, a photovoltaic module under full sunlight experiences the lowest temperatures when its emissivity is 1 for wavelengths above 4.5 μm. Emissivity values in the atmospheric window are 60-65% more impactful than emissivity values outside of the atmospheric window when considering reductions below a baseline emissivity of 1 for a 20% efficient PERC Si module under full sunlight and typical convection conditions. The impact of wavelength-selective emissivity is more pronounced at times when the incident sunlight irradiance is low, thus future work may look to investigate the wavelength-selective design that optimizes the annual temperatures to limit degradation of the module that occurs both when incident solar irradiance is high *and* times where it is low. For photovoltaics under one sun, however, 94% of the potential benefits of radiative cooling are achieved by the presence of a cover glass – a value increased to 99% if micro-textured glass is used.

The next section investigates another form of passive cooling, sub-bandgap reflection, which shows values far below ideal, even for state-of-the-art Si modules.

CHAPTER 8

IMPACT OF LIGHT TRAPPING ON SUB-BANDGAP REFLECTION

This chapter gives the results from my paper published in the journal *IEEE Journal of Photovoltaics,* Ref. [91].

Abstract—Reflection of sub-bandgap light has been argued to be the most effective path to lower-temperature solar modules. This report compares GaAs modules with high sub-bandgap reflection to various Si modules under two experimental thermal configurations. The GaAs modules operate 6°C colder than both polycrystalline and monocrystalline Si within an open-rack configuration. This thermal advantage increases to 13°C for an insulated configuration. The experimental data is used to build a theoretical model, finding agreement with root-mean-square (RMS) error between 1.5-2.8°C. The model shows the main thermal advantage of these GaAs modules to be their high sub-bandgap reflection of 77%. Next, the potential for enhancing silicon's sub-bandgap reflection is considered. It is found that Si modules fundamentally cannot achieve such high sub-bandgap reflection, because of the amplification of parasitic absorption that occurs with light trapping. Light trapping more than doubles the parasitic absorption of encapsulation layers, limiting the Si's maximum sub-bandgap reflection to 63%. Hence, higher values require thorough optimization of front, bulk, and rear layers, but could lower temperatures by up to 11.6°C for insulated Si modules. Enhanced sub-bandgap reflection thus offers an elusive yet effective improvement for solar energy.

Sub-bandgap reflection has been argued as a particularly effective way to lower module temperatures [86],[162],[163],[164]. These reports have focused on open-rack configurations. The current report evaluates the impact of sub-bandgap reflection across thermal configurations. Section I compares module temperature and efficiency between insulated and open-rack configurations. Then, Section III examines the fundamental limitations and practical benefits of sub-bandgap reflection for silicon modules.

I. Effect of Thermal Configurations

Before using the model for explanatory results, it is assessed by comparing calculated and measured temperatures. The curves match quite well as seen in Fig. 51 for a representative summer day. Calculations match measurements with RMS errors within 2.8°C for each module in the open rack configuration. RMS error reduces to 1.5°C for insulated GaAs modules. GaAs's thermal advantage can also be seen in Fig. 51. GaAs operates up to 8.2°C colder than Si in the open-rack configuration compared to 16.9°C colder in the insulated configuration. One may expect the temperature difference to be larger in the insulated configuration as temperatures are magnified by lower cooling.

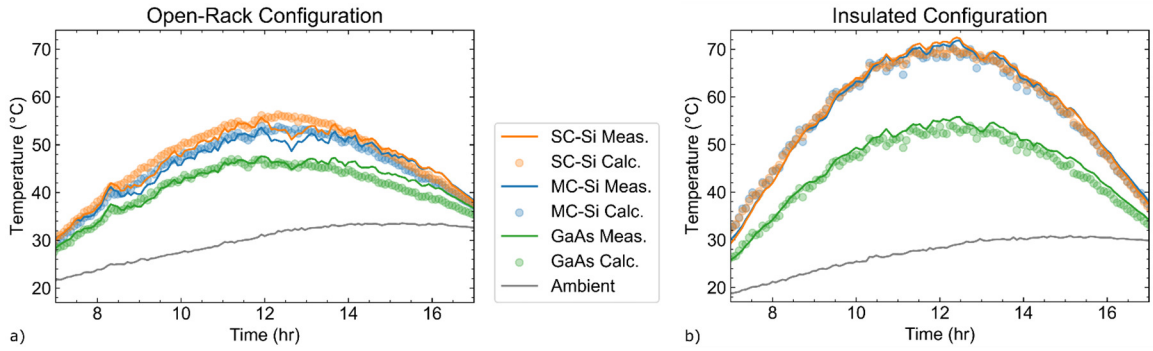

Fig. 51. Hourly temperatures for the (a) open-rack and the (b) insulated configurations for two days during mid-summer in Merced, CA. In the insulated configuration, the Si module temperatures are seen to be much greater than those of GaAs. Calculations match measured values within an RMS error of 1.5-2.8°C for each module over multiple months.

Fig. 52 compares the increase of module temperatures above ambient, ΔT, for Si and GaAs modules across several months of data. The ratio $\Delta T_{Si}/\Delta T_{GaAs}$ is greater in the insulated configuration. In the insulated configuration $\Delta T_{Si}/\Delta T_{GaAs}$ stays near 1.4, while the open-rack ratio varies from 0.9 to 1.3. This variation in the ratio is partly due to movement of the rack's shadow; when the rack shadows the ground beneath the module, the module receives less radiative heat from the ground. Another reason for the varying ratio is nonlinearity in the radiation terms – as seen in Fig. 53.

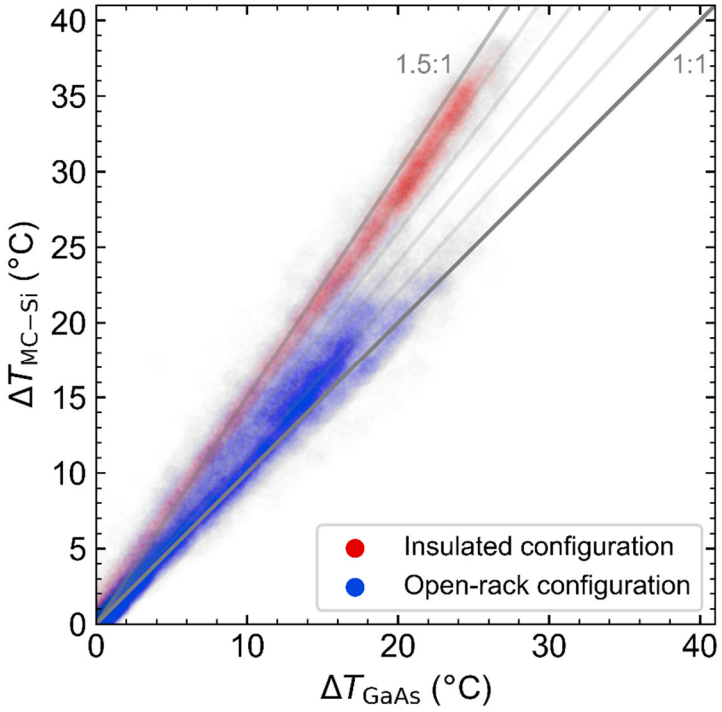

Fig. 52. Comparison of measured ΔT (module temperature above ambient) over several months. The ratio of ΔT is nearly fixed in the insulated configuration, but this ratio varies in the open-rack configuration due to effects of shadows and nonlinearities on radiative cooling.

Fig. 53 depicts the thermal balance graphically for MC-Si and GaAs (with modules graphed on one plot by using only convection coefficients of GaAs1 and neglecting variation in extraction efficiency.) The balance of the heating load with cooling determines the module temperature. The heating load is reduced by reflection and

electrical extraction. The resultant heat load of GaAs is much lower than that of Si primarily due to higher reflection and secondarily to greater extraction. Comparison of a) and b) shows that the cooling effect of sub-bandgap reflection becomes magnified in the insulated configuration. In the open-rack configuration, both modules run cooler due to rear convection and rear radiation.

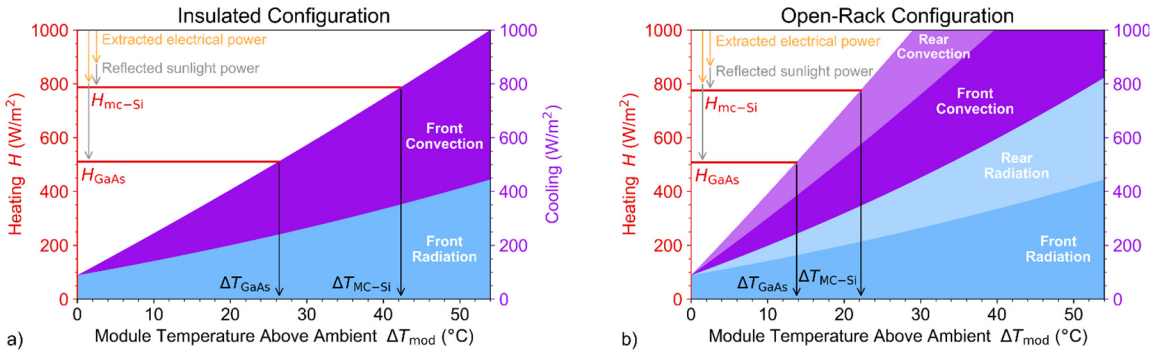

Fig. 53. Depiction of thermal balance for modules in a) the insulated configuration and b) the open-rack configuration. The data are calculated for 1000 W/m^2 irradiance, 1.9 m/s wind speed, as well as 25°C ambient and ground temperatures. GaAs modules are seen to run colder primarily through higher sub-bandgap reflectance. The impact of sub-bandgap reflection leads to much greater temperature differences in the insulated configuration.

Fig. 54 presents a statistical summary for the experimental results, giving averages and standard deviations for module temperature and relative efficiency. To isolate from changes in the weather, the data have been filtered for irradiances between 900-1050 W/m^2, wind speeds 0.5-1.5 m/s, and ambient temperatures 25-35°C. Fig. 54a shows that GaAs modules run significantly cooler than Si - especially in the insulated configuration. The temperature difference between silicon modules is within the standard deviation. The impact on relative efficiency is given in Fig. 54b. The Si modules operate much more efficiently in the cooler configuration, but the GaAs performance appears independent of configuration. This result demonstrates extra power in using GaAs for insulated applications.

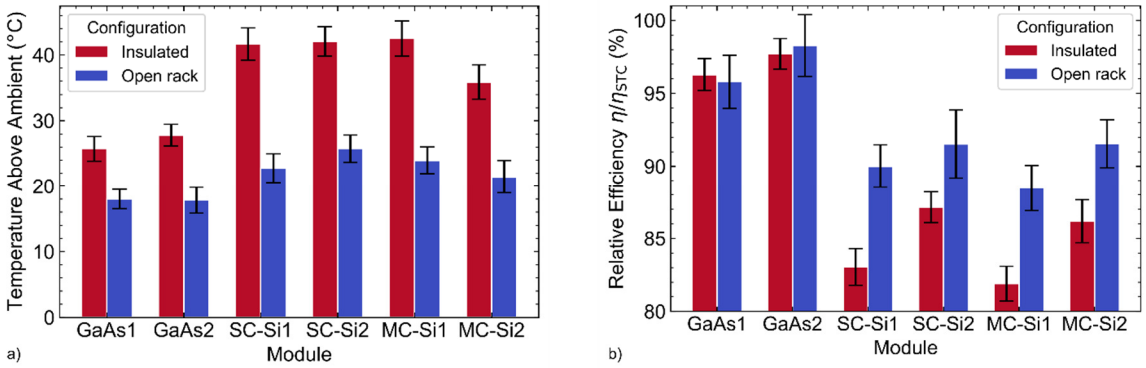

Fig. 54. Experimental (a) module temperature and (b) relative efficiency (relative to STC efficiency) of GaAs, multi-crystalline Si, and single-crystalline Si. The data are filtered for weather around 30°C ambient and 1000 W/m^2 irradiance. The insulated configuration creates hotter temperatures for all modules. The silicon efficiencies are greater in the open-rack than insulated configuration, but the GaAs efficiencies are practically independent of thermal configuration.

The experiments were in Merced, CA – a relatively warm locale. The model is used to extrapolate results to various cities, with results given in Fig. 55. The performance losses due to temperature are nearly three times as large in Phoenix, AZ as in Fargo, ND. Although weather conditions such as irradiance, wind speed, and humidity are considered, the ambient temperatures largely determine the performance loss of hot modules. Error bars here indicate the difference between temperature coefficients found from indoor and outdoor measurements [127]. Although the MC-Si and SC-Si modules operate at similar temperatures, the MC-Si are expected to receive a greater performance loss due to a steeper temperature coefficient. In insulated configurations, the MC modules can lose 16% of their efficiency relative to STC. These results motivate redesigning Si modules to operate at cooler temperatures for insulated configurations.

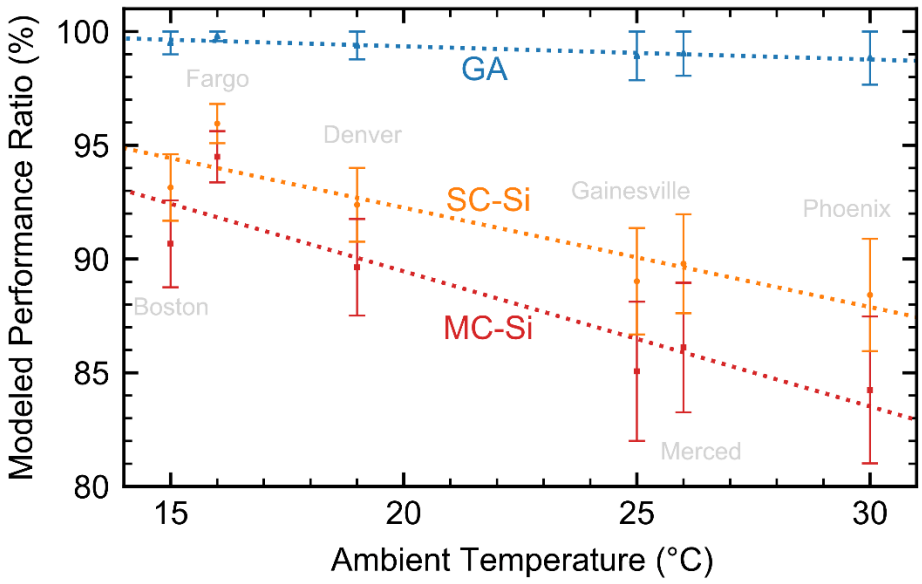

Fig. 55. Irradiance-weighted module-level performance ratio showing the effect of climate on insulated modules. The ambient temperature largely determines the modeled performance loss, while wind and humidity introduce some scatter to a linear fit.

II. Enhancement of Sub-Bandgap Reflection

Si modules are textured to achieve light trapping, which drastically impacts reflection. In particular, the angle-averaged internal reflectance is enhanced to $R_{int} = 1 - 1/n_1^2 = 92\%$ after texturing [141]. For planar modules, internal reflection is much smaller: $R_{int} = R_{ext} = 5\%$ as taken from Si's reflection at 2.5 eV in Fig. 10 of the methods section.

Fig. 56 illustrates the difference in internal reflection. Light trapping leads to a $2n_1^2 = 25$ times greater effective path length through the Si layers of a textured module (compared to in a planar module with a rear reflector) [165]. Due to the intermediate indices of the glass and encapsulant, light trapping increases the effective path length through an encapsulation layer from two to 8.9 times its thickness.

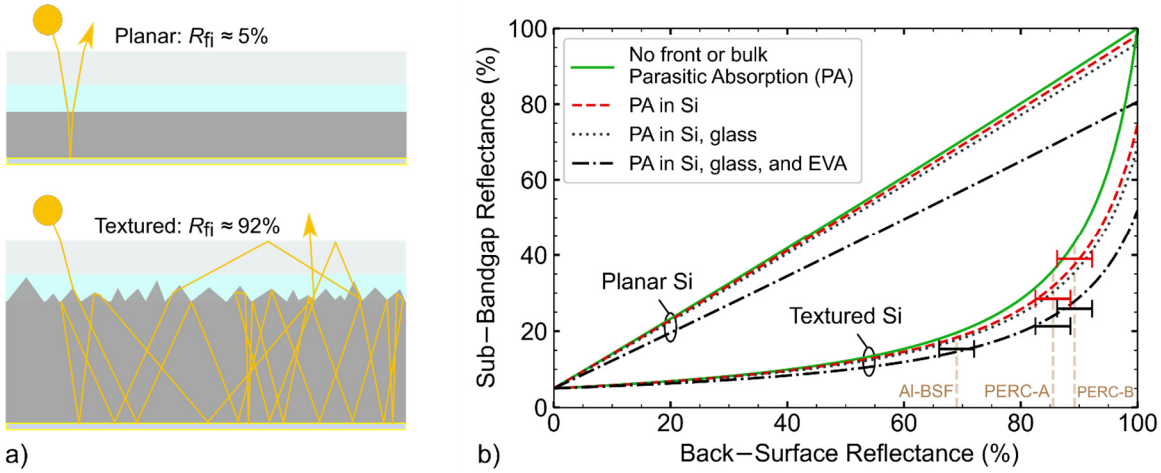

Fig. 56. (a) Illustration of the compounding effect of light trapping on parasitic absorption. Sub-bandgap light in textured cells hits interfaces several times more than in planar cells – sometimes resulting in extra parasitic absorption in encapsulation layers before reflecting at the air interface. (b) Effect on (irradiance-averaged) sub-bandgap reflectance. Textured Si's sub-bandgap reflectance drops precipitously with introduction of parasitic absorption at the front *or* back. Error bars indicate agreement of calculations with experiments from [129].

Thus, light trapping amplifies the effect of parasitic absorption on R_{sub}, leading to the nonlinear curves of Fig. 56b. For textured modules, small deficiencies in back-surface reflection create large drops in sub-bandgap reflection. This sensitivity generalizes to various light-trapping geometries [136], although its magnitude depends on the texturing geometry. In addition to absorption at the rear, textured modules depend more sensitively on PA in bulk and front layers – compare the 80% maximum for planar, encapsulated Si with the 52% maximum for textured, encapsulated Si.

Fig. 56b was calculated with the moderate-doping FCA model to enable comparison of the calculated curves with experimental results from [129]. Indeed, the bare and encapsulated curves here agree with the experimental error bars. The experimental sub-bandgap reflectances were taken from irradiance-weighted averages of bare and encapsulated curves from for Al-BSF, line-contact (PERC-A), and point contact (PERC-B) architectures [129]. The back-surface reflectance values were found from

[166], [167], [168]. The lower reflection for Al-BSF compared to PERC cells can be due to the lack of a rear dielectric layer [169] and the presence of a graded Al-Si layer in the Al-BSF cells [170].

Table 9 gives the maximum sub-bandgap reflection for varying amounts of free-carrier absorption and encapsulation. The table shows moderate FCA to reduce the maximum sub-bandgap reflectance by 25%. This loss, however, can be reduced to 10% in the low-doping case. The impact of glass is seen to be small relative to EVA. The encapsulant EVA drastically limits sub-bandgap reflection. Encapsulation reduces the maximum R_{sub} achievable by 38% absolute.

Table 9
SI SUB-BANDGAP REFLECTANCE AT 100% REAR REFLECTANCE

	Glass & EVA	Glass	Bare
Mid-doping FCA	52.0%	68.8%	74.6%
Low-doping FCA	59.9%	82.5%	89.9%
No FCA	62.5%	91.5%	100.0%

These calculations for textured Si consider parasitic absorption in encapsulation layers and free carrier absorption (FCA) in the Si layers.

For GaAs modules, the sub-bandgap reflection would follow the linear trend of the planar curves in Fig. 56, resulting in less sensitivity to parasitic absorption or rear optical losses. This conclusion is supported by Fig. 10, where the irradiance-averaged R_{sub} for GaAs is 77% compared to PERC's 21%. GaAs modules can fundamentally achieve much higher sub-bandgap reflectances due to the relative insensitivity of planar cells on parasitic absorption.

The thermal impact of enhanced sub-bandgap reflection is determined by

replacing R(E) with $R_{sub}(E)$ for sub-bandgap energies in a recalculation of (1) and (2). Module temperatures (calculated for 1000 W/m^2 irradiance, 25°C ambient, 1 m/s wind speed, and the low-doping FCA model) are given in Fig. 57. These results show a potential 12.8°C reduction from sub-bandgap reflection. This enhancement could significantly improve the end-of-life performance for insulated configurations, because module degradation can increase with temperature [171], [172]. Using a temperature coefficient of -0.37%/°C for SC-Si, the efficiency increase is determined as 4.8% relative to STC – amounting to an efficiency boost of 1.0% absolute.

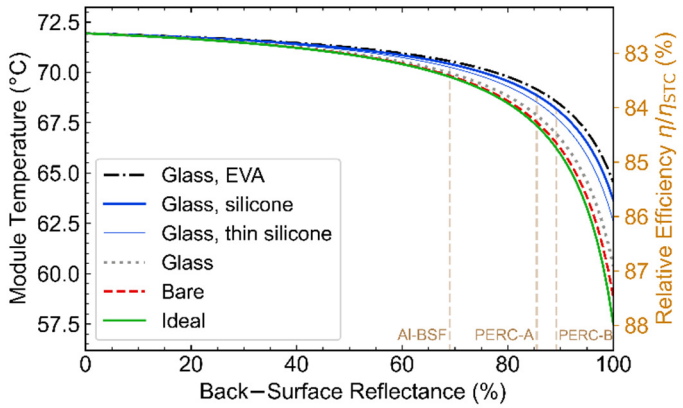

Fig. 57. Cooling due to enhanced reflection of sub-bandgap light for insulated SC-Si modules in 25°C ambient. Parasitic absorption in the encapsulant material severely limits the impact of a higher back-surface reflection.

The ideal curve in Fig. 57 neglects parasitic absorption in front and bulk layers. Although ideal modules can cool by 12.8°C due to enhanced back-surface reflection, this value drops significantly for encapsulated modules. A module with glass and EVA sees 7.4°C cooling if its back-surface reflectance improves to 100%. Replacing EVA with the more expensive encapsulant silicone gives marginal benefits in cooling. Using thinner silicone of 0.2 mm would yield some extra benefits - but thinner encapsulants do leave

modules more vulnerable to stress-induced damage [173]. The thin silicone encapsulant gives a maximum sub-bandgap reflection of 67%, yielding 9.3°C cooling.

Substantially more cooling, 11.6°C, becomes available if PA in the encapsulant could be eliminated. One may consider removing [174] or replacing the encapsulant [175]. A selective filter could be integrated into the glass to reflect sub-bandgap light [86], [176]. The glass itself could be designed as a selective mirror [177], [178]. Perhaps best, a selective filter could be placed between the glass and the encapsulant, which would lower the parasitic absorption that occurs in the encapsulant while preserving radiative emission from the glass [87].

III. Conclusion of sub-bandgap reflection

This chapter compares the value of sub-bandgap reflection across module types and thermal configurations. Multiple configurations were designed to simulate varying thermal scenarios. The Si modules run hotter than the GaAs. The temperature difference was highest in the insulated configuration, where cooling factors are reduced. The performance of Si modules in the insulated configuration dropped by several percent relative to the open-rack configuration, but GaAs preserved its high efficiency. This result demonstrates extra power in using GaAs over Si for thermally-insulated configurations.

This result demonstrates extra power in using GaAs over Si for thermally-insulated configurations. Although GaAs is too expensive for many large-scale applications, its temperature advantage could become a deciding factor for thermally-insulated, high-value applications such as unmanned-aerial vehicles. Lower temperatures

should also yield less module degradation. Future work may consider evaluating the difference in lifespan between GaAs and Si modules within thermally insulated configurations.

A computational model was validated with RMS errors within 1.5-2.8°C. This model explains that the temperature difference derives primarily from GaAs's higher sub-bandgap reflection and secondarily from its higher V_{OC}. These GaAs modules reflect 77% of sub-bandgap photons, which reduces excess heat. This sub-bandgap reflection dwarfs that of the Si modules – at 21% for the single-crystalline modules and 15% for the multi-crystalline modules.

Enhancing the sub-bandgap reflection of Si could return a quarter of its temperature-induced performance loss – but only if the front, bulk, and rear are all highly optimized. Ray tracing shows light trapping to amplify parasitic absorption, which fundamentally limits sub-bandgap reflection in textured Si modules compared to thin films. Parasitic absorption within the EVA layer nearly halves the potential benefits of sub-bandgap reflection. Alternative materials for the encapsulant can give marginal improvements - but eliminating parasitic absorption in the encapsulant through advanced designs enables greater benefits. Only then could textured Si achieve the sub-bandgap reflection demonstrated by planar GaAs.

CHAPTER 9

OVERVIEW AND CONCLUSION

In this work, light trapping in thin photovoltaic (PV) cells is examined over the electromagnetic spectrum.

First, the influence of light trapping for the absorption of above-bandgap light is detailed. It is shown that an enhancement of a rear mirror always benefits a monofacial cell, but negative consequences can occur as a result of light trapping caused by light scattering and internal reflection. Depending on the structures and processes used to implement it, light trapping can increase parasitic absorption, series resistance, or surface recombination velocity. In the absence of those potential negative effects, it is shown that light trapping will improve Si cell performance - even for thick 1000 μm absorber layers, but it only boosts performance in direct-bandgap, thin-film PV cells for particularly thin absorbers. GaAs, for example, can only significantly benefit from light trapping when the absorber thickness is below 2 μm, which could allow for V_{oc} increases through absorber thickness and bulk recombination reduction. At a fixed thickness and current, however, light trapping will decrease V_{oc} by increasing the net radiative recombination in the absorber. The increased radiative recombination was shown to lead to an efficiency loss for some copper indium gallium diselenide (CIGS) cells, depending on thickness, rear reflectance, and carrier lifetime. Nonetheless, it is shown that the net effect of increased absorption and radiative recombination, which are the two fundamental consequences of light trapping, lead to efficiency increases for Si, CdTe, and GaAs regardless of thickness, rear reflectance, and carrier lifetime.

The minority-carrier lifetime has a significant impact on the extent to which light trapping benefits the photovoltaic performance of a material. If the carrier lifetime in a material is relatively low, then many charge carriers will recombine before reaching electrical contacts. By increasing absorption, light trapping allows for a reduction in absorber thickness, reducing the distance to contacts. Thus, light trapping is particularly beneficial for materials with low bulk lifetimes. To investigate this, bulk lifetimes in multiple materials were measured using time-resolved photoluminescence (TRPL). The bulk lifetime was measured at 32 ns ± 5 ns for molecular beam epitaxy (MBE)-grown GaAs, and 100 ns ± 30 ns for metal-organic chemical vapor deposition (MOCVD)-grown GaAs. The surface-recombination velocities were found to be 4100 cm/s ± 800 cm/s at the MBE-grown and 1210 ± 60 cm/s at the MOCVD-grown GaAs/GaInP interface. The superior quality of MOCVD-grown material over the MBE material is consistent with multiple previous studies. Modeling of light trapping effects yielded benefits for both materials, boosting maximum efficiencies by 2% absolute for MBE-grown and 1% absolute for the MOCVD-grown material. For the dilute nitride material $GaN_{0.02}P_{0.98}$, the TRPL signal was detectable only at low temperatures. At 11 K, the SRV was measured to be 730 cm/s ± 130 cm/s and the bulk lifetime at 300 ns ± 400 ns for $GaN_{0.02}P_{0.98}$ passivated by GaP. At room temperature, the bulk lifetime is expected to be much lower, implying that light trapping would become critical for GaNP photovoltaic cell performance under normal operating conditions.

The impact of light trapping and surface recombination was investigated for a type of photovoltaic cell known as a photonic power converter (PPC). PPCs convert monochromatic light into electricity, and as such, can experience significant current gains

from light trapping when the light is near the material bandgap. Device modeling shows an increase in PPC efficiency of 8-16% absolute from the introduction of light trapping on our MBE-grown GaAs material. Optical modeling with the finite-difference time-domain (FDTD) software Lumerical was performed to explore particular light-trapping structures. The current best simulation uses 700-nm wide truncated nanocones and achieves 25x path-length enhancement. A major obstacle to higher light trapping values is the parasitic absorption that occurs in the rear metal layer. Thus, a dielectric layer was integrated in the simulated PV cell between the metal layer and the semiconductor layer. While such a dielectric layer is essential to reaching path-length enhancement over 10×, it complicates fabrication, as it would likely require a patterned dielectric back-contact layer to be developed along with the front nanostructures.

The front nanostructures were experimentally fabricated and then characterized. Fabrication was led by our partners at the University of Ottawa through electron-beam lithography (EBL) followed by plasma etching with Cl_2/Ar. EBL was chosen over self-assembled lithography as the uniformity in nanostructure diameter and spacing was essential to the light trapping enhancement determined by FDTD simulations. Under secondary electron microscopy (SEM), the nanotexturing structures were found to be highly uniform with the shape of semi-ellipsoids. Impact of the nanotexturing was assessed by TRPL. For Cl_2/Ar plasma etching on the order of a 150 nm depth into a 250 nm GaInP passivation layer, the material lifetime did not reduce as a result of the plasma etching or the EBL nanotexturing process. Thus, a nanotextured III-V layer offers absorption enhancement without amplification of recombination, and is particularly

beneficial to narrowband photovoltaics where parasitic absorption in a nanotextured passivation layer can be neglected.

Next, the thermal impact of wavelength-selective light trapping was examined, through the phenomena of both radiative cooling and sub-bandgap reflection. For conventional modules, the glass material's emissivity is the parameter that largely determines the radiative cooling of a material at a given temperature. In this report, influence of the atmospheric window on radiative cooling is quantified. The atmospheric window is defined as 8-13 μm, where the atmosphere is largely transparent to light, and it has a significant influence on the net longwave irradiance of a surface. Greater emittance in this wavelength range can significantly enhance radiative cooling. Here, the impact of increasing the emissivity inside of the atmospheric window was compared to that of a corresponding region outside of the atmospheric window. Compared to an emissivity of 1, a reduction in the emissivity inside of the atmospheric window is modeled to have a 60%-65% higher impact on the module temperature than the emissivity outside of the window. Finally, the radiative cooling of state-of-the-art Si modules is shown to already have 99% of the possible gains achievable for modules in an environment with moderate values of convection. In summary, the investigations show that, while wavelength-selective emissivity has a significant impact on temperature (and thus material longevity), the current state-of-the-art is already quite close to its ideal limit.

The final section showed that for sub-bandgap reflection, in contrast, there is still much room for improvement between the values for modern Si modules and the ideal of 100% reflection. In collaboration with the University of California, Merced, an experimental apparatus was built to compare record-breaking GaAs module designs to

various Si module types. The GaAs modules were seen to operate with several degrees lower temperature than the Si modules, an effect seen in previous work by Silverman [85]. For the modules in the present study however, it was proven that the temperature advantage of GaAs was primarily due to its higher sub-bandgap reflection. Furthermore, was shown that the reason for the superior sub-bandgap reflection of the GaAs modules was primarily the absence of light trapping. Ray-tracing calculations were performed, showing that light trapping amplifies parasitic absorption, reducing the sub-bandgap reflection of an Aluminum back surface field (Al-BSF) Si module from 57% to 15%. For cells with a higher back surface reflection, the sub-bandgap reflectance increases but is limited by the impact of encapsulation layers. Since the encapsulation layer, which is commonly ethylene vinyl acetate (EVA), has an index of refraction between air and the semiconductor, light in a module with textured cells can get trapped and attenuated in the encapsulant, leading to substantial parasitic absorption for photon energies below 1 eV. A textured Si module encapsulated by 3.2 mm glass and 0.4 mm of EVA can achieve a sub-bandgap reflectance of only 63%. For modules with rear thermal insulation, elimination of parasitic absorption in the encapsulant could reduce temperatures by up to 4°C, offering efficiency gains by 1.5% relative to standard testing conditions. Further benefits to PV module levelized cost of electricity (LCOE) can be realized by considering the accelerating effect that higher temperatures have on material degradation.

In conclusion, light trapping should be avoided for sub-bandgap light to increase reflection (lower temperatures), but applied at lower energies of the blackbody spectrum to increase thermal emission (lower temperatures) and at above-bandgap energies to increase photogeneration (higher currents).

There are multiple areas of near-term research that could be productive in the area of wavelength-selective light trapping. One research opportunity is to optimize FDTD simulations for metallic nanospheres in order to create light trapping above the bandgap but not below the bandgap. A similar opportunity is to categorize which light-trapping designs could trap light near the bandgap without trapping sub-bandgap light.

A particularly interesting research possibility is to quantify the thermal effect of light trapping for thin-film materials such as CdTe, CIGS, a-Si, and perovskites. These direct bandgap materials can achieve strong optical absorption without light trapping. By avoiding the heat generation incurred by light trapping, direct bandgap semiconductors become a better fit for applications involving thermal insulation, as in some building-integrated and vehicle-integrated PV applications. That thermal advantage would, however, diminish if the direct bandgap PV cells have light-trapping features or absorptive rear interfaces. Light trapping for these materials is particularly relevant for Si-based tandem cells, where light trapping is conventionally introduced for the indirect-bandgap Si bottom cell. The impact of this light trapping could be critical to the reliability of perovskite top-junctions, which have been seen to decompose at temperatures as low as 60°C [179]. Determination of the effect of light trapping on levelized cost of electricity (LCOE) of perovskite-Si tandems could provide valuable information on whether the long-term production of such tandems would benefit from broadband light trapping – or not [180]. Designs that only give light trapping above a specified energy, such as selective front reflectors or backscattering nanospheres, could allow for the photogeneration benefits of light trapping without incurring increased heat

generation. These investigations could impact the development of perovskite-Si tandems, and the field of photovoltaics at large.

REFERENCES

[1] "A fundamental look at energy reserves for the planet." https://www.researchgate.net/publication/237440187_A_fundamental_look_at_energy_reserves_for_the_planet (accessed Apr. 08, 2021).

[2] Z. Shahan, "Correction: Solar Power Equaled 37% Of New US Power Capacity In 1st Half Of 2020," *CleanTechnica*, Sep. 14, 2020. https://cleantechnica.com/2020/09/14/correction-solar-power-equaled-37-of-new-us-power-capacity-in-1st-half-of-2020/ (accessed Oct. 27, 2021).

[3] N. El-Atab, R. B. Mishra, R. Alshanbari, and M. M. Hussain, "Solar Powered Small Unmanned Aerial Vehicles: A Review," *Energy Technology*, vol. n/a, no. n/a, doi: 10.1002/ente.202100587.

[4] R. Haight, W. Haensch, and D. Friedman, "Solar-powering the Internet of Things," *Science*, vol. 353, no. 6295, pp. 124–125, Jul. 2016, doi: 10.1126/science.aag0476.

[5] W. R. Chan *et al.*, "Toward high-energy-density, high-efficiency, and moderate-temperature chip-scale thermophotovoltaics," *Proceedings of the National Academy of Sciences*, vol. 110, no. 14, pp. 5309–5314, Apr. 2013, doi: 10.1073/pnas.1301004110.

[6] J. D. López-Cardona, C. Vázquez, D. S. Montero, and P. C. Lallana, "Remote Optical Powering Using Fiber Optics in Hazardous Environments," *J. Light. Technol.*, vol. 36, no. 3, pp. 748–754, Feb. 2018, doi: 10.1109/JLT.2017.2776399.

[7] L. Summerer and O. Purcell, "Concepts for wireless energy transmission via laser," *ESA*, p. 10, 2009.

[8] G. Landis, *Laser Power Beaming for Lunar Polar Exploration*. 2020. doi: 10.2514/6.2020-3538.

[9] E. Yablonovitch, "Statistical ray optics," *J. Opt. Soc. Am., JOSA*, vol. 72, no. 7, pp. 899–907, Jul. 1982, doi: 10.1364/JOSA.72.000899.

[10] N. N. Lal, B. W. Schneider, K. N. Le, A. F. Thomson, T. P. White, and K. R. Catchpole, "Wavelength selective light trapping for tandem solar cells on silicon," in *Light, Energy and the Environment (2014), paper PTu3C.4*, Optica Publishing Group, Dec. 2014, p. PTu3C.4. doi: 10.1364/PV.2014.PTu3C.4.

[11] N. N. Lal, T. P. White, and K. R. Catchpole, "Optics and Light Trapping for Tandem Solar Cells on Silicon," *IEEE Journal of Photovoltaics*, vol. 4, no. 6, pp. 1380–1386, Nov. 2014, doi: 10.1109/JPHOTOV.2014.2342491.

[12] C. Yang *et al.*, "Wavelength-Selective Light Trapping with Nanometer-Thick Metallic Coating," *Advanced Photonics Research*, vol. 3, Mar. 2022, doi: 10.1002/adpr.202100338.

[13] P. K. Basu, A. Khanna, and Z. Hameiri, “The effect of front pyramid heights on the efficiency of homogeneously textured inline-diffused screen-printed monocrystalline silicon wafer solar cells,” *Renewable Energy*, vol. 78, pp. 590–598, Jun. 2015, doi: 10.1016/j.renene.2015.01.058.

[14] Y. Li, Z. Li, Y. Zhao, and A. Lennon, “Modelling of Light Trapping in Acidic-Textured Multicrystalline Silicon Wafers,” *International Journal of Photoenergy*, vol. 2012, p. e369101, Feb. 2012, doi: 10.1155/2012/369101.

[15] S. C. Baker-Finch and K. R. McIntosh, “Reflection of normally incident light from silicon solar cells with pyramidal texture,” *Progress in Photovoltaics: Research and Applications*, vol. 19, no. 4, pp. 406–416, 2011, doi: 10.1002/pip.1050.

[16] B. Jacobs and G. De Mey, “Change of the collection efficiency in a pn-solar cell by scattering of the incident light through the junction,” *Solid-State Electronics*, vol. 21, no. 10, pp. 1191–1193, Oct. 1978, doi: 10.1016/0038-1101(78)90364-7.

[17] R. Saive, “Light trapping in thin silicon solar cells: A review on fundamentals and technologies,” *Progress in Photovoltaics: Research and Applications*, vol. 29, no. 10, pp. 1125–1137, 2021, doi: 10.1002/pip.3440.

[18] K. Wijekoon, R. Mishra, M. P. Stewart, T. Weidman, H. Ponnekanti, and T. R. Holtam, “Surface cleaning and texturing process for crystalline solar cells,” US8129212B2, Mar. 06, 2012 Accessed: Apr. 16, 2023. [Online]. Available: https://patents.google.com/patent/US8129212B2/en

[19] D. A. Jenny, J. J. Loferski, and P. Rappaport, “Photovoltaic Effect in GaAs p-n Junctions and Solar Energy Conversion,” *Phys. Rev.*, vol. 101, no. 3, pp. 1208–1209, Feb. 1956, doi: 10.1103/PhysRev.101.1208.

[20] Z. I. Alferov, V. M. Andreev, M. B. Kagan, I. I. Protasov and V. G. Trofim, “Solar-energy converters based on p-n $Al_xGa_{1-x}As$-GaAs heterojunctions,” *Soviet Physics: Semiconductors*, bol. 4, pp. 2047, 1971.

[21] J. M. Woodall and H. J. Hovel, “High-efficiency $Ga_{1-x}Al_xAs$–GaAs solar cells,” p. 4.

[22] R. P. Gale, J. C. C. Fan, G. W. Turner, and R. L. Chapman, A new high-efficiency GaAs solar cell structure using a heterostructure back-surface field. 1984, pp. 1422–1425. Accessed: Oct. 27, 2021. [Online]. Available: https://ui.adsabs.harvard.edu/abs/1984pvsp.conf.1422G

[23] G. J. Bauhuis, P. Mulder, E. J. Haverkamp, J. C. C. M. Huijben, and J. J. Schermer, “26.1% thin-film GaAs solar cell using epitaxial lift-off,” *Solar Energy Materials and Solar Cells*, vol. 93, no. 9, pp. 1488–1491, Sep. 2009, doi: 10.1016/j.solmat.2009.03.027.

[24] M. A. Green, E. D. Dunlop, J. Hohl-Ebinger, M. Yoshita, N. Kopidakis, and A. W. Y. Ho-Baillie, “Solar cell efficiency tables (Version 55),” *Progress in Photovoltaics: Research and Applications*, vol. 28, no. 1, pp. 3–15, 2020, doi: https://doi.org/10.1002/pip.3228.

[25] S. Rühle, “Tabulated values of the Shockley–Queisser limit for single junction solar cells,” *Solar Energy*, vol. 130, pp. 139–147, Jun. 2016, doi: 10.1016/j.solener.2016.02.015.

[26] M. Yamaguchi, *High-Efficiency GaAs-Based Solar Cells*. IntechOpen, 2020. doi: 10.5772/intechopen.94365.

[27] S. Eyderman, A. Deinega, and S. John, “Near perfect solar absorption in ultra-thin-film GaAs photonic crystals,” *J. Mater. Chem. A*, vol. 2, no. 3, pp. 761–769, Dec. 2013, doi: 10.1039/C3TA13655H.

[28] W. Yang *et al.*, “Ultra-thin GaAs single-junction solar cells integrated with a reflective back scattering layer,” *Journal of Applied Physics*, vol. 115, no. 20, p. 203105, May 2014, doi: 10.1063/1.4878156.

[29] H.-L. Chen *et al.*, “A 19.9%-efficient ultrathin solar cell based on a 205-nm-thick GaAs absorber and a silver nanostructured back mirror,” *Nat Energy*, vol. 4, no. 9, pp. 761–767, Sep. 2019, doi: 10.1038/s41560-019-0434-y.

[30] M. van Eerden *et al.*, “A facile light-trapping approach for ultrathin GaAs solar cells using wet chemical etching,” *Progress in Photovoltaics: Research and Applications*, vol. 28, no. 3, pp. 200–209, 2020, doi: 10.1002/pip.3220.

[31] Kirchhoff G. Uber den Zusammenhang zwischen Emission und Absorption von Licht und, *Monatsberichte der Akademie der Wissenschaften zu Berlin,* 1859; 783–787.

[32] Shockley W, Queisser HJ. Detailed Balance Limit of Efficiency of p-n Junction Solar Cells. *J. Appl. Phys.* 1961; **32**: 510–519.

[33] Tiedje T, Yablonovitch E, Cody GD, Brooks BG. Limiting efficiency of silicon solar cells. *IEEE Transactions on Electron Devices* 1984; **31**: 711–716.

[34] Miller OD, Yablonovitch E, Kurtz SR. Strong Internal and External Luminescence as Solar Cells Approach the Shockley–Queisser Limit. *IEEE Journal of Photovoltaics* 2012; **2**: 303–311.

[35] Lasher G, Stern F. Spontaneous and Stimulated Recombination Radiation in Semiconductors. *Phys. Rev.* 1964; **133**: A553–A563.

[36] Wurfel P. The chemical potential of radiation. *J. Phys. C: Solid State Phys.* 1982; **15**: 3967–3985.

[37] Trupke T, Green MA, Würfel P, Altermatt PP, Wang A, Zhao J, Corkish R. Temperature dependence of the radiative recombination coefficient of intrinsic crystalline silicon. *J. Appl. Phys.* 2003; **94**: 4930.

[38] Shockley, W. and Queisser, H. J., "Detailed Balance Limit of Efficiency of p-n Junction Solar Cells," J. Appl. Phys 32(3), 510–519 (1961).

[39] Feldman, D. and Margolis, R., "Q4 2018 / Q1 2019 Solar Industry Update," PR-6A20-73992, NREL, 74 (2019).

[40] Green, M. A., Hishikawa, Y., Dunlop, E. D., Levi, D. H., Hohl-Ebinger, J., Yoshita, M. and Ho-Baillie, A. W. Y., "Solar cell efficiency tables (Version 53)," *Prog. Photovolt.* 27(1), 3–12 (2019).

[41] Yablonovitch, E., "Statistical ray optics," J. Opt. Soc. Am., JOSA 72(7), 899–907 (1982).

[42] Han, S. E. and Chen, G., "Toward the Lambertian Limit of Light Trapping in Thin Nanostructured Silicon Solar Cells," Nano Lett. 10(11), 4692–4696 (2010).

[43] Yu, Z., Raman, A. and Fan, S., "Fundamental limit of nanophotonic light trapping in solar cells," PNAS 107(41), 17491–17496 (2010).

[44] Ghannam, M. Y., Abouelsaood, A. A. and Mertens, R. P., "Refined modeling of optical confinement in thin silicon layers with a Lambertian back reflector for solar cell applications," J. Appl. Phys 84(1), 496–502 (1998).

[45] Disney, C. E. R., Pillai, S., Johnson, C. M. and Green, M. A., "Self-Assembled Nanostructured Rear Reflector Designs for Thin-Film Solar Cells," ACS Photonics 2(8), 1108–1116 (2015).

[46] Kioupakis, E., Yan, Q., Steiauf, D. and Van de Walle, C. G., "Temperature and carrier-density dependence of Auger and radiative recombination in nitride optoelectronic devices," New J. Phys. 15(12), 125006 (2013).

[47] Richter, A., Hermle, M. and Glunz, S. W., "Reassessment of the Limiting Efficiency for Crystalline Silicon Solar Cells," IEEE J Photovolt 3(4), 1184–1191 (2013).

[48] Yoshikawa, K., Kawasaki, H., Yoshida, W., Irie, T., Konishi, K., Nakano, K., Uto, T., Adachi, D., Kanematsu, M., Uzu, H. and Yamamoto, K., "Silicon heterojunction solar cell with interdigitated back contacts for a photoconversion efficiency over 26%," Nat Energy 2(5), 17032 (2017).

[49] Schäfer, S. and Brendel, R., "Accurate Calculation of the Absorptance Enhances Efficiency Limit of Crystalline Silicon Solar Cells With Lambertian Light Trapping," IEEE J Photovolt 8(4), 1156–1158 (2018).

[50] M. Boroditsky *et al.*, "Surface recombination measurements on III–V candidate materials for nanostructure light-emitting diodes," *Journal of Applied Physics*, vol. 87, no. 7, pp. 3497–3504, Apr. 2000, doi: 10.1063/1.372372.

[51] B. Fischer, "Loss Analysis of Crystalline Silicon Solar Cells Using Photoconductance and Quantum Efficiency Measurements," May 2003.

[52] J. F. Geisz and D. J. Friedman, “III N V semiconductors for solar photovoltaic applications,” *Semicond. Sci. Technol.*, vol. 17, no. 8, pp. 769–777, Aug. 2002, doi: 10.1088/0268-1242/17/8/305.

[53] Y. Zou, C. Zhang, C. Honsberg, D. Vasileska, R. King, and S. Goodnick, “A lattice-matched GaNP/Si three-terminal tandem solar cell,” *2018 IEEE 7th World Conf. Photovolt. Energy Convers (WCPEC 2018)*, pp. 0279–0282, June 2018, doi: 10.1109/PVSC.2018.8548033

[54] S. Sukrittanon *et al.*, “Enhanced conversion efficiency in wide-bandgap GaNP solar cells,” *Appl. Phys. Lett.*, vol. 107, no. 15, p. 153901, Oct. 2015, doi: 10.1063/1.4933317.

[55] L. N. Dvoretckaia *et al.*, “GaNP-based photovoltaic device integrated on Si substrate,” *Solar Energy Materials and Solar Cells*, vol. 206, p. 110282, Mar. 2020, doi: 10.1016/j.solmat.2019.110282.

[56] S. Mitsuyoshi, K. Umeno, Y. Furukawa, N. Urakami, A. Wakahara, and H. Yonezu, “Electrical and luminescence properties of Mg-doped p-type GaPN grown by molecular beam epitaxy,” *physica status solidi c*, vol. 7, no. 10, pp. 2498–2501, 2010, doi: https://doi.org/10.1002/pssc.200983851.

[57] A. G. Balanta *et al.*, “Effects of nitrogen incorporation and thermal annealing on the optical and spin properties of GaPN dilute nitride alloys,” *Journal of Alloys and Compounds*, vol. 814, p. 152233, Jan. 2020, doi: 10.1016/j.jallcom.2019.152233.

[58] N. P. Irvin *et al.*, “Annealing and Hydrogenation of GaNP Lattice Matched to Si,” *2021 IEEE 48th Photovoltaic Specialists Conference (PVSC)*, p. 5, 2021.

[59] B. J. Hallam *et al.*, “Advanced Hydrogenation of Dislocation Clusters and Boron-oxygen Defects in Silicon Solar Cells,” *Energy Procedia*, vol. 77, pp. 799–809, Aug. 2015, doi: 10.1016/j.egypro.2015.07.113.

[60] C. R. Brown *et al.*, “The effect and nature of N–H complexes in the control of the dominant photoluminescence transitions in UV-hydrogenated GaInNAs,” *RSC Adv.*, vol. 7, no. 41, pp. 25353–25361, 2017, doi: 10.1039/C7RA02900D.

[61] D. Dagnelund *et al.*, “Effects of hydrogenation on non-radiative defects in GaNP and GaNAs alloys: An optically detected magnetic resonance study,” *Journal of Applied Physics*, vol. 111, no. 2, p. 023501, Jan. 2012, doi: 10.1063/1.3676576.

[62] H. Helmers *et al.*, “Photovoltaic Cells with Increased Voltage Output for Optical Power Supply of Sensor Electronics,” *Proceedings SENSOR 2015*, pp. 519–524, May 2015, doi: 10.5162/sensor2015/D1.4.

[63] S. Fafard *et al.*, “Ultrahigh efficiencies in vertical epitaxial heterostructure architectures,” *Appl. Phys. Lett.*, vol. 108, no. 7, p. 071101, Feb. 2016, doi: 10.1063/1.4941240.

[64] H. Helmers *et al.*, "68.9% Efficient GaAs-Based Photonic Power Conversion Enabled by Photon Recycling and Optical Resonance," *physica status solidi (RRL) – Rapid Research Letters*, vol. n/a, no. n/a, p. 2100113, doi: https://doi.org/10.1002/pssr.202100113.

[65] O. Höhn, M. Schauerte, P. Schygulla, H. Hauser, D. Lackner, B. Bläsi, and H. Helmers, in *2022 IEEE 49th Photovoltaics Specialists Conference (PVSC)* (2022), pp. 0038–0042.

[66] N. Vandamme, "Nanostructured ultrathin GaAs solar cells," Ph.D. thesis, Paris-Sud Univ., Orsay, France, 2015, [Online]. Available: https://www.theses.fr/2015PA112111/abes/VD2_VANDAMME_NICOLAS_30062015.pdf

[67] Y. Takeda, "Light trapping for photovoltaic cells used for optical power transmission," *Appl. Phys. Express*, vol. 13, no. 5, p. 054001, May 2020, doi: 10.35848/1882-0786/ab8056.

[68] N. Nouri, C. E. Valdivia, M. N. Beattie, M. S. Zamiri, J. J. Krich, and K. Hinzer, "Ultrathin monochromatic photonic power converters with nanostructured back mirror for light trapping of 1310-nm laser illumination," in *Physics, Simulation, and Photonic Engineering of Photovoltaic Devices X*, Mar. 2021, vol. 11681, p. 116810X. doi: 10.1117/12.2584689.

[69] O. Höhn *et al.*, "Realization of Ultrathin GaAs Photonic Power Converters with Rear-Side Metal Grating on Full 4" Wafers," in *2022 IEEE 49th Photovoltaics Specialists Conference (PVSC)*, Jun. 2022, pp. 0038–0042. doi: 10.1109/PVSC48317.2022.9938600.

[70] J. J. Wysocki and P. Rappaport, "Effect of Temperature on Photovoltaic Solar Energy Conversion," *J. Appl. Phys.*, vol. 31, no. 3, pp. 571–578, Mar. 1960, doi: 10.1063/1.1735630.

[71] L. Xu *et al.*, "Heat generation and mitigation in silicon solar cells and modules," *Joule*, vol. 5, no. 3, pp. 631–645, Mar. 2021, doi: 10.1016/j.joule.2021.01.012.

[72] M. A. Green, "General temperature dependence of solar cell performance and implications for device modelling," *Progress in Photovoltaics: Research and Applications*, vol. 11, no. 5, pp. 333–340, 2003, doi: 10.1002/pip.496.

[73] O. Dupré, R. VAILLON, and M. A. Green, *Thermal Behavior of Photovoltaic Devices: Physics and Engineering*, Springer International Publishing AG, 2017, pp. 3, doi: 10.1007/978-3-319-49457-9.

[74] S. Catalanotti, V. Cuomo, G. Piro, D. Ruggi, V. Silvestrini, and G. Troise, "The radiative cooling of selective surfaces," *Solar Energy*, vol. 17, no. 2, pp. 83–89, May 1975, doi: 10.1016/0038-092X(75)90062-6.

[75] A. P. Raman, M. A. Anoma, L. Zhu, E. Rephaeli, and S. Fan, "Passive radiative cooling below ambient air temperature under direct sunlight," *Nature*, vol. 515, no. 7528, pp. 540–544, Nov. 2014, doi: 10.1038/nature13883.

[76] G. Perrakis, A. C. Tasolamprou, G. Kenanakis, E. N. Economou, S. Tzortzakis, and M. Kafesaki, "Combined nano and micro structuring for enhanced radiative cooling and efficiency of photovoltaic cells," *Sci Rep*, vol. 11, no. 1, p. 11552, Dec. 2021, doi: 10.1038/s41598-021-91061-1.

[77] L. Zhu, A. Raman, K. X. Wang, M. A. Anoma, and S. Fan, "Radiative cooling of solar cells," *Optica*, vol. 1, no. 1, p. 32, Jul. 2014, doi: 10.1364/OPTICA.1.000032.

[78] E. Rephaeli and S. Fan, "Absorber and emitter for solar thermo-photovoltaic systems to achieve efficiency exceeding the Shockley-Queisser limit," *Opt. Express, OE*, vol. 17, no. 17, pp. 15145–15159, Aug. 2009, doi: 10.1364/OE.17.015145.

[79] Y. X. Yeng *et al.*, "Enabling high-temperature nanophotonics for energy applications," *Proceedings of the National Academy of Sciences*, vol. 109, no. 7, pp. 2280–2285, Feb. 2012, doi: 10.1073/pnas.1120149109.

[80] X. Sun, Y. Sun, Z. Zhou, M. A. Alam, and P. Bermel, "Radiative sky cooling: fundamental physics, materials, structures, and applications," *Nanophotonics*, vol. 6, no. 5, pp. 997–1015, Jul. 2017, doi: 10.1515/nanoph-2017-0020.

[81] S. Jeon and J. Shin, "Ideal spectral emissivity for radiative cooling of earthbound objects," *Sci Rep*, vol. 10, no. 1, Art. no. 1, Aug. 2020, doi: 10.1038/s41598-020-70105-y.

[82] K. McCabe, "Modeling Thermal Behavior of Vehicle Integrated Photovoltaics," B.S. thesis, Dept. Mech. Eng., Ohio State Univ., Columbus, OH, USA, 2021. [Online]. Available: https://kb.osu.edu/bitstream/handle/1811/92462/ThesisMcCabe_FinalDraft.pdf?sequence=1&isAllowed=y

[83] J. J. Bloem, "Evaluation of a PV-integrated building application in a well-controlled outdoor test environment," *Build. Environ.,* vol. 43, no. 2, pp. 205–216, Feb. 2008, doi: 10.1016/j.buildenv.2006.10.041.

[84] G. A. Landis, "Review of solar cell temperature coefficients for space," NASA Lewis Research Center, Cleveland, OH (United States), N-95-20502; NASA-CP-3278; E-9083; NAS-1.55:3278; CONF-9406314-, Sep. 1994. Accessed: Aug. 26, 2021. [Online]. Available: https://www.osti.gov/biblio/36446-review-solar-cell-temperature-coefficients-space

[85] T. J. Silverman, M. G. Deceglie, B. Marion, S. Cowley, B. Kayes, and S. Kurtz, "Outdoor performance of a thin-film gallium-arsenide photovoltaic module," in *2013 IEEE 39th Photovoltaic Specialists Conference (PVSC)*, Jun. 2013, pp. 0103–0108. doi: 10.1109/PVSC.2013.6744109.

[86] T. J. Silverman *et al.*, "Reducing Operating Temperature in Photovoltaic Modules," *IEEE Journal of Photovoltaics*, vol. 8, no. 2, pp. 532–540, Mar. 2018, doi: 10.1109/JPHOTOV.2017.2779842.

[87] X. Sun, T. J. Silverman, Z. Zhou, M. R. Khan, P. Bermel, and M. A. Alam, "Optics-Based Approach to Thermal Management of Photovoltaics: Selective-Spectral and Radiative Cooling," *IEEE J. Photovoltaics*, vol. 7, no. 2, pp. 566–574, Mar. 2017, doi: 10.1109/JPHOTOV.2016.2646062.

[88] R. Vaillon, O. Dupré, R. B. Cal, and M. Calaf, "Pathways for mitigating thermal losses in solar photovoltaics," *Sci Rep*, vol. 8, no. 1, p. 13163, Dec. 2018, doi: 10.1038/s41598-018-31257-0.

[89] G. Perrakis, A. C. Tasolamprou, G. Kenanakis, E. N. Economou, S. Tzortzakis, and M. Kafesaki, "Passive radiative cooling and other photonic approaches for the temperature control of photovoltaics: a comparative study for crystalline silicon-based architectures," *Opt. Express*, vol. 28, no. 13, pp. 18548-18565, Jun. 2020, doi: 10.1364/OE.388208.

[90] J. L. Bryan, T. J. Silverman, M. G. Deceglie, M. Mahaffey, P. Firth, and Z. C. Holman, "Systematic Operating Temperature Differences Between Al-BSF, PERC, and PERT-With-Optimized-Rear-Reflector Solar Mini-Modules Due to Rear Reflectance," *IEEE Journal of Photovoltaics*, vol. 12, no. 1, pp. 293–300, Jan. 2022, doi: 10.1109/JPHOTOV.2021.3127447.

[91] N. P. Irvin, D. M. Escobar, A. Wheeler, R. R. King, C. B. Honsberg, and S. R. Kurtz, "Thermal Impact of Rear Insulation, Light Trapping, and Parasitic Absorption in Solar Modules," *IEEE Journal of Photovoltaics*, vol. 12, no. 4, pp. 1043–1050, Jul. 2022, doi: 10.1109/JPHOTOV.2022.3173785.

[92] "Reference Air Mass 1.5 Spectra, ASTM G-173-03.", National Renewable Energy Laboratory, 2012, https://www.nrel.gov/grid/solar-resource/spectra-am1.5.html.

[93] Wurfel, P., "The chemical potential of radiation," *J. Phys. C: Solid State Phys*. 15(18), 3967–3985 (1982).

[94] Green, M. A., "Lambertian light trapping in textured solar cells and light-emitting diodes: analytical solutions," Prog Photovoltaics 10(4), 235–241 (2002).

[95] Rau, U., "Reciprocity relation between photovoltaic quantum efficiency and electroluminescent emission of solar cells," *Phys. Rev. B* 76(8) (2007).

[96] Miller, O. D., Yablonovitch, E. and Kurtz, S. R., "Strong Internal and External Luminescence as Solar Cells Approach the Shockley–Queisser Limit," *IEEE J Photovolt* 2(3), 303–311 (2012).

[97] Richter, A., Glunz, S. W., Werner, F., Schmidt, J. and Cuevas, A., "Improved quantitative description of Auger recombination in crystalline silicon," *Phys. Rev. B* 86(16) (2012).

[98] N. P. Irvin, Sean J. Babcock, Eric Y. Chen, Richard R. King, and Christiana B. Honsberg, "Benefits of Lambertian light distribution across widely deployed photovoltaic materials," *Proc. SPIE*, vol. 11275, Mar. 2020, doi: https://doi.org/10.1117/12.2543935

[99] N. P. Irvin, S. J. Babcock, E. Y. Chen, R. R. King, and C. B. Honsberg, "Feedback between radiation and transport in photovoltaics," *Progress in Photovoltaics: Research and Applications*, vol. n/a, no. n/a, Dec. 2022, doi: 10.1002/pip.3640.

[100] P. Kowalczewski, L. Redorici, A. Bozzola, and L.C. Andreani, "Silicon solar cells reaching the efficiency limits: from simple to complex modelling," J. Opt. 18(5), 054001 (2016).

[101] Richter A, Hermle M, Glunz SW. Reassessment of the Limiting Efficiency for Crystalline Silicon Solar Cells. *IEEE Journal of Photovoltaics* 2013; **3**: 1184–1191.

[102] X. Wang, M. R. Khan, J. L. Gray, M. A. Alam, and M. S. Lundstrom, "Design of GaAs Solar Cells Operating Close to the Shockley–Queisser Limit," *IEEE J. Photovoltaics*, vol. 3, no. 2, pp. 737–744, Apr. 2013, doi: 10.1109/JPHOTOV.2013.2241594.

[103] M. P. Lumb, M. A. Steiner, J. F. Geisz, and R. J. Walters, "Incorporating photon recycling into the analytical drift-diffusion model of high efficiency solar cells," Journal of Applied Physics, vol. 116, no. 19, p. 194504, Nov. 2014, doi: 10.1063/1.4902320.

[104] "Reference Air Mass 1.5 Spectra, ASTM G-173-03," National Renewable Energy Laboratory, 2012. https://www.nrel.gov/grid/solar-resource/spectra-am1.5.html (accessed Dec. 31, 2019).

[105] Barnett, A. M. and Rothwarf, A., "Thin-film solar cells: A unified analysis of their potential," *IEEE Trans. Electron Devices* 27(4), 615–630 (1980).

[106] Green, M. A., "Self-consistent optical parameters of intrinsic silicon at 300K including temperature coefficients," *Sol Energ Mat Sol C* 92(11), 1305–1310 (2008).

[107] Palik, E., [Handbook of Optical Constants of Solids], 1st ed., Academic Press, New York (1985).

[108] Paulson, P. D., Birkmire, R. W. and Shafarman, W. N., "Optical characterization of $CuIn_{1-x}Ga_xSe_2$ alloy thin films by spectroscopic ellipsometry," *J. Appl. Phys* 94(2), 879–888 (2003).

[109] Adachi, S., "Optical dispersion relations for GaP, GaAs, GaSb, InP, InAs, InSb, $Al_xGa_{1-x}As$, and $In_{1-x}Ga_xAs_yP_{1-y}$," *J. Appl. Phys* 66(12), 6030–6040 (1989).

[101] Treharne, R. E., Seymour-Pierce, A., Durose, K., Hutchings, K., Roncallo, S. and Lane, D., "Optical Design and Fabrication of Fully Sputtered CdTe/CdS Solar Cells," *J. Phys.: Conf. Ser.* 286, 012038 (2011).

[110] A. B. Sproul, "Dimensionless solution of the equation describing the effect of surface recombination on carrier decay in semiconductors," *Journal of Applied Physics*, vol. 76, no. 5, pp. 2851–2854, Sep. 1994, doi: 10.1063/1.357521.

[112] B. Archambeault, O. M. Ramahi, and C. Brench, "The Finite-Difference Time-Domain Method," in *EMI/EMC Computational Modeling Handbook*, B. Archambeault, O. M. Ramahi, and C. Brench, Eds. Boston, MA: Springer US, 1998, pp. 35–36. doi: 10.1007/978-1-4757-5124-6_3.

[113] H. J. Hagemann, W. Gudat, and C. Kunz, J. Opt. Soc. Am., 65, 742, 1975.

[114] E. Shiles, T., Sasaki, M., Inokuti, and D. Y. Smith, Phys. Rev. Sect. B, 22, 1612, 1980.

[115] C. G. Olson, D. W. Lynch, and J. H. Weaver, unpublished.

[116] "Thin film GaAs solar cell," *Ansys Optics*. https://optics.ansys.com/hc/en-us/articles/360042160334-Thin-film-GaAs-solar-cell (accessed Mar. 23, 2023).

[117] M. J. Dodge. Refractive properties of magnesium fluoride, *Appl. Opt.* **23**, 1980-1985 (1984).

[118] E. Palik, *Handbook of Optical Constants of Solids*, 1st ed. New York: Academic Press, 1985.

[119] J. Liu, C. Chen, G. Yang, Y. Chen, and C.-F. Yang, "Effect of the Fabrication Parameters of the Nanosphere Lithography Method on the Properties of the Deposited Au-Ag Nanoparticle Arrays," *Materials (Basel)*, vol. 10, no. 4, p. 381, Apr. 2017, doi: 10.3390/ma10040381.

[120] J. Hong *et al.*, "Comparison of plasma chemistries for inductively coupled plasma etching of InGaAlP alloys," *Journal of Vacuum Science & Technology A: Vacuum, Surfaces, and Films*, vol. 16, no. 3, pp. 1497–1501, May 1998, doi: 10.1116/1.581176.

[121] X. Yang and J. A. Hopwood, "Physical mechanisms for anisotropic plasma etching of cesium iodide," *Journal of Applied Physics*, vol. 96, no. 9, pp. 4800–4806, Nov. 2004, doi: 10.1063/1.1803607.

[122] S. Combrié *et al.*, "Optimization of an inductively coupled plasma etching process of GaInP⁄GaAs based material for photonic band gap applications," *Journal of*

Vacuum Science & Technology B: Microelectronics and Nanometer Structures Processing, Measurement, and Phenomena, vol. 23, no. 4, pp. 1521–1526, Jul. 2005, doi: 10.1116/1.1993617.

[123] M. de Lafontaine *et al.*, "Anisotropic and low damage III-V/Ge heterostructure etching for multijunction solar cell fabrication with passivated sidewalls," *Micro and Nano Engineering*, vol. 11, p. 100083, Jun. 2021, doi: 10.1016/j.mne.2021.100083.

[124] J. Hong *et al.*, "Comparison of plasma chemistries for inductively coupled plasma etching of InGaAlP alloys," *Journal of Vacuum Science & Technology A: Vacuum, Surfaces, and Films*, vol. 16, no. 3, pp. 1497–1501, May 1998, doi: 10.1116/1.581176.

[125] M. Muller, B. Marion, and J. Rodriguez, "Evaluating the IEC 61215 Ed.3 NMOT procedure against the existing NOCT procedure with PV modules in a side-by-side configuration," in *2012 38th IEEE Photovoltaic Specialists Conference*, Jun. 2012, pp. 000697–000702. doi: 10.1109/PVSC.2012.6317705.

[126] M. A. Goforth, G. W. Gilchrist, and J. D. Sirianni, "Cloud effects on thermal downwelling sky radiance," in *Thermosense XXIV*, Mar. 2002, vol. 4710, pp. 203–213. doi: 10.1117/12.459570.

[127] Wheeler, M. Leveille, I. Anton, M. Limpinsel, and S. Kurtz, "Outdoor Performance of PV Technologies in Simulated Automotive Environments," in *2019 IEEE 46th Photovoltaic Specialists Conference (PVSC)*, Jun. 2019, pp. 3103–3110. doi: 10.1109/PVSC40753.2019.8981352.

[128] N. H. Reich, B. Mueller, A. Armbruster, W. G. J. H. M. Sark, K. Kiefer, and C. Reise, "Performance ratio revisited: is PR > 90% realistic?," *Progress in Photovoltaics: Research and Applications*, vol. 20, no. 6, 2012, doi: 10.1002/pip.1219.

[129] I. Subedi, T. J. Silverman, M. G. Deceglie, and N. J. Podraza, "PERC silicon PV infrared to ultraviolet optical model," *Sol. Energy Mater Sol. Cells*, vol. 215, p. 110655, Sep. 2020, doi: 10.1016/j.solmat.2020.110655.

[130] R. J. Cole and N. S. Sturrock, "The convective heat exchange at the external surface of buildings," *Build. Environ.*, vol. 12, no. 4, pp. 207–214, Jan. 1977, doi: 10.1016/0360-1323(77)90021-X.

[131] J. W. Sparrow W M and E. A. Mass, "Effect of Finite Width on Heat Transfer and Fluid Flow about an Inclined Rectangular Plate," *J Heat Transfer – T ASME*, vol. 101, no. 2, pp. 199–204, May 1979 doi: 10.1115/1.3450946.

[132] J. Watmuff, W. Charters, and D. Proctor, "Solar and wind induced external coefficients - Solar collectors," 2nd Revue Internationale d'Heliotechnique, p. 56, Jun. 1977.

[133] M. Hammami, S. Torretti, F. Grimaccia, and G. Grandi, "Thermal and Performance Analysis of a Photovoltaic Module with an Integrated Energy Storage System," *Appl. Sci.,* vol. 7, no. 11, Art. no. 11, Nov. 2017, doi: 10.3390/app7111107.

[134] A. Goetzberger, "Optical confinement in thin Si-solar cells by diffuse back reflectors," *15th PVSC Proc.*, pp. 867–870, May 1981.

[135] J. M. Gee, "The effect of parasitic absorption losses on light trapping in thin silicon solar cells," in *20th PVSC Proc.*, Sep. 1988, pp. 549–554 vol.1. doi: 10.1109/PVSC.1988.105762.

[136] Z. C. Holman *et al.*, "Parasitic absorption in the rear reflector of a silicon solar cell: Simulation and measurement of the sub-bandgap reflectance for common dielectric/metal reflectors," *Sol. Energy Mater Sol. Cells,* vol. 120, pp. 426–430, Jan. 2014, doi: 10.1016/j.solmat.2013.06.024.

[137] M. Vogt, "Development of physical models for the simulation of optical properties of solar cell modules," 2015. doi: 10.15488/8592.

[138] M. Rüdiger, J. Greulich, A. Richter, and M. Hermle, "Parameterization of Free Carrier Absorption in Highly Doped Silicon for Solar Cells," *IEEE Trans. Electron Devices*, vol. 60, no. 7, pp. 2156–2163, Jul. 2013, doi: 10.1109/TED.2013.2262526.

[139] P. Uprety, I. Subedi, M. Junda, R. Collins, and N. Podraza, "Photogenerated Carrier Transport Properties in Silicon Photovoltaics," *Sci. Rep.*, vol. 9, p. 19015, Dec. 2019, doi: 10.1038/s41598-019-55173-z.

[140] B. Min et al., "A Roadmap Toward 24% Efficient PERC Solar Cells in Industrial Mass Production," *IEEE J. Photovolt.,* vol. PP, pp. 1–10, Sep. 2017, doi: 10.1109/JPHOTOV.2017.2749007.

[141] M. A. Green, "Lambertian light trapping in textured solar cells and light-emitting diodes: analytical solutions," *Prog. Photovolt.: Res. Appl.*, vol. 10, no. 4, pp. 235–241, Jun. 2002, doi: 10.1002/pip.404.

[142] E. Yablonovitch, O. D. Miller, and S. R. Kurtz, "A great solar cell also needs to be a great LED: External fluorescence leads to new efficiency record," presented at the NOBEL SYMPOSIUM 153: NANOSCALE ENERGY CONVERTERS, Orenas Castle, Sweden, Orenas Castle, Sweden, 2013, pp. 9–11. doi: 10.1063/1.4794698.

[143] E. Y. Chen, S. J. Babcock, N. P. Irvin, and R. R. King, "Enhanced Internal Reflectance of Emission in Solar Cells with Angle- and Energy-selective Reflectors," in *2020 47th IEEE Photovoltaic Specialists Conference (PVSC)*, Jun. 2020, pp. 2010–2016. doi: 10.1109/PVSC45281.2020.9300407.

[144] E. Chen, S. J. Babcock, N. P. Irvin, and R. R. King, "Enabling high-efficiency photovoltaics by tailoring monochromatic illumination to energy-selective front reflectors." Proc. SPIE 11496, New Concepts in Solar and Thermal Radiation Conversion III, 114960C, Aug. 2020); https://doi.org/10.1117/12.2568196

[145] S. J. Babcock, N. P. Irvin, E. Y. Chen, C. B. Honsberg, and R. R. King, "Effects of high photon gas density and radiative efficiency on upper bounds of energy conversion efficiency in single-crystal solar cells," in *2019 IEEE 46th Photovoltaic Specialists Conference (PVSC)*, Jun. 2019, pp. 3195–3199. doi: 10.1109/PVSC40753.2019.8980473.

[146] P. Altermatt et al., "The extraction of the surface recombination velocity of Si:P emitters using advanced silicon models," May 2000.

[147] S. Schäfer, D. Turkay, C. Gemmel, S. Kajari-Schröder, and R. Brendel, *Macroporous blind holes as surface texture for high efficiency silicon solar cells*. 2015.

[148] S. Murali, N. P. Irvin, C. Zhang, R. R. King, and C. B. Honsberg, "Epitaxial GaP grown on Silicon by MEE and MBE Techniques as a Pathway for Dilute Nitride-Si Tandem Solar Cells," in *2019 IEEE 46th Photovoltaic Specialists Conference (PVSC)*, Jun. 2019, pp. 1044–1048. doi: 10.1109/PVSC40753.2019.8980577.

[149] I. A. Buyanova, G. Pozina, J. P. Bergman, W. M. Chen, H. P. Xin, and C. W. Tu, "Time-resolved studies of photoluminescence in GaNxP1−x alloys: Evidence for indirect-direct band gap crossover," *Appl. Phys. Lett.*, vol. 81, no. 1, pp. 52–54, Jul. 2002, doi: 10.1063/1.1491286.

[150] M. Baranowski et al., "Temperature evolution of carrier dynamics in GaN x P y As 1−y−x alloys," Journal of Applied Physics, vol. 117, no. 17, p. 175702, May 2015, doi: 10.1063/1.4919751.

[151] I. García, I. Rey-Stolle, B. Galiana, and C. Algora, "Analysis of tellurium as n-type dopant in GaInP: Doping, diffusion, memory effect and surfactant properties," *Journal of Crystal Growth*, vol. 298, pp. 794–799, Jan. 2007, doi: 10.1016/j.jcrysgro.2006.10.099.

[152] T. J. Grassman, D. J. Chmielewski, S. D. Carnevale, J. A. Carlin, and S. A. Ringel, "GaAs0.75P0.25/Si Dual-Junction Solar Cells Grown by MBE and MOCVD," *IEEE Journal of Photovoltaics*, vol. 6, no. 1, pp. 326–331, Jan. 2016, doi: 10.1109/JPHOTOV.2015.2493365.

[153] D. J. Wolford *et al.*, "Interface-free GaAs structures—from bulk to the quantum limit," in *Gallium Arsenide and Related Compounds 1991*, CRC Press, 1992, pp. 403-404.

[154] A. J. Ptak, D. J. Friedman, and S. W. Johnston, "A comparison of MBE- and MOCVD-grown InGaAsN," in *International Conference on Molecular Bean Epitaxy*, Sep. 2002, pp. 291–292. doi: 10.1109/MBE.2002.1037874.

[155] M. Sheik-Bahae, B. Imangholi, M. P. Hasselbeck, R. I. Epstein, and S. Kurtz, "Advances in laser cooling of semiconductors," in *Physics and Simulation of Optoelectronic Devices XIV*, Feb. 2006, vol. 6115, pp. 186–198. doi: 10.1117/12.644915.

[156] N. P. Irvin *et al.*, "Monochromatic Light Trapping in Photonic Power Converters," in *2022 IEEE 49th Photovoltaics Specialists Conference (PVSC)*, Jun. 2022, pp. 0143–0143. doi: 10.1109/PVSC48317.2022.9938800.

[157] N. Vandamme *et al.*, "Ultrathin GaAs Solar Cells With a Silver Back Mirror," *IEEE Journal of Photovoltaics*, vol. 5, no. 2, pp. 565–570, Mar. 2015, doi: 10.1109/JPHOTOV.2014.2371236.

[158] H. Elsner, H.-G. Meyer, A. Voigt, and G. Grützner, "Evaluation of ma-N 2400 series DUV photoresist for electron beam exposure," Microelectronic Engineering, vol. 46, no. 1–4, pp. 389–392, May 1999, doi: 10.1016/S0167-9317(99)00113-6.

[159] D. J. Thoen, V. Murugesan, A. Pascual Laguna, K. Karatsu, A. Endo, and J. J. A. Baselmans, "Combined ultraviolet- and electron-beam lithography with Micro-Resist-Technology GmbH ma-N1400 resist," Journal of Vacuum Science & Technology B, vol. 40, no. 5, p. 052603, Sep. 2022, doi: 10.1116/6.0001918.

[160] A. Goodyear, M. Boettcher, I. Stolberg, and M. Cooke, "Direct comparison of the performance of commonly used e-beam resists during nano-scale plasma etching of Si, SiO2, and Cr," in Advanced Etch Technology for Nanopatterning IV, Mar. 2015, vol. 9428, pp. 141–148. doi: 10.1117/12.2085469.

[161] A. Chikhalkar, "Interaction of Charge Carriers with Defects at Interfaces and Grain Boundaries in Compound Semiconductors," Ph.D. dissertation, Arizona State University, United States -- Arizona, 2021. [Online]. Available: https://www.proquest.com/docview/2532530663/abstract/C26FEE4772644BA3PQ/1

[162] X. Sun, T. J. Silverman, Z. Zhou, M. R. Khan, P. Bermel, and M. A. Alam, "Optics-Based Approach to Thermal Management of Photovoltaics: Selective-Spectral and Radiative Cooling," *IEEE J. Photovoltaics*, vol. 7, no. 2, pp. 566–574, Mar. 2017, doi: 10.1109/JPHOTOV.2016.2646062.

[163] R. Vaillon, O. Dupré, R. B. Cal, and M. Calaf, "Pathways for mitigating thermal losses in solar photovoltaics," *Sci Rep*, vol. 8, no. 1, p. 13163, Dec. 2018, doi: 10.1038/s41598-018-31257-0.

[164] G. Perrakis, A. C. Tasolamprou, G. Kenanakis, E. N. Economou, S. Tzortzakis, and M. Kafesaki, "Passive radiative cooling and other photonic approaches for the temperature control of photovoltaics: a comparative study for crystalline silicon-based architectures," *Opt. Express*, vol. 28, no. 13, pp. 18548-18565, Jun. 2020, doi: 10.1364/OE.388208.

[165] E. Yablonovitch, "Statistical ray optics," *J. Opt. Soc. Am., JOSA*, vol. 72, no. 7, pp. 899–907, Jul. 1982, doi: 10.1364/JOSA.72.000899.

[166] P. A. Basore, "Extended spectral analysis of internal quantum efficiency," *38th PVSC Proc.*, May 1993, pp. 147–152. doi: 10.1109/PVSC.1993.347063.

[167] J. Müller, S. Gatz, and R. Brendel, "Optimizing the geometry of local aluminum-alloyed contacts to fully screen-printed silicon solar cells," *38th PVSC Proc.*, Jun. 2012.

[168] V. Petrova-Koch, R. Hezel, and A. Goetzberger, Eds., High-Efficient Low-Cost Photovoltaics: Recent Developments. Berlin Heidelberg: Springer-Verlag, 2009, pp. 65–94. doi: 10.1007/978-3-540-79359-5.

[169] J. L. Bryan *et al.*, "Inserting a Low-Refractive-Index Dielectric Rear Reflector into PERC Cells: Challenges and Opportunities," Piscataway, NJ: Institute of Electrical and Electronics Engineers (IEEE), NREL/CP-5K00-76282, Feb. 2020. doi: 10.1109/PVSC40753.2019.8980513.

[170] I. Subedi, T. J. Silverman, M. G. Deceglie, and N. J. Podraza, "Al+Si Interface Optical Properties Obtained in the Si Solar Cell Configuration," *physica status solidi (a)*, vol. 214, no. 12, p. 1700480, 2017, doi: 10.1002/pssa.201700480.

[171] S. Kurtz *et al.*, "Evaluation of high-temperature exposure of photovoltaic modules," *Prog. Photovolt.: Res. Appl.*, vol. 19, no. 8, pp. 954–965, 2011, doi: 10.1002/pip.1103.

[172] N. C. Park, W. W. Oh, and D. H. Kim, "Effect of Temperature and Humidity on the Degradation Rate of Multicrystalline Silicon Photovoltaic Module," *Int. J. Photoenergy*, vol. 2013, pp. 1–9, 2013, doi: 10.1155/2013/925280.

[173] A. Pfreundt, A. J. Beinert, D. Yucebas, L. V. Mesquita, L. Pitta-Bauermann, and M. Mittag, "Post-Processing Thickness Variation of PV Module Materials and its Impact on Temperature, Mechanical Stress and Power," *EU PVSEC 2019,* Sep. 2019.

[174] M. Mittag, I. Haedrich, T. Neff, S. Hoffmann, U. Eitner, and H. Wirth, "TPedge: qualification of a gas-filled, encapsulation-free glass-glass photovoltaic module.," *EU PVSEC 2015*, Aug. 2015. doi: 10.4229/EUPVSEC20152015-1CO.11.4.

[176] A. Shamim, M. Noman, M. Zubair, A. D. Khan, and S. Saher, "A facile approach to determine the unknown refractive index (n) and extinction coefficient (k) of novel encapsulant materials used in back contact PV modules," *Appl. Phys. A*, vol. 124, no. 8, p. 542, Aug. 2018, doi: 10.1007/s00339-018-1974-x.

[176] W. Li, Y. Shi, K. Chen, L. Zhu, and S. Fan, "A Comprehensive Photonic Approach for Solar Cell Cooling," *ACS Photonics*, vol. 4, no. 4, pp. 774–782, Apr. 2017, doi: 10.1021/acsphotonics.7b00089.

[177] I. M. Slauch, M. G. Deceglie, T. J. Silverman, and V. E. Ferry, “Model for Characterization and Optimization of Spectrally Selective Structures to Reduce the Operating Temperature and Improve the Energy Yield of Photovoltaic Modules,” ACS Appl. Energy Mater., vol. 2, no. 5, pp. 3614–3623, May 2019, doi: 10.1021/acsaem.9b00347.

[178] I. M. Slauch, M. G. Deceglie, T. J. Silverman, and V. E. Ferry, “Optical approaches for passive thermal management in c-Si photovoltaic modules,” *Cell Rep. Phys. Sci.*, vol. 2, no. 5, p. 100430, May 2021, doi: 10.1016/j.xcrp.2021.100430.

[179] X. Yu, Y. Qin, and Q. Peng, “Probe Decomposition of Methylammonium Lead Iodide Perovskite in N2 and O2 by in Situ Infrared Spectroscopy,” J. Phys. Chem. A, vol. 121, no. 6, pp. 1169–1174, Feb. 2017, doi: 10.1021/acs.jpca.6b12170.

[180] N. P. Irvin *et al.*, “Deleterious Effect of Light Trapping on the Temperatures of Solar Modules,” in *2022 IEEE 49th Photovoltaics Specialists Conference (PVSC)*, Jun. 2022, pp. 1059–1059. doi: 10.1109/PVSC48317.2022.9938767.

APPENDIX A

REFRACTIVE INDEX AND EXTINCTION COEFFICIENT OF GAINP

Table 10 gives the measured values of the index of refraction n and extinction coefficient k for GaInP lattice matched to GaAs. These values are used in the FDTD modeling of Section 3.III.B.

Table 10
OPTICAL CONSTANTS OF GAINP

Wavelength (nm)	n	k
193.7113	1.46545	2.31907
195.2945	1.466888	2.377887
196.8777	1.495326	2.388957
198.461	1.490964	2.370362
200.0444	1.459977	2.374742
201.6278	1.442579	2.403916
203.2112	1.441152	2.429177
204.7947	1.436463	2.447325
206.3783	1.426143	2.472484
207.9618	1.420408	2.507556
209.5455	1.422726	2.544744
211.1292	1.428494	2.58057
212.7129	1.434749	2.617847
214.2966	1.44336	2.658649
215.8804	1.456472	2.701641
217.4643	1.473338	2.744779
219.0482	1.492207	2.787955
220.6322	1.51258	2.832538
222.2161	1.535079	2.879288
223.8002	1.560457	2.928509
225.3842	1.589587	2.980164
226.9684	1.623352	3.033716
228.5525	1.661878	3.088115
230.1367	1.70445	3.142995
231.7209	1.750392	3.199565
233.3052	1.801513	3.259546
234.8895	1.860796	3.322738
236.4739	1.93083	3.386744
238.0583	2.012201	3.448701
239.6427	2.105198	3.506229
241.2271	2.209519	3.55601
242.8116	2.323007	3.595404
244.3962	2.443368	3.623035
245.9808	2.568485	3.638072
247.5654	2.696328	3.64007
249.15	2.825055	3.628863
250.7347	2.952922	3.604315
252.3194	3.077989	3.566404
253.9041	3.198142	3.515405
255.4889	3.311052	3.452204
257.0737	3.415038	3.378345
258.6585	3.508703	3.295099
260.2434	3.590138	3.20399
261.8283	3.657905	3.108114
263.4132	3.712286	3.010376
264.9982	3.753962	2.912962
266.5832	3.783726	2.81781
268.1682	3.802735	2.726766
269.7532	3.812542	2.641371
271.3383	3.815198	2.562771
272.9234	3.813065	2.49086
274.5085	3.807357	2.424849
276.0937	3.798782	2.364243
277.6789	3.787885	2.308709
279.2641	3.775138	2.258019
280.8493	3.761007	2.211998
282.4346	3.745974	2.170487
284.0198	3.730582	2.133287
285.6052	3.715385	2.099964
287.1905	3.700638	2.06999
288.7758	3.686447	2.042933
290.3612	3.672811	2.018433
291.9466	3.659638	1.996298
293.532	3.646951	1.976473
295.1175	3.634854	1.958887
296.7029	3.623485	1.943447
298.2884	3.613035	1.93001
299.8739	3.603646	1.918309
301.4594	3.595337	1.908081
303.0449	3.588069	1.899105
304.6305	3.581746	1.891198
306.216	3.576211	1.884288
307.8016	3.571409	1.878428
309.3872	3.567376	1.873647
310.9728	3.564191	1.869946
312.5584	3.561976	1.867298
314.1441	3.560897	1.865565
315.7298	3.560998	1.864522
317.3154	3.562239	1.863977
318.9011	3.564531	1.863775
320.4868	3.567738	1.863798
322.0725	3.571658	1.864037
323.6583	3.576201	1.864623
325.244	3.581385	1.865657
326.8297	3.58727	1.867208
328.4155	3.593951	1.869322
330.0013	3.601574	1.871998
331.587	3.610272	1.875126
333.1728	3.620087	1.878579
334.7586	3.631025	1.882252
336.3444	3.643071	1.886055
337.9302	3.656183	1.88992
339.5161	3.670274	1.89384
341.1019	3.685334	1.897919
342.6877	3.701459	1.902242
344.2736	3.718794	1.906854
345.8594	3.737531	1.911769
347.4453	3.757923	1.91696
349.0311	3.780334	1.922271
350.6169	3.805001	1.927286
352.2028	3.831958	1.931621
353.7887	3.861175	1.934953
355.3745	3.892596	1.937
356.9604	3.926173	1.937511
358.5463	3.961906	1.936227
360.1321	3.999791	1.932727
361.718	4.039611	1.926558
363.3039	4.081053	1.917362
364.8898	4.123762	1.90485
366.4756	4.167356	1.888791
368.0615	4.211433	1.868997
369.6474	4.255563	1.84533
371.2332	4.299307	1.81771
372.8191	4.342232	1.786083
374.405	4.383891	1.750412
375.9908	4.423796	1.71067
377.5767	4.461393	1.666852
379.1625	4.49601	1.618977
380.7484	4.526684	1.567177
382.3342	4.552307	1.512337
383.92	4.572512	1.455662
385.5059	4.587278	1.398164
387.0917	4.59675	1.340731
388.6775	4.601195	1.284162
390.2633	4.601001	1.229185
391.8491	4.596708	1.176469
393.4349	4.589143	1.126508
395.0206	4.579103	1.079252
396.6064	4.567036	1.034563
398.1922	4.553263	0.992344
399.7779	4.538055	0.952532
401.3636	4.52165	0.915074
402.9494	4.504276	0.879934
404.5351	4.48616	0.847083
406.1208	4.467569	0.816479
407.7065	4.448776	0.787979
409.2921	4.429956	0.761399
410.8778	4.411236	0.736572
412.4634	4.39271	0.713344
414.0491	4.374451	0.691567
415.6347	4.356509	0.671105
417.2203	4.338918	0.651825
418.8058	4.32169	0.633603
420.3914	4.304803	0.616333
421.977	4.288237	0.599954

423.5625	4.271987	0.584414
425.148	4.256059	0.569665
426.7335	4.240454	0.555656
428.3189	4.225176	0.542341
429.9044	4.210227	0.529673
431.4898	4.195603	0.517606
433.0753	4.181302	0.506098
434.6606	4.167311	0.495108
436.246	4.153614	0.484609
437.8314	4.140203	0.474579
439.4167	4.127074	0.465
441.002	4.114226	0.455851
442.5873	4.101656	0.447114
444.1725	4.089366	0.438769
445.7577	4.077355	0.430797
447.3429	4.065626	0.423181
448.9281	4.054179	0.415902
450.5133	4.043021	0.408942
452.0984	4.032159	0.402277
453.6835	4.021594	0.395877
455.2686	4.011322	0.389713
456.8536	4.001337	0.383759
458.4386	3.991629	0.377989
460.0236	3.982186	0.372378
461.6086	3.972995	0.366901
463.1935	3.964037	0.361536
464.7784	3.955291	0.35626
466.3633	3.946729	0.351052
467.9481	3.938309	0.345898
469.5329	3.929986	0.340809
471.1177	3.921734	0.335812
472.7025	3.913541	0.330929
474.2871	3.905399	0.326182
475.8718	3.897307	0.321592
477.4565	3.889269	0.317177
479.0411	3.881289	0.312957
480.6256	3.873381	0.308949
482.2101	3.86556	0.30517
483.7947	3.857848	0.301635
485.3792	3.850276	0.298359
486.9636	3.842897	0.295341
488.5479	3.835751	0.29255
490.1323	3.82886	0.289947
491.7166	3.822236	0.287499
493.3009	3.815883	0.285172
494.8852	3.809802	0.282934
496.4693	3.803988	0.280754
498.0535	3.798433	0.278603
499.6376	3.793127	0.276452
501.2217	3.788054	0.274274
502.8057	3.783194	0.272044
504.3897	3.778521	0.269737
505.9737	3.774002	0.267331
507.5576	3.769588	0.264821
509.1414	3.765248	0.262224
510.7253	3.760961	0.259553
512.309	3.75671	0.256821
513.8928	3.752482	0.25404
515.4764	3.748267	0.251224
517.0601	3.744056	0.248383
518.6437	3.739844	0.245528
520.2272	3.735625	0.242671
521.8107	3.731395	0.239821
523.3942	3.727152	0.236989
524.9777	3.722893	0.234182
526.561	3.718616	0.231412
528.1443	3.71432	0.228686
529.7275	3.710006	0.226016
531.3107	3.705673	0.22341
532.8939	3.701326	0.220879
534.4771	3.696966	0.218432
536.0601	3.692599	0.21608
537.6431	3.688231	0.213829
539.2261	3.683869	0.21169
540.809	3.67952	0.20967
542.3918	3.675193	0.207776
543.9746	3.670899	0.206017
545.5573	3.66665	0.204399
547.14	3.662459	0.20293
548.7227	3.658344	0.201615
550.3052	3.654325	0.20046
551.8878	3.650434	0.199468
553.4702	3.646704	0.19862
555.0526	3.643155	0.197892
556.6349	3.639798	0.197258
558.2173	3.63664	0.196695
559.7995	3.633686	0.19618
561.3817	3.630936	0.195691
562.9638	3.628388	0.195207
564.5458	3.626039	0.194707
566.1279	3.623883	0.194173
567.7098	3.621913	0.193584
569.2916	3.620119	0.192923
570.8735	3.618489	0.192172
572.4552	3.617009	0.191315
574.0369	3.615664	0.190336
575.6185	3.614433	0.189218
577.2001	3.613289	0.187949
578.7816	3.612195	0.186527
580.363	3.611127	0.184967
581.9445	3.610066	0.18328
583.5258	3.609	0.181481
585.107	3.607919	0.179581
586.6881	3.606816	0.177593
588.2692	3.605684	0.175527
589.8503	3.60452	0.173395
591.4313	3.603319	0.171208
593.0121	3.602082	0.168975
594.593	3.600807	0.166707
596.1738	3.599496	0.164412
597.7545	3.598149	0.162101
599.3351	3.596771	0.159781
600.9156	3.595366	0.157462
602.4962	3.593941	0.155152
604.0765	3.592504	0.152858
605.6569	3.591067	0.150588
607.2372	3.589652	0.148341
608.8174	3.58827	0.146104
610.3975	3.586928	0.143868
611.9775	3.58563	0.141622
613.5575	3.584378	0.139355
615.1374	3.583172	0.137058
616.7172	3.58201	0.134721
618.297	3.58089	0.132336
619.8766	3.579808	0.129893
621.4563	3.578761	0.127384
623.0358	3.577742	0.124801
624.6152	3.576746	0.122136
626.1946	3.575764	0.119382
627.7739	3.574788	0.11653
629.3531	3.573808	0.113574
630.9323	3.572814	0.110507
632.5114	3.571793	0.107323
634.0903	3.570729	0.104014
635.6692	3.569604	0.100576
637.248	3.568394	0.097002
638.8267	3.567065	0.093302
640.4054	3.565595	0.089496
641.9839	3.563971	0.085606
643.5624	3.562181	0.08165
645.1408	3.56022	0.077648
646.7191	3.558083	0.073619
648.2974	3.555767	0.069579
649.8755	3.553272	0.065548
651.4536	3.550596	0.06154
653.0316	3.547743	0.057574
654.6094	3.544715	0.053664
656.1873	3.541516	0.049826
657.765	3.538151	0.046076
659.3426	3.534627	0.042428
660.9201	3.53095	0.038896
662.4976	3.527131	0.035495
664.075	3.523177	0.032237
665.6522	3.519101	0.029138
667.2294	3.514916	0.026209
668.8065	3.510637	0.023464
670.3835	3.506281	0.020915
671.9604	3.501873	0.018575
673.5372	3.497445	0.016444
675.114	3.49302	0.014512
676.6906	3.488617	0.012768
678.2672	3.484248	0.011201
679.8436	3.479926	0.009802
681.4199	3.475659	0.00856
682.9962	3.471457	0.007464
684.5724	3.467324	0.006505
686.1484	3.463269	0.005674
687.7244	3.459296	0.004962
689.3003	3.455408	0.004358
690.8761	3.451609	0.003854
692.4518	3.447902	0.003442
694.0273	3.444289	0.003112
695.6028	3.440772	0.002857
697.1782	3.43735	0.002667
698.7535	3.434025	0.002536
700.3287	3.430796	0.002454
701.9037	3.427662	0.002415

703.4788	3.424621	0.00241
705.0537	3.421673	0.002433
706.6284	3.418813	0.002476
708.2031	3.416039	0.002532
709.7777	3.413346	0.002595
711.3522	3.410727	0.002657
712.9266	3.408173	0.002716
714.5009	3.405679	0.002774
716.075	3.403242	0.002829
717.649	3.400857	0.002881
719.223	3.398521	0.00293
720.7969	3.396232	0.002977
722.3707	3.393988	0.003022
723.9443	3.391786	0.003063
725.5178	3.389624	0.003101
727.0912	3.387501	0.003137
728.6646	3.385416	0.00317
730.2378	3.383365	0.003199
731.8109	3.38135	0.003225
733.3839	3.379367	0.003249
734.9567	3.377416	0.003269
736.5295	3.375495	0.003285
738.1022	3.373604	0.003299
739.6747	3.371742	0.003309
741.2472	3.369906	0.003316
742.8195	3.368098	0.003319
744.3917	3.366315	0.003319
745.9638	3.364557	0.003315
747.5358	3.362823	0.003308
749.1077	3.361111	0.003298
750.6794	3.359423	0.003283
752.2511	3.357755	0.003265
753.8226	3.356109	0.003244
755.394	3.354482	0.003218
756.9654	3.352874	0.003189
758.5365	3.351285	0.003157
760.1076	3.349713	0.003122
761.6786	3.348159	0.003084
763.2494	3.346621	0.003043
764.8201	3.345098	0.003
766.3907	3.343592	0.002954
767.9612	3.3421	0.002906
769.5316	3.340624	0.002857
771.1017	3.339161	0.002805
772.6719	3.337712	0.002751
774.2418	3.336277	0.002697
775.8117	3.334855	0.00264
777.3815	3.333446	0.002583
778.9511	3.332049	0.002525
780.5206	3.330665	0.002465
782.09	3.329293	0.002406
783.6593	3.327932	0.002345
785.2284	3.326583	0.002284
786.7974	3.325245	0.002223
788.3663	3.323918	0.002161
789.9351	3.322602	0.002099
791.5037	3.321297	0.002038
793.0721	3.320002	0.001977
794.6405	3.318717	0.001916
796.2088	3.317443	0.001855
797.7769	3.316179	0.001795
799.3449	3.314924	0.001736
800.9128	3.31368	0.001678
802.4805	3.312445	0.00162
804.0481	3.31122	0.001563
805.6156	3.310004	0.001508
807.1829	3.308798	0.001453
808.7501	3.307602	0.0014
810.3173	3.306415	0.001348
811.8842	3.305237	0.001296
813.451	3.304069	0.001246
815.0177	3.30291	0.001197
816.5842	3.30176	0.001149
818.1506	3.300619	0.001102
819.7169	3.299487	0.001056
821.283	3.298364	0.001011
822.849	3.297249	0.000967
824.4149	3.296143	0.000924
825.9807	3.295046	0.000883
827.5463	3.293957	0.000842
829.1117	3.292876	0.000803
830.6771	3.291804	0.000764
832.2423	3.29074	0.000727
833.8073	3.289685	0.00069
835.3723	3.288637	0.000655
836.937	3.287597	0.00062
838.5016	3.286565	0.000587
840.0661	3.285541	0.000555
841.6305	3.284525	0.000524
843.1947	3.283516	0.000494
844.7588	3.282515	0.000465
846.3226	3.281522	0.000437
847.8864	3.280536	0.00041
849.4501	3.279557	0.000384
851.0136	3.278586	0.000359
852.577	3.277622	0.000335
854.1401	3.276666	0.000313
855.7032	3.275716	0.000291
857.2661	3.274774	0.00027
858.8289	3.273839	0.00025
860.3915	3.272911	0.000232
861.954	3.27199	0.000214
863.5163	3.271076	0.000198
865.0785	3.270169	0.000182
866.6405	3.269269	0.000167
868.2025	3.268375	0.000153
869.7642	3.267489	0.00014
871.3258	3.266609	0.000128
872.8872	3.265736	0.000116
874.4485	3.26487	0.000105
876.0096	3.26401	0.000095
877.5706	3.263157	0.000086
879.1315	3.26231	0.000077
880.6922	3.26147	0.000069
882.2526	3.260636	0.000062
883.8131	3.259808	0.000055
885.3732	3.258987	0.000049
886.9334	3.258172	0.000043
888.4933	3.257363	0.000038
890.053	3.25656	0.000033
891.6126	3.255763	0.000028
893.1721	3.254972	0.000024
894.7313	3.254187	0.000021
896.2905	3.253408	0.000018
897.8495	3.252635	0.000015
899.4083	3.251867	0.000012
900.967	3.251105	0.00001
902.5255	3.250349	0.000008
904.0838	3.249598	0.000007
905.642	3.248853	0.000005
907.2	3.248113	0.000004
908.7579	3.247379	0.000003
910.3156	3.24665	0.000002
911.8732	3.245926	0.000002
913.4305	3.245208	0.000001
914.9878	3.244495	0.000001
916.5448	3.243787	0
918.1017	3.243083	0
919.6584	3.242385	0
921.215	3.241692	0
922.7714	3.241004	0
924.3276	3.240321	0
925.8837	3.239642	0
927.4396	3.238968	0
928.9954	3.238299	0
930.551	3.237634	0
932.1063	3.236974	0
933.6616	3.236318	0
935.2167	3.235667	0
936.7716	3.23502	0
938.3263	3.234377	0
939.8809	3.233739	0
941.4352	3.233105	0
942.9894	3.232475	0
944.5436	3.231849	0
946.0975	3.231227	0
947.6512	3.23061	0
949.2047	3.229996	0
950.758	3.229387	0
952.3112	3.228781	0
953.8643	3.228179	0
955.4171	3.227582	0
956.9697	3.226987	0
958.5223	3.226397	0
960.0746	3.225811	0
961.6268	3.225228	0
963.1787	3.224648	0
964.7305	3.224073	0
966.2821	3.223501	0
967.8335	3.222933	0
969.3848	3.222368	0
970.9359	3.221807	0
972.4868	3.221249	0
974.0375	3.220695	0
975.5881	3.220144	0
977.1384	3.219596	0
978.6886	3.219052	0

980.2386	3.218511	0
981.7884	3.217974	0
983.3381	3.217439	0
984.8875	3.216908	0
986.4368	3.216381	0
987.9858	3.215856	0
989.5348	3.215334	0
991.0835	3.214816	0
992.632	3.214301	0
994.1804	3.213789	0
995.7286	3.213279	0
997.2766	3.212773	0
998.8243	3.21227	0
1010.709	3.208501	0
1014.082	3.207461	0
1017.454	3.206434	0
1020.828	3.205419	0
1024.201	3.204417	0
1027.576	3.203426	0
1030.951	3.202446	0
1034.326	3.201479	0
1037.702	3.200522	0
1041.079	3.199577	0
1044.456	3.198642	0
1047.834	3.197719	0
1051.212	3.196806	0
1054.591	3.195903	0
1057.97	3.195011	0
1061.35	3.194128	0
1064.731	3.193256	0
1068.112	3.192393	0
1071.494	3.19154	0
1074.876	3.190696	0
1078.259	3.189862	0
1081.642	3.189037	0
1085.026	3.18822	0
1088.411	3.187413	0
1091.796	3.186614	0
1095.181	3.185824	0
1098.568	3.185043	0
1101.954	3.18427	0
1105.342	3.183505	0
1108.729	3.182748	0
1112.118	3.181999	0
1115.507	3.181257	0
1118.896	3.180524	0
1122.287	3.179799	0
1125.677	3.17908	0
1129.069	3.17837	0
1132.46	3.177666	0
1135.853	3.17697	0
1139.246	3.176281	0
1142.639	3.175599	0
1146.033	3.174923	0
1149.428	3.174255	0
1152.823	3.173593	0
1156.219	3.172938	0
1159.615	3.172289	0
1163.012	3.171647	0
1166.409	3.171011	0
1169.807	3.170382	0
1173.206	3.169758	0
1176.605	3.169141	0
1180.005	3.16853	0
1183.405	3.167924	0
1186.805	3.167325	0
1190.207	3.166731	0
1193.609	3.166142	0
1197.011	3.16556	0
1200.414	3.164983	0
1203.818	3.164412	0
1207.222	3.163845	0
1210.627	3.163285	0
1214.032	3.162729	0
1217.438	3.162179	0
1220.844	3.161633	0
1224.251	3.161093	0
1227.659	3.160558	0
1231.067	3.160028	0
1234.476	3.159503	0
1237.885	3.158982	0
1241.295	3.158466	0
1244.705	3.157955	0
1248.116	3.157449	0
1251.527	3.156947	0
1254.939	3.156449	0
1258.352	3.155956	0
1261.765	3.155468	0
1265.179	3.154983	0
1268.593	3.154503	0
1272.008	3.154028	0
1275.423	3.153556	0
1278.839	3.153089	0
1282.256	3.152626	0
1285.673	3.152166	0
1289.091	3.151711	0
1292.509	3.15126	0
1295.927	3.150812	0
1299.347	3.150369	0
1302.767	3.149929	0
1306.187	3.149493	0
1309.608	3.149061	0
1313.03	3.148632	0
1316.452	3.148207	0
1319.875	3.147786	0
1323.298	3.147368	0
1326.722	3.146954	0
1330.146	3.146543	0
1333.571	3.146136	0
1336.997	3.145732	0
1340.423	3.145331	0
1343.849	3.144934	0
1347.276	3.14454	0
1350.704	3.144149	0
1354.133	3.143761	0
1357.561	3.143377	0
1360.991	3.142995	0
1364.421	3.142617	0
1367.851	3.142242	0
1371.283	3.14187	0
1374.714	3.1415	0
1378.147	3.141135	0
1381.579	3.140771	0
1385.013	3.140411	0
1388.447	3.140053	0
1391.881	3.139699	0
1395.316	3.139347	0
1398.752	3.138998	0
1402.188	3.138651	0
1405.625	3.138308	0
1409.062	3.137967	0
1412.5	3.137629	0
1415.939	3.137293	0
1419.378	3.13696	0
1422.817	3.13663	0
1426.257	3.136302	0
1429.698	3.135976	0
1433.139	3.135653	0
1436.581	3.135333	0
1440.023	3.135015	0
1443.466	3.134699	0
1446.91	3.134386	0
1450.354	3.134075	0
1453.799	3.133767	0
1457.244	3.133461	0
1460.69	3.133157	0
1464.136	3.132855	0
1467.583	3.132556	0
1471.03	3.132259	0
1474.478	3.131964	0
1477.927	3.131672	0
1481.376	3.131381	0
1484.825	3.131093	0
1488.276	3.130806	0
1491.727	3.130522	0
1495.178	3.13024	0
1498.63	3.12996	0
1502.082	3.129682	0
1505.535	3.129406	0
1508.989	3.129132	0
1512.443	3.12886	0
1515.898	3.12859	0
1519.353	3.128322	0
1522.809	3.128056	0
1526.266	3.127791	0
1529.723	3.127529	0
1533.18	3.127269	0
1536.638	3.12701	0
1540.097	3.126753	0
1543.556	3.126498	0
1547.016	3.126245	0
1550.476	3.125993	0
1553.937	3.125743	0
1557.399	3.125495	0
1560.861	3.125249	0
1564.324	3.125005	0
1567.787	3.124762	0

1571.25	3.124521	0
1574.715	3.124281	0
1578.18	3.124043	0
1581.645	3.123807	0
1585.111	3.123573	0
1588.578	3.123339	0
1592.045	3.123108	0
1595.512	3.122878	0
1598.981	3.12265	0
1602.449	3.122423	0
1605.919	3.122198	0
1609.389	3.121974	0
1612.859	3.121752	0
1616.33	3.121531	0
1619.802	3.121312	0

1623.274	3.121094	0
1626.747	3.120878	0
1630.22	3.120663	0
1633.694	3.12045	0
1637.169	3.120238	0
1640.644	3.120027	0
1644.119	3.119818	0
1647.595	3.11961	0
1651.072	3.119404	0
1654.549	3.119198	0
1658.027	3.118994	0
1661.505	3.118792	0
1664.984	3.118591	0
1668.464	3.118391	0
1671.944	3.118192	0

1675.424	3.117995	0
1678.906	3.117799	0
1682.387	3.117604	0
1685.87	3.117411	0
1689.353	3.117218	0